2011

Evolution of structural and physical properties of transition metal oxide $Sr_3(Ru_1-xMnx)_2O_7$ ($0 \leq x \geq 0.7$) with Mn concentration

Biao Hu
Louisiana State University and Agricultural and Mechanical College

EVOLUTION OF STRUCTURAL AND PHYSICAL PROPERTIES OF TRANSITION METAL OXIDE $SR_3(RU_{1-x}MN_x)_2O_7$ ($0 \leq X \leq 0.7$) WITH MN CONCENTRATION

A Dissertation
Submitted to the Graduate Faculty of the
Louisiana State University and
Agricultural and Mechanical College
in partial fulfillment of the
requirement for the degree of
Doctor of Philosophy
In
The Department of Physics and Astronomy

by
Biao Hu
B.S., Lanzhou University, 2002
M.S., Fudan University, 2005
August, 2011

Dedication

To my parents

Acknowledgements

First I am grateful to my advisors, Professor Ward Plummer and Professor Rongying Jin, for providing me with the opportunity to carry out fundamental research in strongly correlated electronic system field in Louisiana State University. I greatly benefit from their detailed guidance and scientific insight throughout my PhD study. I sincerely appreciate their instructions and help in assisting me to finish my dissertation.

I acknowledge Professor Jiandi Zhang for the vivid explanations of physics puzzles and help in writing dissertation. I would also like to acknowledge my committee: Professor Ilya Vekhter and Professor Hui-Hsiung Kuo for their reviews of dissertation.

I would like to thank Dr. Von Braun Nascimento for the help in LEED theoretical calculation and experiment. I greatly acknowledge Gregory T. McCandless for the single-crystal XRD experiments and crystallographic structure refinements. I also thank Professor Julia Y. Chan for the useful discussion in data interpretation and Professor Shane Stadler for the powder XRD experiments.

I send my thanks to collaborators in Oak Ridge National Laboratory: Wei Tian, Feng Ye, Songxue Chi, Jerel L Zarestky, V. O. Garlea, Jaime A. Fernamdez-Baca for neutron scattering experiment and An-Ping Li, Minghu Pan for STM/S experiment.

I feel grateful to all my colleagues in LSU: Yiming Xiong, Amar B. Karki, Jianneng Li, Zhenyu Diao, Donovan Myers, Xiaobo He, Guorong Li, Chen Chen, Fangyang Liu, Junsoo Shin, Jing Teng, Zhaoliang Liao, Dalgis Mesa, Yi Li and Lina Chen.

My final and most heartfelt acknowledgement must go to my parents. I greatly thank them for the endless love and supporting and caring for me all of my life.

Table of Contents

List of Tables

List of Figures

Abstract

Correlated Electron Materials (CEMs) have attracted the attention of the materials community because the strong coupling between charge, lattice, orbital, and spin degrees of freedom produces exotic phenomena. Transition metal oxide series $Sr_{n+1}Ru_nO_{3n+1}$ (n = 1 to ∞) is a prototype of CEMs. The n = 2 member of this family $Sr_3Ru_2O_7$ is the subject of this dissertation. It has a paramagnetic (PM) metallic ground state, which can be driven into an antiferromagnetic (AFM) insulator with a partial substitution of Ru by Mn. The focus of this research is to understand the role of chemical doping as the driving force for the structural, electrical and magnetic properties in Mn-doped $Sr_3Ru_2O_7$. A key to achieving this goal is contained in the understanding of different magnetic ordering in the system. High quality single crystals $Sr_3(Ru_{1-x}Mn_x)_2O_7$ ($0 \leq x \leq 0.7$) have been grown by the floating zone technique in an image furnace. A phase diagram of $Sr_3(Ru_{1-x}Mn_x)_2O_7$ is presented, which is divided into five different regions. The structural, electrical and magnetic properties of $Sr_3(Ru_{1-x}Mn_x)_2O_7$ reveal a turning point around x = 0.2, but the phase diagram keeps changing with increasing x. Two characteristic temperatures T_{MIT} and T_M are determined from electrical and magnetic properties measurements, where T_{MIT} represents the temperature of a metallic-to-insulating crossover while T_M corresponds to a peak in magnetic susceptibility. T_{MIT} monotonically increases with increasing x while T_M shows a cusp at x = 0.16 ($T_{MIT} > T_M$) and the difference between T_{MIT} and T_M becomes much larger above x = 0.2. Elastic neutron scattering experiment on x = 0.16 crystal confirms a long-range AFM ordering below its T_M and suggests short-range magnetic correlations between T_{MIT} and T_M.

Chapter 1 Introduction

1.1 Background

Contemporary studies in condensed matter physics face many challenges in understanding complexity in many-body systems. In an early article entitled "More Is Different - Broken Symmetry and the Nature of the Hierarchical Structure of Science", Anderson wrote that "*The behavior of large and complex aggregates of elementary particles is not to be understood in terms of a simple extrapolation of the properties of a few particles*" [1]. In complex systems, where particles strongly interact, exotic phenomena emerge, which is beyond our understanding of the properties of the individual constituents. The so-called strongly correlated materials, where the potential energy is comparable to the kinetic energy, display unusual functionality like high temperature superconductivity (HTSC) in cuprates or colossal magnetoresistence (CMR) in manganites, which cannot be described effectively in a non-interacting picture. Both HTSC cuprates and manganites are transition metal oxides (TMOs) and share a common perovskite structure. Figure 1.1 (a) shows an ideal cubic perovskite with an empirical formula ABO_3, where the A cations (A = alkaline earth or lanthanide cation) are located on the corners, the B cation (B = transition metal cation) is located in the body center, and the oxygen occupies the faces. In fact, most perovskite TMOs deviate from the perfect cubic structure and show distortions, rendering rhombohedral, tetragonal or orthorhombic structues. The tolerance factor, *t*, of an ABO_3 perovskite is defined by $t = \frac{(r_A + r_O)}{\sqrt{2}(r_B + r_O)}$, where the r_A, r_B, r_O are the ionic radii of the A-site, B-Site cations and oxygen anions, respectively. If *t* is 1, the structure will be cubic. Transition metal B cation and its surrounding O ions form a closed packing either tetrahedron or octahedron. The crystal field created by the octahedral coordination lifts the degeneracy to create the e_g and t_{2g} subshells for *d* electrons (Figure 1.1 (b) and (c)) [2]. Overlap

between the wavefunctions of the transition metal *d* electrons and the oxygen 2*p* electrons is called *p-d* hybridization. Goodenough, in 1955, explained that the electronic band-structure at the Fermi energy of ABO_3 perovskite can often be attributed to hybridization between *d* orbital in transition metal and *p* orbital in the O ion [3]. The electronic states from the A-site cations are far from the Fermi energy and are often neglected when considering low-energy electronic properties. The substitution of isovalent cations onto the A-site does not add or remove any electronics but may modify the crystal structure, hence, affect the *p-d* hybridization. Non-isovalent substitution on the A-site can add or remove electrons from the band at E_F. Electrons can be introduced into the band at the Fermi level if a divalent cation is replaced by a trivalent cation. Holes are introduced if the substitution is *vice versa*.

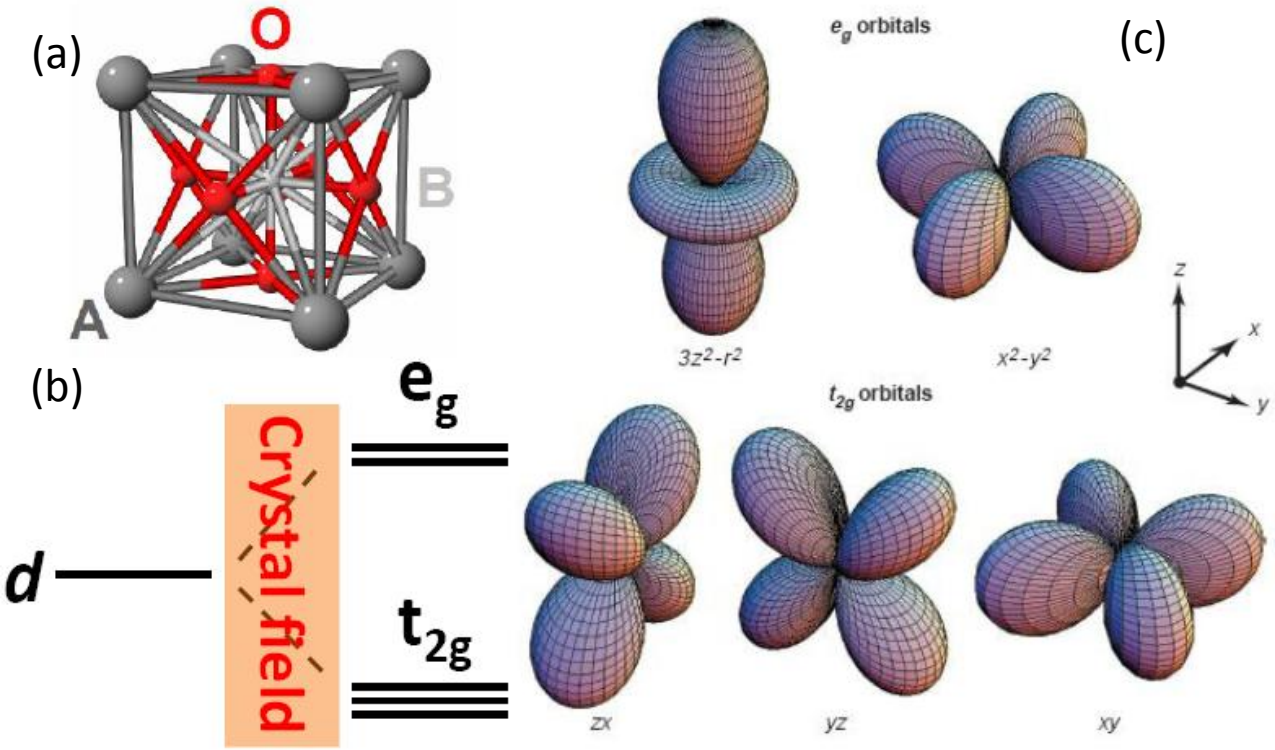

Figure 1.1 (a) Perovskite structure. A-site shown as dark grey on corners of cubic structure. B-site shown as light grey inhibiting center of octahedral. Oxygen shown as red. (b) Crystal field splitting lifts band degeneracy into subshells e_g and t_{2g}. (c) Five *d* orbitals. In the cubic crystal field, this fivefold degeneracy is lifted to two e_g orbitals [$(x^2 - y^2)$ and $(3z^2 - r^2)$] and three t_{2g} orbitals [(*xy*), (*yz*), (*zx*)]. Figure adapted from [2, 3]

The manganite $R_{1-x}A_xMnO_3$ is a class of provskite with an ABO_3 structure, where R is a rare earth – La, Nd, or Pr and A is a divalent alkali – Ca, Sr, or Ba [4, 5]. Slightly changing in x will result in drastic changes in the overall character of the compound. The central manganese ion has three (Mn^{4+}) or four (Mn^{3+}) electrons. According to Hund's rule, three of four electrons in Mn^{3+} ion fill only one electron in each level, the rest of one electron will occupy one of degenerated e_g orbital, for example, d_{3z2-r2}. If the d_{3z2-r2} orbital is defined along the z-axis, the d_{x2-y2} orbital lies in the xy plane. As shown in Figure 1.2, the reduced coulomb repulsion between oxygen ions is achieved by the elongation of the Mn-O bond in z-axis. This is accompanied with an enhanced coulomb repulsion caused by the compression of the MnO_6 in the xy plane. Such a lattice distortion caused by the modified coulomb interaction of the electrons within the crystal is called Jahn-Teller (JT) distortion [6].

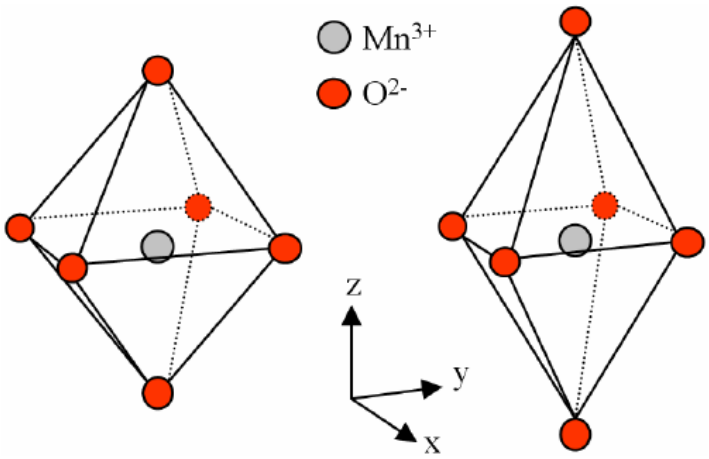

Figure 1.2 Jahn-Teller distortion in an octahedron MnO_6. The undistorted octahedron is shown on the left. The image on the right shows the elongated octahedron along the z-axis. Figure adapted from [3]

In 1951, Zener proposed the so-called double-exchange (DE) interaction between Mn^{3+} and Mn^{4+} ions to explain the ferromagnetic ground state of metallic $R_{1-x}A_xMnO_3$ [7, 8]. A fraction x of Mn is in the tetravalent Mn^{4+} with S = 3/2 state and 1-x in the trivalent Mn^{3+} with S = 2 state, as

shown in Figure 1.3 (a). This process arises via the transfer of an electron from Mn^{3+} to the central O^{2-} simultaneous with transfer from O^{2-} to Mn^{4+}. Anderson and Hasegawa broadened this model and treated the core spin of each Mn ion classically but the mobile electron quantum mechanically [9]. Based on this assumption, there is a transfer probability $t = t_0\cos(\theta/2)$ where $t = 1$ at $\theta = 0$ and $t = 0$ at $\theta = 180°$ (Figure 1.3 (b)). Thus, the exchange energy is lower when the itinerant electron's spin is parallel to the total spin of the Mn cores. Based on this model, many further modifications are developed in the past 50 years [10]. However, DE model is only able to give a qualitative explanation of transport properties, and unable to explain observed Curie temperatures and multiple electronic and magnetic phases.

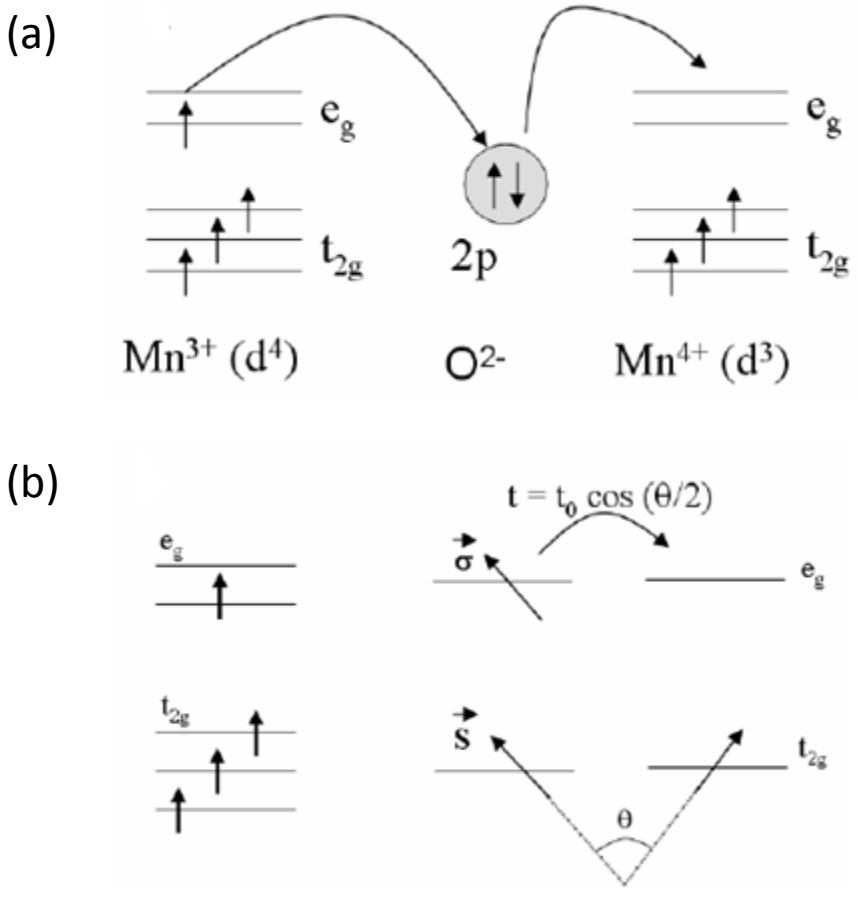

Figure 1.3 Zener's double exchange model and de Gennes spin-canted states. Figure adapted from [7 - 8].

The emergence of CMR effect in manganites and HTSC in cuprates revived the research in perovskite or perovskite-related structures [10 – 22]. In thin films of $La_{0.67}Ca_{0.33}MnO_x$, a MR effect three orders of magnitude larger than the typical giant MR of superlattice films was observed [11]. Following studies on $La_{1-x}Sr_xMnO_3$, $La_{1-x}Ca_xMnO_3$ and $Pr_{1-x}Ca_xMnO_3$ single crystals reveal rich phase diagrams and existences of competing phases in manganites [12]. Figure 1.4 (a) shows coupled metal-to-insulator and paramagnetic-to-ferromagnetic transitions at T_c in $La_{0.65}Ca_{0.35}MnO_3$ [16 - 19]. These coupled electronic and magnetic phase transitions are also associated with the static and dynamic lattice distortions [20 - 22]. These exotic properties of TMOs are believed to result from a variety of possible ground states very close together in energy, so the balance between competing phases is very subtle and small changes can create new phenomena. The concept of electronic and magnetic phase separation has been central to understand CMR effects [15]. Figure 1.4 (b) is an illustration of phase separation, where the manganites contain ferromagnetic (FM) clusters with randomly oriented moments separated by regions where a competing antiferromagnetic (AF) insulating phase is stabilized [15]. The fragility of the state shown in Figure 1.4 (b) can be dramatically changed by perturbations such as magnetic fields, pressure and electric fields [23]. Many experimental works have directly observed phase separation using a variety of techniques [24, 25]. Using both scanning electron microscope (SEM) and scanning tunneling microscopy/spectroscopy (STM/STS), a dynamic phase separation evolution with applied stress was reported in a correlated system $Sr_3(Ru_{0.8}Mn_{0.2})_2O_7$, which undergoes a Mott-type metal-insulator transition (MIT) [26]. Figure 1.5 (a) and (b) show the domain patterns before and after applying stress, respectively. The insulating domain appears brighter than the metallic one. As shown in Figure 1.5 (b) and (c), in the presence of stress, the insulating phase expands dramatically at the expense of the metal one at a constant temperature. The insulating domains expand slowly over a

period of several hours for the crystal with nominal strain of 0.0033% (Figure 1.5 (c)). The domain area increases logarithmically with time without any sign of saturation in a 10 *H* duration (Figure 1.5 (d)). The speed of evolution clearly increases with increasing the amplitude of strain. Thus, the dramatic responses of phase separation to strain in $Sr_3(Ru_{0.8}Mn_{0.2})_2O_7$ reveal the coexistence of competing phases in the vicinity of a Mott MIT [26].

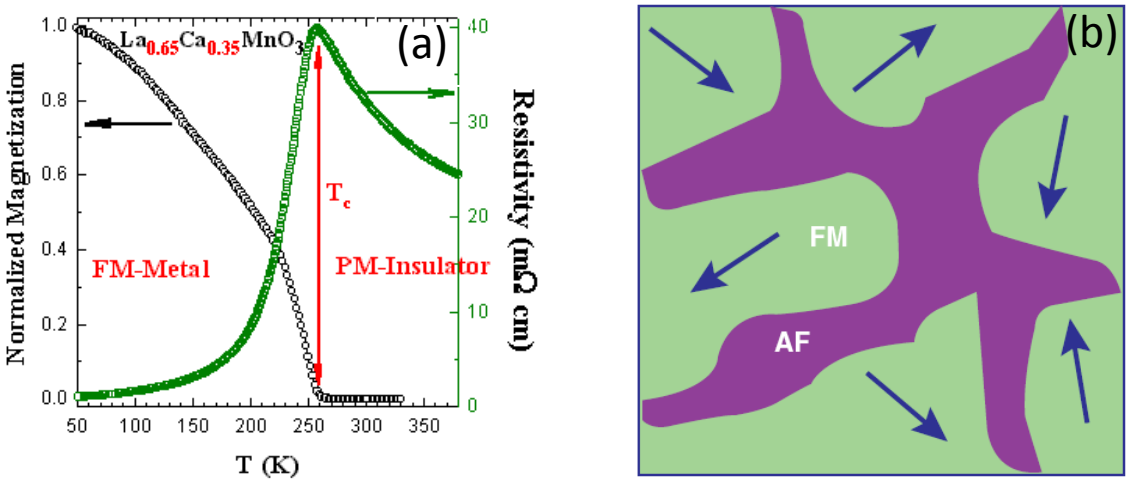

Figure 1.4 (a) Coupled metal-to-insulator (right axis) and paramagnetic-to-ferromagnetic (left axis) transitions at T_c in $La_{0.65}Ca_{0.35}MnO_3$. (b) Scheme of coexistence of FM and AF insulating phase in manganites. Figure adapted from [15 - 19]

1.2 Ruddlesden-Popper Ruthenates

Ruddleden-Popper (RP) ruthenates $Sr_{n+1}Ru_nO_{3n+1}$ (n = 1, 2, 3, ∞) is a prototype of strongly correlated electron materials. RP series originally refer to compounds with K_2NiF_4-type or $Sr_3Ti_2O_7$-type structures, which are the layered perovskite structures and were first reported in the 1950s [27, 28]. Crystal structures of RP ruthenates series is shown in Figure 1.6. The main difference of RP series is the number of octahedron RuO_6 interlinked by sharing apical oxygens prior to separation by Sr-O planes. Sr_2RuO_4 has the same K_2NiF_4 structure as high T_c cuprate parent compound La_2CuO_4 with alternating layers of Sr-O and Ru-O planes. La_2CuO_4 is an antiferromagnetic Mott insulator and the superconductivity is achieved by doping Ba or Sr [13, 14]. On the contrary, the

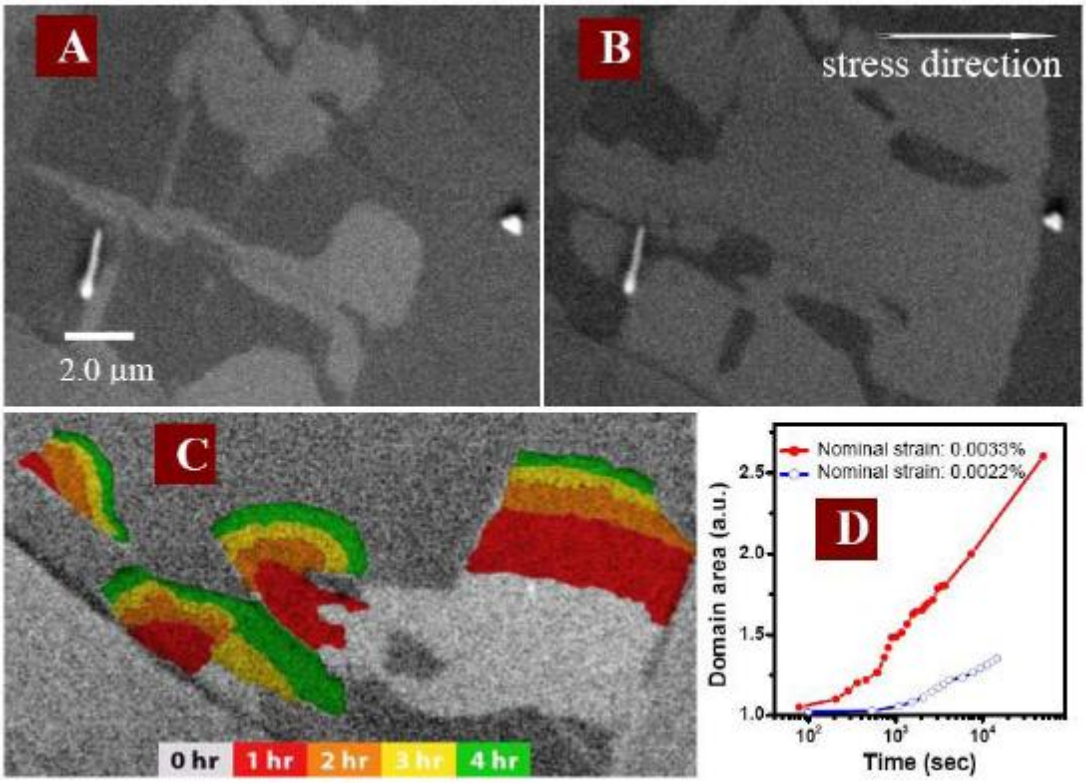

Figure 1.5 Strain-induced domain evolutions in the cleaved surface of $Sr_3(Ru_{0.8}Mn_{0.2})_2O_7$ at 81 K. Domain image before stress (a) and after applying an uniaxial compressive stress in the *ab* plane (along the *a* axis) for 14 h with nominal strain of 0.0033% (b). Domain evolution in time with nominal strain of 0.0022% (c). Domain area change with time (d). SEM primary beam: 5 kV, 50 pA. Figures adapted from [26]

superconductivity in Sr_2RuO_4 is extremely sensitive to disorder, where an impurity with a level of tens of parts per million (ppm) will quickly suppress the superconducting phase [29]. The transport properties of Sr_2RuO_4 show a T^2 dependence of resistivity in both the *ab*-plane and along the *c*-axis at the low temperatures, characteristics of the Fermi liquid behavior [30, 31]. Both angle resolved photoemission spectroscopy (ARPES) and de Haas-van Alphen (dHvA) measurements were carried out on Sr_2RuO_4 and showed a well defined Fermi surface necessary for a Fermi liquid metal, which agrees with local density approximation (LDA) calculations [32 - 34]. As shown in Figure 1.7, the t_{2g} orbitals in ruthenium ion form three Fermi sheets: the d_{xy} bands form a two-dimensional electron-like sheet centered at Γ (*γ*-sheet) and the d_{yz}, d_{zx} bands form a quasi one-dimensional electron-like

sheet centered at Γ (β-sheet) and a quasi one-dimensional hole-like sheet at X (α-sheet). A large anisotropy in the resistivity (ρ_c/ρ_{ab} > 400) was measured at the low temperatures in Sr_2RuO_4, suggesting quasi two-dimensional (2D) character [35]. Spin-triplet pairing has been confirmed by Nuclear Magnetic Resonance (NMR) Knight-shift and Muon Spin Relaxation (μ-SR) measurements [36, 37].

$Sr_3Ru_2O_7$, the closest member to Sr_2RuO_4, is a quasi 2D paramagnetic metal and exhibits Fermi liquid behavior [38]. It has a tetragonal structure with space group *I*4/*mmm* according to the first report in 1990 [39]. Powder neutron diffraction Huang *et al.* reported that the crystal structure of $Sr_3Ru_2O_7$ at room temperature is formed by stacking two blocks of distorted $SrRuO_3$ perovskite along the *c* axis, interleaved with SrO layers, belonging to the symmetry of space group *Pban* [40]. No structural phase transition was observed down to 9 K. But there is an octahedral rotation between the neighboring corner-sharing octahedra in each double perovskite block. The Ru-O-Ru angle in the RuO_2 planes is about 165° rather than 180° [40]. Studies of structural distortion in polycrystalline $Sr_3Ru_2O_7$ via powder neutron diffraction revealed that at room temperature $Sr_3Ru_2O_7$ has the symmetry of orthorhombic space group *Bbcb* (#68) with an octahedral rotation of 6.8° about the *c* axis in terms of an ordered rotation mode within intra- and interbilayer RuO_6 octahedra, as displayed in Figure 1.8. A $\sqrt{2}a_0 \bullet \sqrt{2}a_0 \bullet c_0$ (a_0 = 3.890 Å, c_0 = 20.719 Å) supercell was identified from the superlattice reflections (SLR) in the diffraction pattern [41]. The volume of this supercell in symmetry *Bbcb* is twice as large as that of the undistorted *I*4/*mmm* unit cell. The symmetry of orthorhombic space group *Bbcb* (#68) in $Sr_3Ru_2O_7$ crystal structure was further confirmed by convergent-beam electron diffraction (CBED) experiment on single crystals [42]. The FM and AFM interactions compete in the ground state of $Sr_3Ru_2O_7$. A characteristic peak appears around 16 K in the temperature dependence of magnetic susceptibility $\chi(T)$ of $Sr_3Ru_2O_7$ single crystals (Figure 1.9

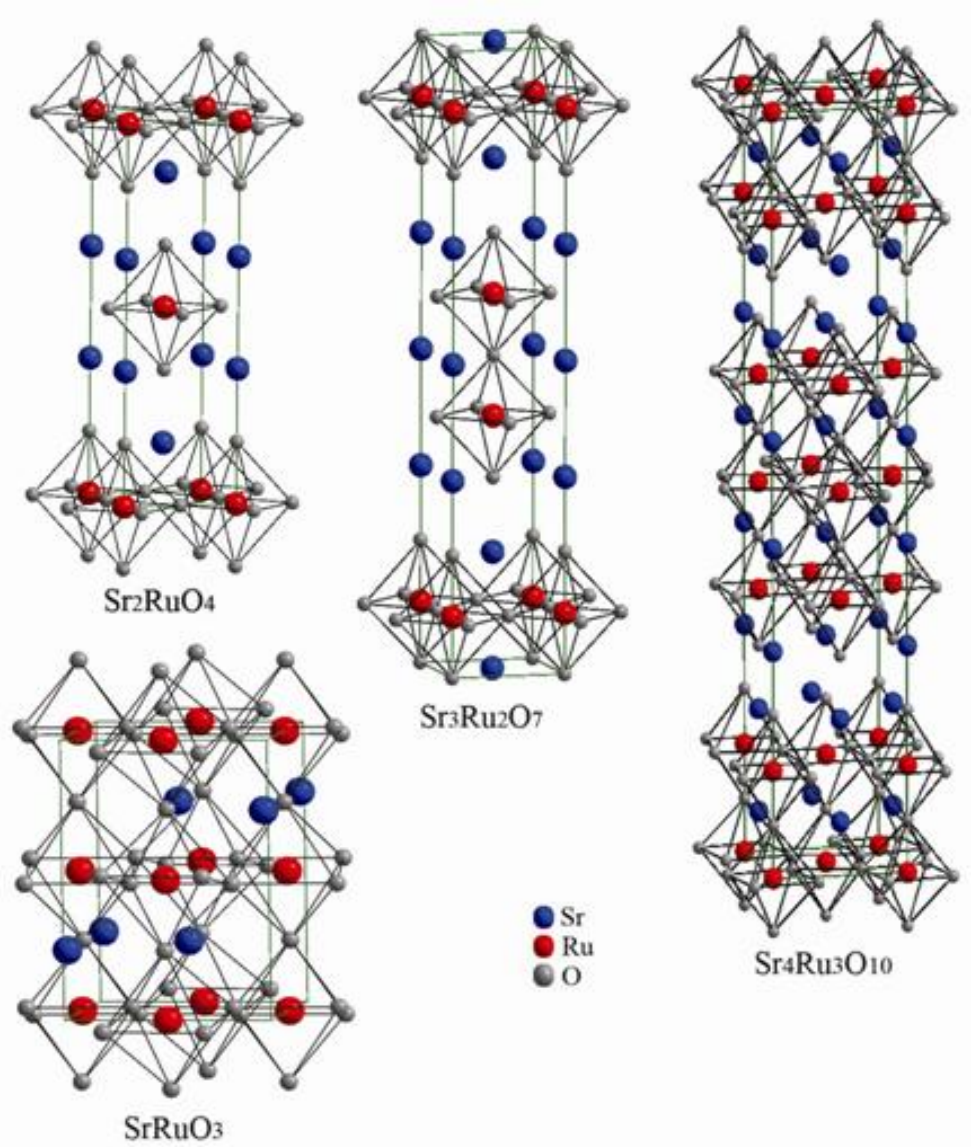

Figure 1.6 Crystal structures of Ruddlesden-Popper (RP) ruthenates series $Sr_{n+1}Ru_nO_{3n+1}$. Both Sr_2RuO_4 (n = 1) and $Sr_3Ru_2O_7$ (n = 2) are denoted under a tetragonal space group *I4/mmm*; $Sr_4Ru_3O_{10}$ (n = 3) and $SrRuO_3$ (n = ∞) belongs to an orthorhombic space group *Pbam* and *Pbnm*, respectively.

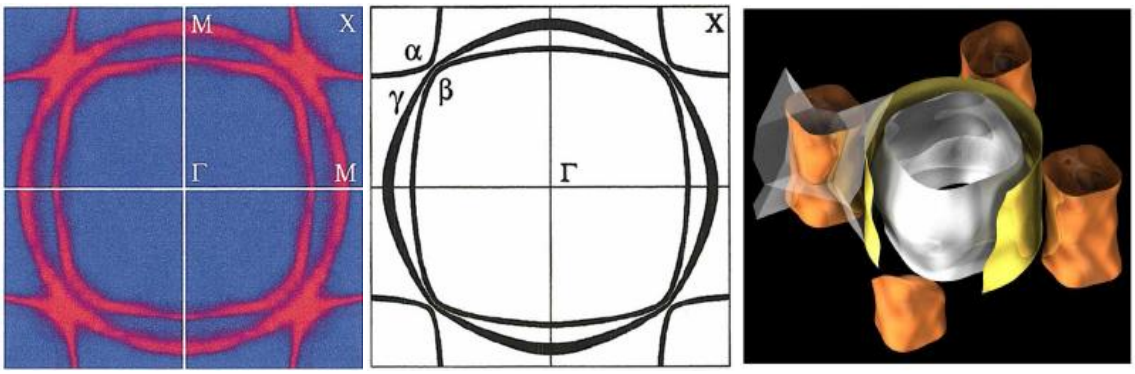

Figure 1.7 Fermi surface of Sr_2RuO_4. Fermi surface as determined from angle resolved photoemission (left) and LDA calculations (middle) and de Haas-van Alphen experiment (right). Figures adapted from [32 - 34]

(a)) [38, 43, 44]. The inelastic neutron scattering (INS) experiment shows that the characteristic peak is due to a short-range AFM-type correlation [45]. Applying hydrostatic pressure up to 1.1 GPa causes an enhancement of FM starting around 70 K, suggesting a FM instability in $Sr_3Ru_2O_7$ (Figure 1.9 (b)). Magnetization of $Sr_3Ru_2O_7$ as a function of applied magnetic field shows a steplike feature at low temperature (Figure 1.9 (c)), indicating the occurrence of metamagnetism [46, 47]. An interpretation for a metamagnetic transition can be explained as the following. An ion with zero net magnetic moment ($J = 0$) in the ground state (such as free Ru^{4+}) but with a $J = 1$ excited state would switch between its zero-magnetization ground state and its fully magnetized excited state at a critical field B_c, where the Zeeman energy lowers one of the $J = 1$ state ($J_z = -1$) below the $J = 0$ state [47]. The metamagnetism in $Sr_3Ru_2O_7$ is due to a rapid change from a paramagnetic state at low fields to a more highly polarized state at high fields [46]. A colorful plot of the power-law behavior ($\rho_{ab}(T) = \rho_{res} + AT^{\alpha}$) of the resistivity of $Sr_3Ru_2O_7$ as a function of temperature and magnetic field (I//ab, B//c) is shown in Figure 1.9 (d) [48]. The Fermi liquid behaviors were observed at low and high fields in the low temperature range and non-Fermi liquid behavior was shown around a critical magnetic field 7.8 T. Figure 1.9 (d) shows a metamagnetic quantum critical point in ultra-pure single crystal $Sr_3Ru_2O_7$ [48]. ARPES measurements on $Sr_3Ru_2O_7$ revealed three Fermi surface pockets

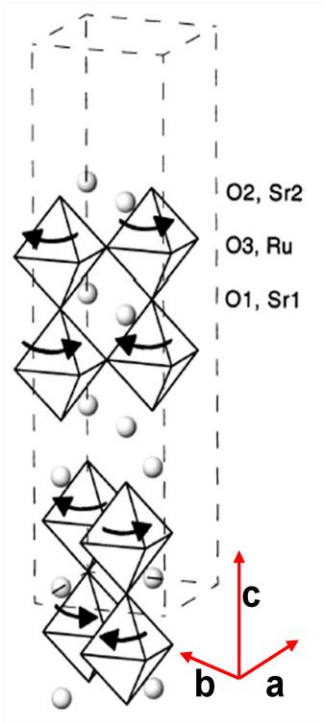

Figure 1.8 The supercell used in the orthorhombic space group *Bbcb* (#68). Ru lies in the center of octahedron and spheres represent Sr atoms. Arrows indicate rotation directions of RuO_6 along *c* axis. The lattice parameter *a* is equal to *b* within the experimental uncertainty. Figure adapted from [41]

centered at Γ, labeled δ, α_1 and α_2 (Figure 1.10 (b)) [49]. LDA calculation shows that the electron like pocket δ derives from Ru d_{x2-y2} orbital, which belongs to e_g manifold and is unoccupied in Sr_2RuO_4 [49, 50]. The holelike pockets α_1 and α_2 derive from the out-of-plane $d_{xz,yz}$ orbitals. Around the *M* points, a small lens (electron like β sheet) and a larger lens with backfolded vertices (electron like γ_1 sheet) are identified. The shape of these pockets indicates mixing of $d_{xz,yz}$ and d_{xy} orbital character on the γ_1 sheet and a dominant $d_{xz,yz}$ character for the β sheet. These ARPES results are consistent with dHvA measurements and LDA calculations [49 - 51]. The $n = 3$ strontium ruthenate, $Sr_4Ru_3O_{10}$, has an orthorhombic unit cell with *Pbam* space group symmetry and is composed of triple layers of corner-shared RuO_6 octahedra separated by double rock-salt layers of Sr-O (Figure 1.6). The RuO_6 octahedra in the outer layers of the two crystallographically independent triple layers per unit cell are rotated in the same sense about the *c* axis about 5.6 °, while the central layers are

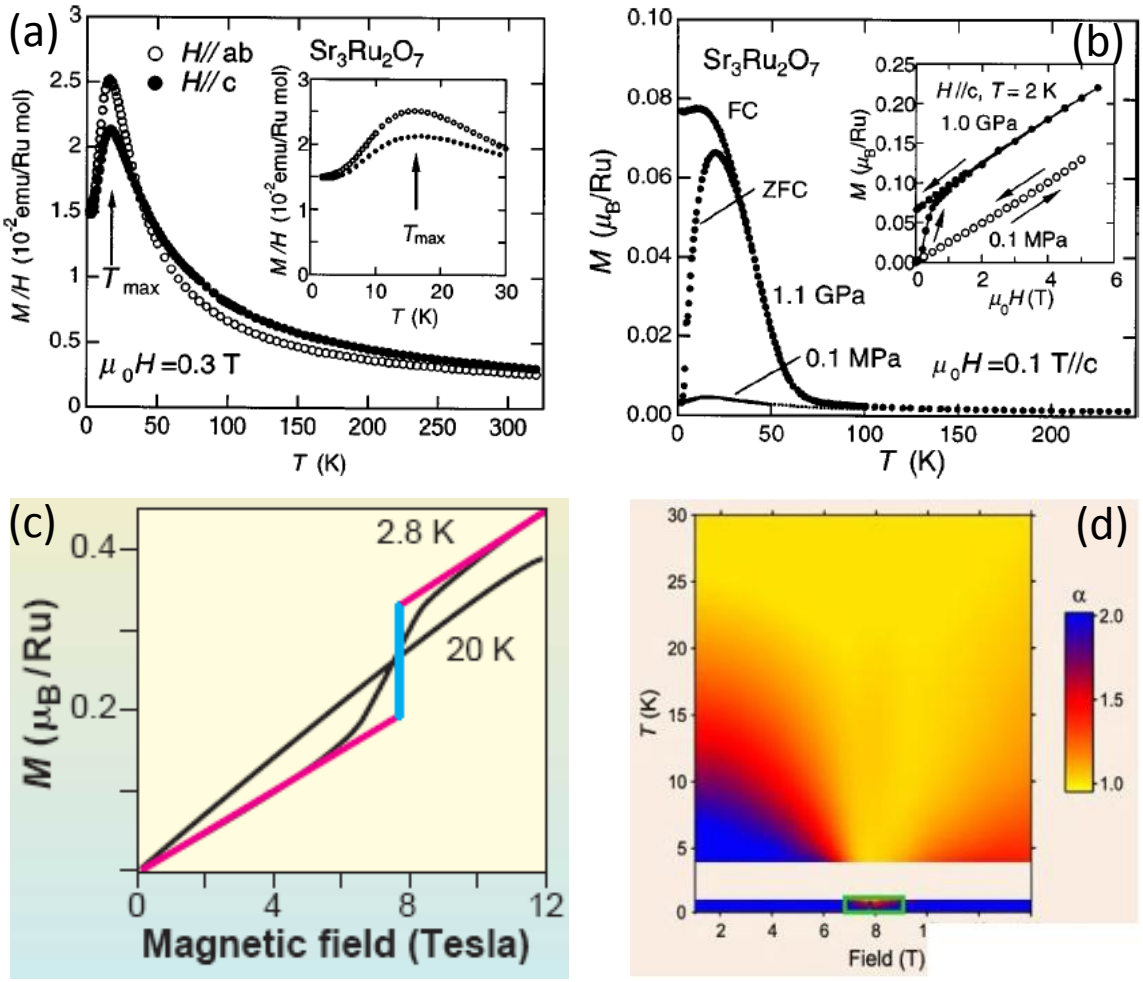

Figure 1.9 (a) The magnetic susceptibility of single crystal $Sr_3Ru_2O_7$ under 0.3 T field above 2 K. (b) The pressure dependence of magnetization $M(T)$ for H//c. Clear ferromagnetic ordering appears under 1.0 GPa at 2 K (Inset of (b)). (c) Magnetization of $Sr_3Ru_2O_7$ as a function of magnetic field at lower temperatures. (d) Colorful plot of the power-law behavior with formula $\rho_{ab}(T) = \rho_{res} + AT^{\alpha}$ for H//c. Figures adapted from [38, 46 - 48]

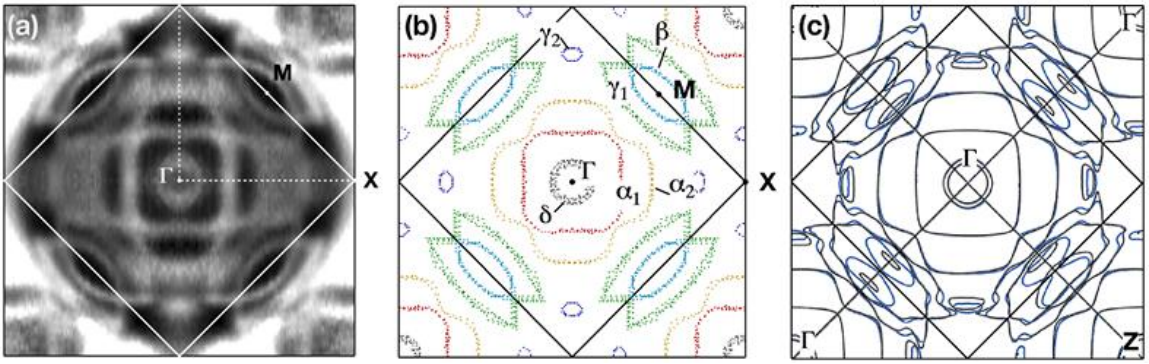

Figure 1.10 Fermi surface of $Sr_3Ru_2O_7$. (a) shows the experimental data taken in the first quadrant of the larger tetragonal BZ and symmetrized with respect to the Ru-Ru nearest neighbor direction. (b) Fermi surface contours extracted from the data shown in (a). (c) LDA calculation for the basal plane (k_z = 0, black) and midplane (k_z = ¼, blue). Figures adapted from [49 - 51]

rotated in the opposite sense about 11.0 ° in each of the triple layers [52]. $Sr_4Ru_3O_{10}$ is a ferromagnet with a Curie temperature T_c = 105 K and a saturated moment of ~ 1.0 μ_B/Ru [53, 54]. The ferromagnetic behavior is followed by an additional magnetic transition at T_M = 50 K primary along the *c* axis with the magnetic state below T_M showing field orientation dependences [55]. A metamagnetic transition occurs in $Sr_4Ru_3O_{10}$ via an electronic phase separation process with magnetic domain formation [56]. The $n = \infty$ end member of the RP series, $SrRuO_3$, is a three dimensional (3D) itinerant ferromagnet (Curie temperature T_c = 160 K, magnetization $M \approx 1.6$ μ_B/Ru) and possesses a distorted perovskite structure with an orthorhombic unit cell in space group *Pbnm* [57, 58].

1.3 Isovalent Doped Ruddlesden-Popper Ruthenates

Chemical doping is a common way to tune the intrinsic properties of TMOs via changing local chemical environment, and band filling, resulting in complicated phase diagrams. The substitution of Sr by Ca induces lattice distortions in $Ca_{2-x}Sr_xRuO_4$ compound because of the smaller ionic radius of Ca^{2+}. These distortions include a rotation of the RuO_6 octahedra about the *c* axis (Figure 1.11 (a)), a tilt around an axis parallel to the edge of the octahedral basal plane (Figure 1.11 (b)) and a flattening of RuO_6 along the *c* axis [59]. Since $Ca_{2-x}Sr_xRuO_4$ system is isovalent

substitution between Ca^{2+} and Sr^{2+}, the structural, electronic and magnetic properties are tuned by lattice distortions. Thus $Ca_{2-x}Sr_xRuO_4$ system provides a good example of strongly correlated system showing bandwidth (W) controlled by lattice distortion without changing charge carrier concentration. Figure 1.12 (a) shows the bulk structural phase diagram of $Ca_{2-x}Sr_xRuO_4$, suggesting no structural distortions in $1.5 < x \leq 2.0$ (*I*4/*mmm*), an octahedral RuO_6 rotation in $0.5 \leq x \leq 1.5$ ($I4_1/acd$), and a combination of RuO_6 rotation and tilt in $0.2 \leq x < 0.5$ ("tilted" phase) and $0 \leq x < 0.2$ (*L-Pbca* and *S-Pbca*) [60]. Correspondingly, their electronic and magnetic properties in $Ca_{2-x}Sr_xRuO_4$ are changed drastically. As shown in Figure 1.12 (b), starting with a superconductor at $x = 2$, the system evolves into a paramagnetic metal ($0.5 \leq x < 2$), a magnetic metal ($0.2 \leq x < 0.5$), and finally an antiferromagnetic insulator ($x < 0.2$). Around region $x \sim 0.5$, a magnetic cluster glass behaviors was clarified below T_{max} [61]. Ca_2RuO_4, the end member of phase diagram, displays a combination of rotation and tilt of RuO_6 in structure and is an antiferromagnetic insulator with a metal-insulator transition at $T_c \sim 360$ K [62]. The underlying physics of the phase diagrams in $Ca_{2-x}Sr_xRuO_4$ system can be understood from the interplay between lattice distortions and magnetism. Figure 1.11 (d) shows the calculated phase diagram. Three types of structure distortions, *I.e.*, RuO_6 rotation, tilting, and the flattening of RuO_6, were considered in the first-principle calculations. The calculated results showed that the RuO_6 rotation will drive the system from a non-magnetic (NM) state to a FM state, while the subsequent tilting plus the flattening of RuO_6 will push the system to an AF region. In theory, the rotation and tilt of RuO_6 are coupled to the FM and the AFM, respectively. The flattening of RuO_6 stabilizes the dominant magnetic interaction in $Ca_{2-x}Sr_xRuO_4$ [63]. The isovalent doping of Sr by Ca in $Sr_3Ru_2O_7$ has been studied recently. A tiny amount of doping will break the competition balance between FM and AFM interactions in the ground state of $Sr_3Ru_2O_7$ and results in rich variety of exotic phenomena. A phase diagram of $Sr_{3-x}Ca_xRu_2O_7$ is displayed in

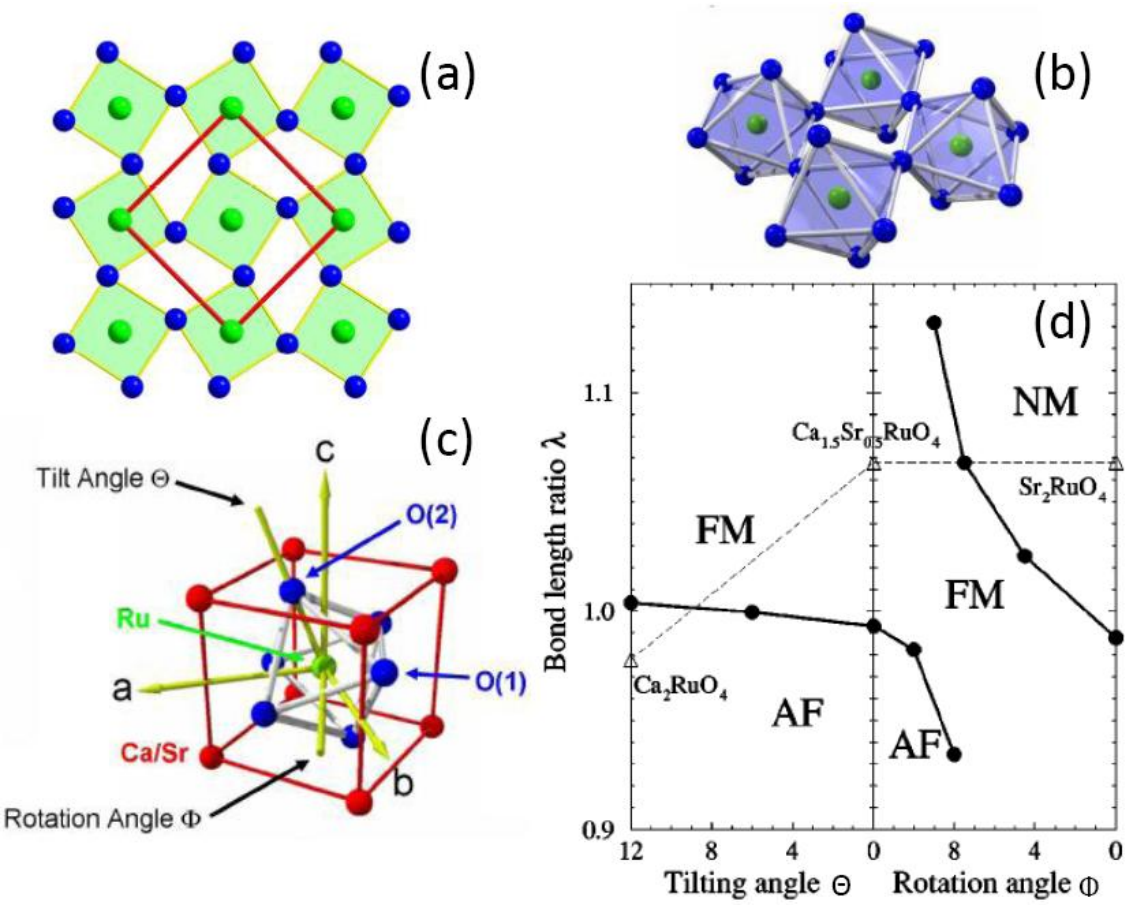

Figure 1.11 (a) Top view of RuO_6 rotation in an enlarged unit cell (red square). (b) Scheme of RuO_6 tilting configuration. (c) Configuration of RuO_6 rotation and tilting in $Ca_{2-x}Sr_xRuO_4$. Θ and Φ denote the rotation angle and tilting angle, respectively. (d) The calculated magnetic phase diagram of Sr_2RuO_4 with structural distortions. Bond length ratio $\lambda = d_c/d_{ab}$ indicates the degree of flattening of RuO_6 octahedron, where d_c (d_{ab}) denotes the Ru-O bond length along the *c* axis (in the *ab* plane) with the volume fixed. The solid bold lines are calculated phase boundaries, while the triangles linked by a dashed line correspond to experimental data. See more details in Ref. 63. Figures adapted from [59, 63]

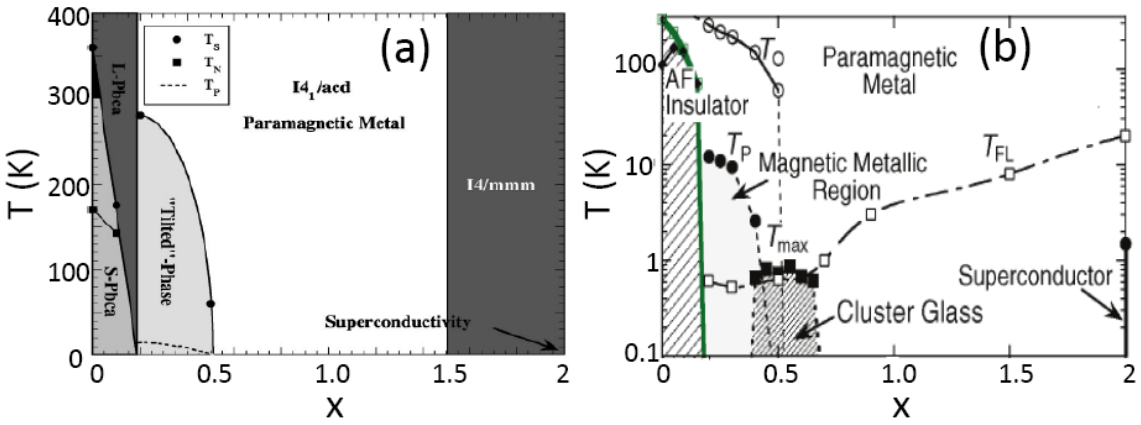

Figure 1.12 (a) Structural phase diagram of $Ca_{2-x}Sr_xRuO_4$ showing *I*4/*mmm* in $1.5 < x \leq 2.0$, $I4_1/acd$ in $0.5 \leq x \leq 1.5$, a "tilted" phase in $0.2 \leq x < 0.5$ and *L-Pbca* and *S-Pbca* in $0 \leq x < 0.2$. T_s: Structure transition temperature; T_N: Neel temperature; T_p: Peak temperature of the susceptibility for the [001] component. (b) Electronic and magnetic phase diagram of $Ca_{2-x}Sr_xRuO_4$. T_{FL}: Fermi liquid behavior temperature; T_{max}: clusters freezing temperature. See more details in Ref. 60 and 61. Figures adapted from [60, 61]

Figure 1.13 [64, 65]. Three regions were divided as the following, region *I*: $0 \leq x \leq 1.2$, region II: $1.2 \leq x \leq 1.8$, region III: $1.8 \leq x \leq 3.0$. The boundary of region *I* and II is $x \approx 1.2$, where the lattice parameters changes abruptly. The boundary of regions II and III is $x \approx 1.8$, where the difference in the lattice parameter between the *a*- and *b*-axis becomes clear [64]. RuO_6 rotation exists at the whole range $0 \leq x \leq 3$ while RuO_6 tilting starts to emerge until $x \approx 1.2$ and changes abruptly at the boundary $x \approx 1.8$ [65]. Correspondingly, the electronic and magnetic properties vary vastly with *x*, as shown in Figure 1.13 (c). No magnetic phase transition is observed in region *I* while a FM cluster glass phase emerges below 4 K in range $0.5 \leq x \leq 1.2$ [65]. Only one anomaly at T_M was observed in region II, where magnetic susceptibility decreases rapidly but remains large for both χ_{ab} and χ_c at $x = 1.25$ and 1.5, which is not characteristic behavior of a simple AFM ordering [64]. The end member of the phase diagram, $Ca_3Ru_2O_7$ ($x = 3$), undergoes an AFM transition at $T_N = 56$ K while remaining metallic, and then a first-order metal-to-nonmetal transition at $T_{MI} = 48$ K, where all lattice constants jump at T_S without a change of the space group symmetry [66, 67]. In $Ca_3Ru_2O_7$, the structural transition temperature T_S is coincident with $T_{MI} = 48$ K. $Ca_3Ru_2O_7$ has a metallic AFM phase

intermediate between T_N and T_{MI} and a quasi 2D metallic ground state of below 30 K [68]. A possible model for the AFM ordering in $Ca_3Ru_2O_7$ is that magnetic moments align ferromagnetically within the double layer and antiferromagnetically between the double layers [68].

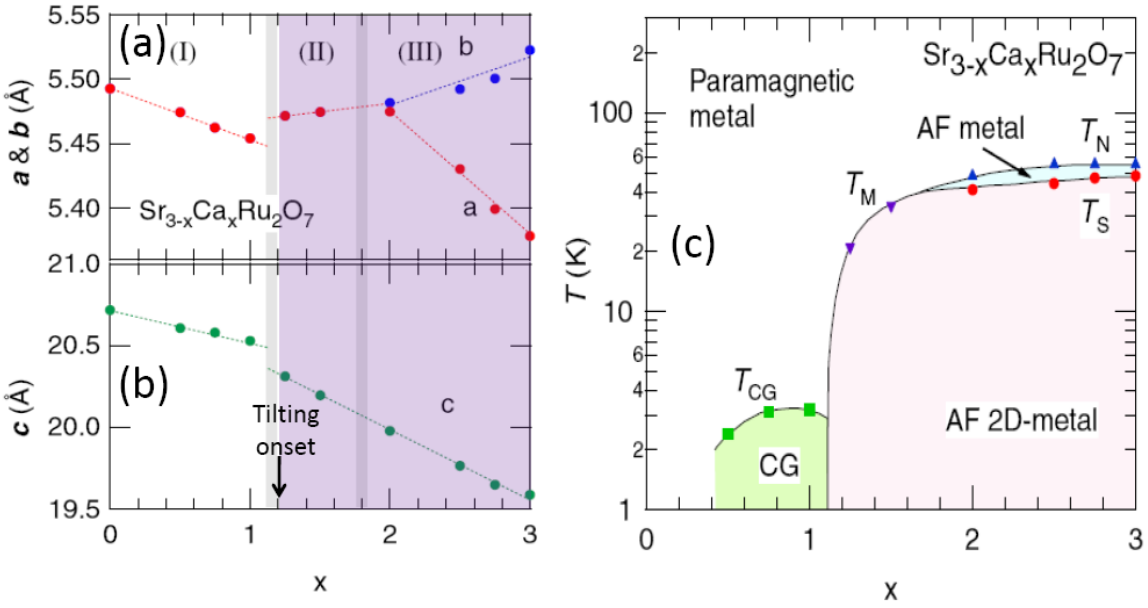

Figure 1.13 (a) and (b) Ca content (x) dependence of the lattice parameters. The substitution content x can be divided into three regions denoted I, II, and III. Arrow in (b) indicates the onset of RuO_6 tilting at x = 1.2. Purple area displays tilting region. (c) The x – T phase diagram for $Sr_{3-x}Ca_xRu_2O_7$. T_{CG} indicates the cluster glass phase. T_N indicates the Neel temperature. T_S denotes the structural transition temperature. T_M indicates the temperature where an anomaly was observed in the measurements in region II. Figures adapted from [64, 65]

1.4 Doped Ruddlesden-Popper Ruthenates: Changing the Transition Metal

The substitution of Ru by Ti in $Sr_3Ru_2O_7$ was studied recently. The Ti^{4+} ion (0.68Å) is easily incorporated in the crystal because of the similar ionic radius as Ru^{4+} (0.67Å) and acts as a nonmagnetic impurity with the electron configuration $3d^0$ in $Sr_3(Ru_{1-x}Ti_x)_2O_7$ [69]. Hooper *et. al* reported that small amount of Ti quickly smears out the metamagnetic quantum phase transition and suppresses the characteristic peak in magnetic susceptibility near 16 K in $Sr_3Ru_2O_7$ and results in a sharp upturn in specific heat [69]. The system remains metallic until approximately 5% doping and shows a Fermi liquid behavior at low temperatures [69]. The elastic and inelastic neutron-scattering

studies on $Sr_3(Ru_{1-x}Ti_x)_2O_7$ shows that samples (x = 0.075 and 0.1) exhibit an incommensurate spin-density wave with a propagation vector of $\boldsymbol{q}_{ic}$ = (0.24, 0.24, 0) [70].

The studies on effects of magnetic impurity in $Sr_3Ru_2O_7$ have been reported [71 - 73]. The pioneering work showed that partial substitution of Ru by magnetic impurity Mn yields a drastic phase change, driving the paramagnetic metal $Sr_3Ru_2O_7$ into an AFM insulator [71]. Resistivity ρ_{ab} is enhanced with Mn concentration x at low temperatures. A sharp increase in resistivity at low temperatures was observed in crystal with x = 0.05, where the metal-insulator transition is shifted to lower temperature with an applied field [71]. A peak at (1/4 1/4 0), reflecting AFM, was observed around the metal-to-insulator transition temperatures in neutron diffractograms in $Sr_3(Ru_{0.95}Mn_{0.05})_2O_7$. Optical conductivity σ(ω) measurement on $Sr_3(Ru_{0.9}Mn_{0.1})_2O_7$ reveals a gap about 0.1 eV, suggesting a metal-to-insulator transition driven by the electron correlation [71]. An electronic phase diagram with a single boundary line separating the paramagnetic metal (PM) state and antiferromagnetic insulator (AFI) state was constructed in $0 \leq x \leq 0.2$, as shown in Figure 1.14.

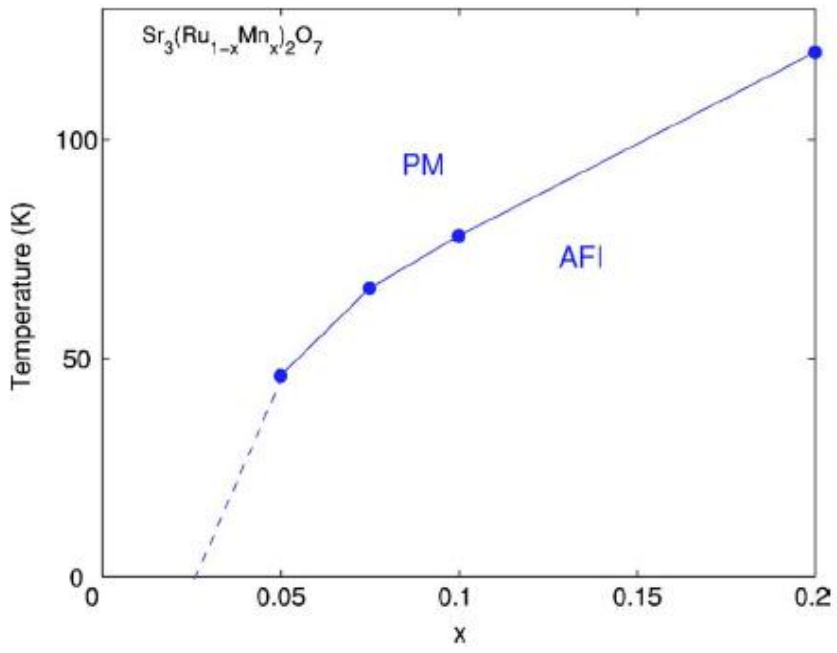

Figure 1.14 Electronic phase diagram of $Sr_3(Ru_{1-x}Mn_x)_2O_7$. Figures adapted from [71]

The valence of Mn in $Sr_3(Ru_{1-x}Mn_x)_2O_7$ has been studied by *x*-ray absorption spectroscopy (XAS). Hossain *et al.* found that Mn impurities show 3+ valence for $x = 0.1$ [72]. From comparisons (Figure 1.15) with well-defined Mn valence compounds, such as MnO (2+), $LaMnO_3$ (3+), and $Sr_3Mn_2O_7$ (4+), the energy position of the $L_{2,3}$ absorption edge in $Sr_3(Ru_{0.9}Mn_{0.1})_2O_7$ is very close to $LaMnO_3$ $L_{2,3}$-edge energy, suggesting Mn impurities in $Sr_3Ru_2O_7$ acting as Mn^{3+} [72]. While Mn^{4+} has three *d* electrons in the 1/2-filled t_{2g} shell, Mn^{3+} has an extra e_g electron ($t_{2g}^3 e_g^1$) and is Jahn-Teller active [72]. The e_g electron would occupy the out-of-plane $d_{3z^2-r^2}$ orbital due to crystal field splitting caused by elongation of RuO_6 octahedron along the *c*-axis. But the *x*-ray linear dichroism (LD) experiment at room temperature shows that the Mn^{3+} e_g electrons occupy the in-plane $d_{x^2-y^2}$ orbital, instead of $d_{3z^2-r^2}$, which is inverse to the standard crystal-field orbital hierarchy in transition metal octahedra. The *ab initio* density functional theory explained that the crystal-field inversion in lightly Mn-doped $Sr_3Ru_2O_7$ is due to the *3d-4d* interplay via the ligand oxygen orbital [72]. However, studies on Mn-doped $Sr_3Ru_2O_7$ via *x*-ray photoelectron spectroscopy (XPS) reveal no change in line shape of Ru $3p_{3/2}$ peaks with Mn doping, suggesting no sign of doping-induced multiple Ru valences [73]. In the end doping compound, $Sr_3Mn_2O_7$ ($x = 1.0$), Mn exhibits 4+ valence. $Sr_3Mn_2O_7$ is an AFM insulator with $T_N = 160$ K and has a tetragonal crystallographic unit cell in space group *I*4/*mmm* [74]. The magnetic structure of $Sr_3Mn_2O_7$ is *G*-type AFM, where each spin is oriented antiparallel to each of its five neighboring spins. The Mn moments ($\mu_{Mn} = 2.31\ \mu_B$) aligns parallel to the *c* axis.

From the paramagnetic metal $Sr_3Ru_2O_7$, which exhibits structural distortion and competitive magnetic correlations, to AFM insulator $Sr_3Mn_2O_7$, $Sr_3(Ru_{1-x}Mn_x)_2O_7$ system provides an opportunity to investigate correlations between structural, electronic and magnetic properties. We are investigating the evolution of structural and physical properties of $Sr_3(Ru_{1-x}Mn_x)_2O_7$ with Mn

concentration. This is the main goal in this dissertation. An achieved phase diagram ($0 \leq x \leq 0.7$) will shed light on the understanding of strongly correlated electronic system.

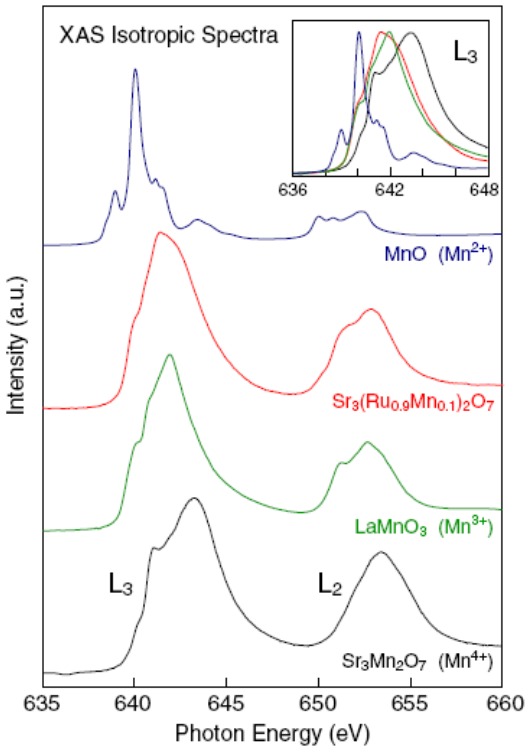

Figure 1.15 Isotropic Mn $L_{2,3}$-edge XAS data from $Sr_3(Ru_{0.9}Mn_{0.1})_2O_7$ and stoichiometric Mn oxides of known valences. Inset: detailed view of the L_3-edge chemical shift. Figure adapted from [72]

Chapter 2 Experimental Techniques and Analytical Procedures

2.1 Synthesis

Single crystals are required in many experiments because grain boundaries and impurities can be minimized. We grow single crystals via floating zone technique (FZT), which has been widely proven to grow high quality single crystals such as high temperature cuprate superconductors [75]. In this technique, no materials container is involved, the crystal growth comes directly from the melt of ceramic rod of the desired material in an optical image furnace [76]. In our optical furnace (Canon Machinery, model: SC1MDH-20020 (Figure 2.1 (a)), there is an ellipsoidal mirrored cavity with halogen lamps installed at foci of elliptic surface reflector. Polycrystalline samples are firstly synthesized via a conventional solid-state reaction method and then pressed into a cylindrical feed rod. As shown in Figure 2.1 (b), a polycrystalline feed rod is suspended using a platinum wire from a platinum hook on the upper shaft. A single crystalline seed rod is mounted coaxially with respect to the feed rod in a ceramic holder on the lower shaft. Both the upper and lower shafts are connected to electric motors allowing vertical transition and rotation around the vertical axis independently. The feed and seed rods are placed within a quartz tube so that a desired atmosphere could be established using different types of gases. The infrared rays emitting from the lamps are converged to the center of cavity. First, the tip of the feed rod is brought into the melting zone. After it starts melting the seed rod moves down continuously from the melt while the feed rod is continuously lowered into the melt to replenish lost material [76]. Thus, a floating molten zone forms between feed and seed rod. The hottest zone is in the center of the cavity with a region of approximately Φ0.5 cm x 0.5 cm. The crystal growth process can be monitored through a CCD camera which is connected to a computer.

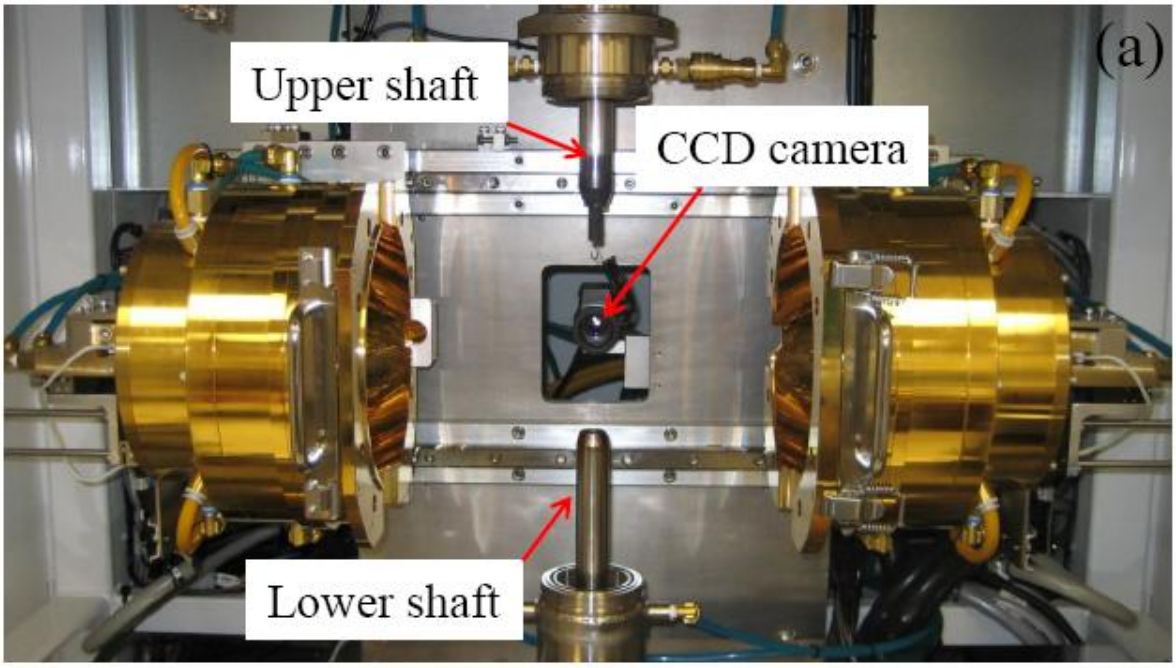

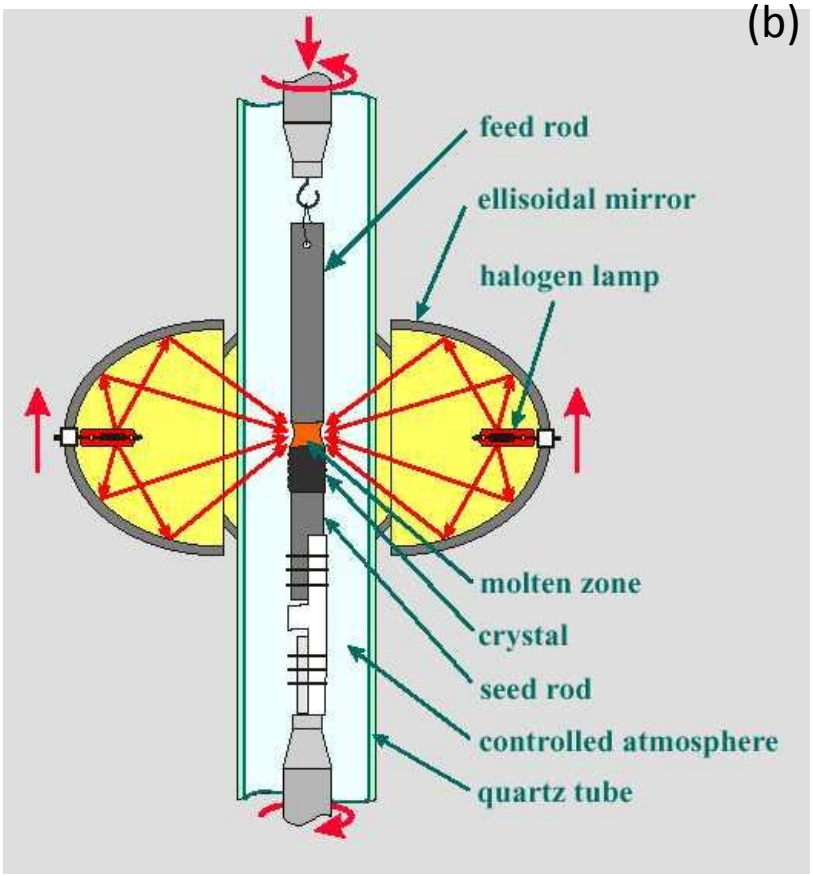

Figure 2.1 (a) Optical image furnace used for single crystal growth. (b) Scheme of single crystal growth by floating zone technique (FZT). Figures adapted from [77]

2.2 Structural Characterization and Analytical Procedures

2.2.1 Powder X-ray Diffraction

Powder X-ray diffraction (XRD) is an effective technique for the identification and the characterization of crystalline solids. In this work, powder XRD measurements were carried out on a Scintag XDS 2000 X-ray diffractometer housed in Department of Physics & Astronomy at Louisiana State University. The diffractometer is installed with a copper K_α X-ray source with a wavelength λ = 1.54 Å. Well ground powder of the samples was placed onto a sample holder of the diffractometer. The data were collected from 2θ = 5 to 85 ° with a constant scan speed at room temperature. Figure 2.2 shows an example of powder XRD diffraction pattern in pulverized single crystal $CaRuO_3$ grown by FZT [78]. All peaks were indexed in the orthorhombic space group *Pnma* and the lattice parameters were a = 5.535(3) Å, b = 7.652(2) Å and c = 5.340(3) Å.

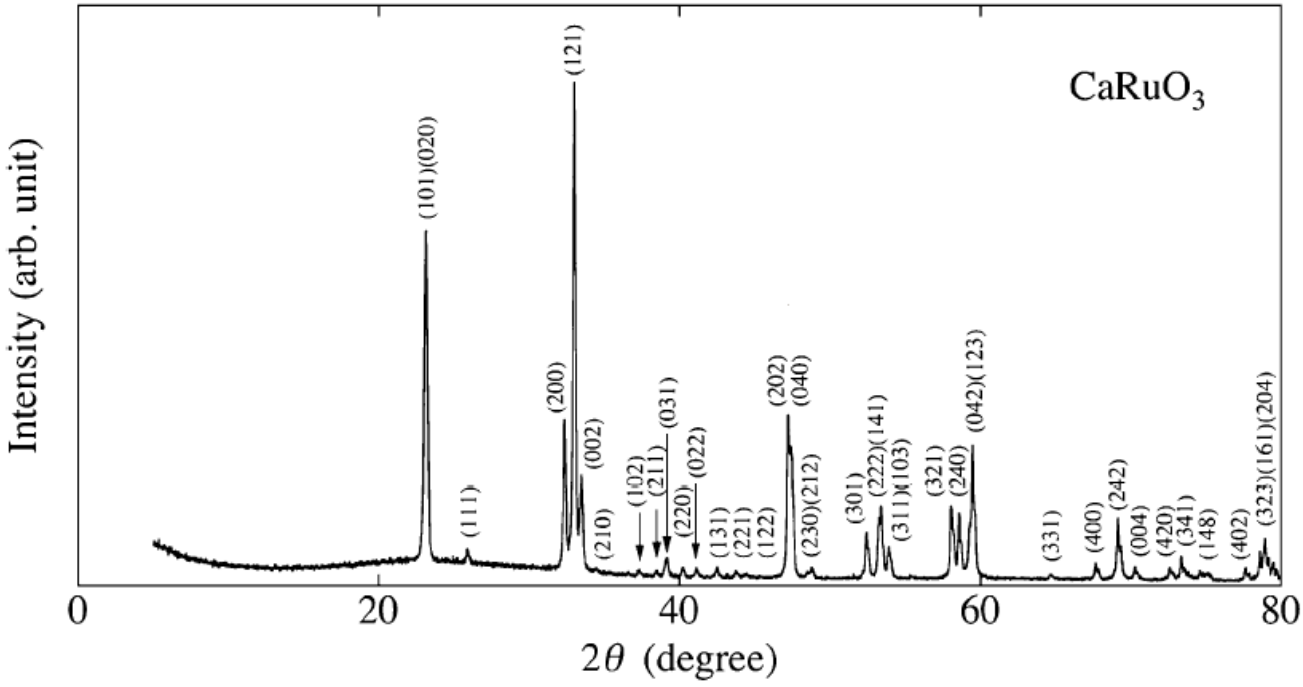

Figure 2.2 The powder X-ray diffraction pattern with indices of $CaRuO_3$ crystal grown by FZT. Figures adapted from [78]

2.2.2 Single-Crystal X-ray Diffraction

Single-crystal XRD provides more detailed structural information such as bond length and bond angle. This method is widely used to determine the crystallographic structure. A tiny piece of a single crystal, with approximate size of 0.03 x 0.08 x 0.08 mm^3, is selected and mounted with epoxy on a thin glass fiber attached to a brass fitting. After allowing sufficient time for the epoxy to dry and harden, vacuum grease is carefully applied at the adhesive intersection of the single crystal and the glass fiber. The combination of the epoxy and the vacuum grease was needed to provide the stability of the sample through the cooling and warming process. In this work, the single-crystal XRD measurement was conducted on a Nonius KappaCCD X-ray diffractometer with a Mo Kα radiation source (λ = 0.71073 Å), a graphite monochromator, and an Oxford Cryosystems 700 series cryostream controller. Most of data collections were made at three different temperatures (298 K, 200 K, and 90 K with a cooling/warming rate of 5 K/minute). The waiting time is about 30 minutes for the temperature of the single crystal to stabilize and about 30 minutes for preliminary unit cell/crystal quality determination, diffraction limit estimation, and set-up of the appropriate scan-set strategy using Nonius SuperGUI software. At each fixed temperature, data collections were approximately 1½ hours long, covering angle theta range of 1.0 ° to 27.5 °. A lower monoclinic symmetry, 2/m, was used in order to increase the number of images collected for refinement. For the thermal-cycling dependence experiment in $Sr_3Ru_2O_7$, each successive thermal cycle was completed in the following order: 1) data collection at 298 K, 2) lowering down temperature to 200 K, 3) data collection at 200 K, 4) lowering down temperature to 90 K, 5) data collection at 90 K, 6) warming up temperature to 200 K, 7) data collection at 200 K, and 8) warming up temperature to 298 K. This order of events was repeated without any delay between cycles. After the data collections were completed, the data refinement was done using the maXus package with SHELXL-97 and SIR97

software [79, 80]. Final refinement is completed using WinGX with SHELXL-97 [81]. Missing symmetry is checked using the "ADDSYM" test in the PLATON program [82].

2.2.3 Low Energy Electron Diffraction

Low Energy Electron Diffraction (LEED) is a sensitive technique to determine the surface structure [83]. Low energy electron beams can be used as an incident wave whose wavelength is shorter than the lattice constant but whose penetration depth in the solid in the range of several angstroms. From the de Broglie relation the wavelength of the electrons is given by:

$$\lambda = h/p \qquad (1)$$

where *H* is the Planck's constant and *p* is the electron momentum. If the electrons are accelerated by a voltage *V*, the kinetic energy of electrons is *eV*, the electron wavelength is determined by:

$$\lambda = h/(2meV)^{1/2} = (150.4/V)^{1/2} \qquad (2)$$

where *e* is the electron charge, and *M* is the mass of electron. In Eq. (2), the unit of *V* is volt, and λ is $\mathring{A}$.

The impinging low energy electrons strongly interact with the atoms at the top surface layers. This strong interaction gives rise to a multiple scattering process that reduces the free mean path of the probing electrons and enhances the surface sensitivity of the technique. Another consequence of this multiple scattering is that the surface structure determination by LEED needs to follow an indirect methodology, in which the experimentally collected *I-V* curves are compared with theoretically calculated ones for a variety of structure. From the LEED experiment we can directly acquire *I-V* curves, which are the intensity of a certain diffraction beam as a function of the incident electron beam energy. Retarding Field Analyzer (RFA), as shown in Figure 2.3 (a), is the main part of the LEED instrument. Figure 2.3 (b)

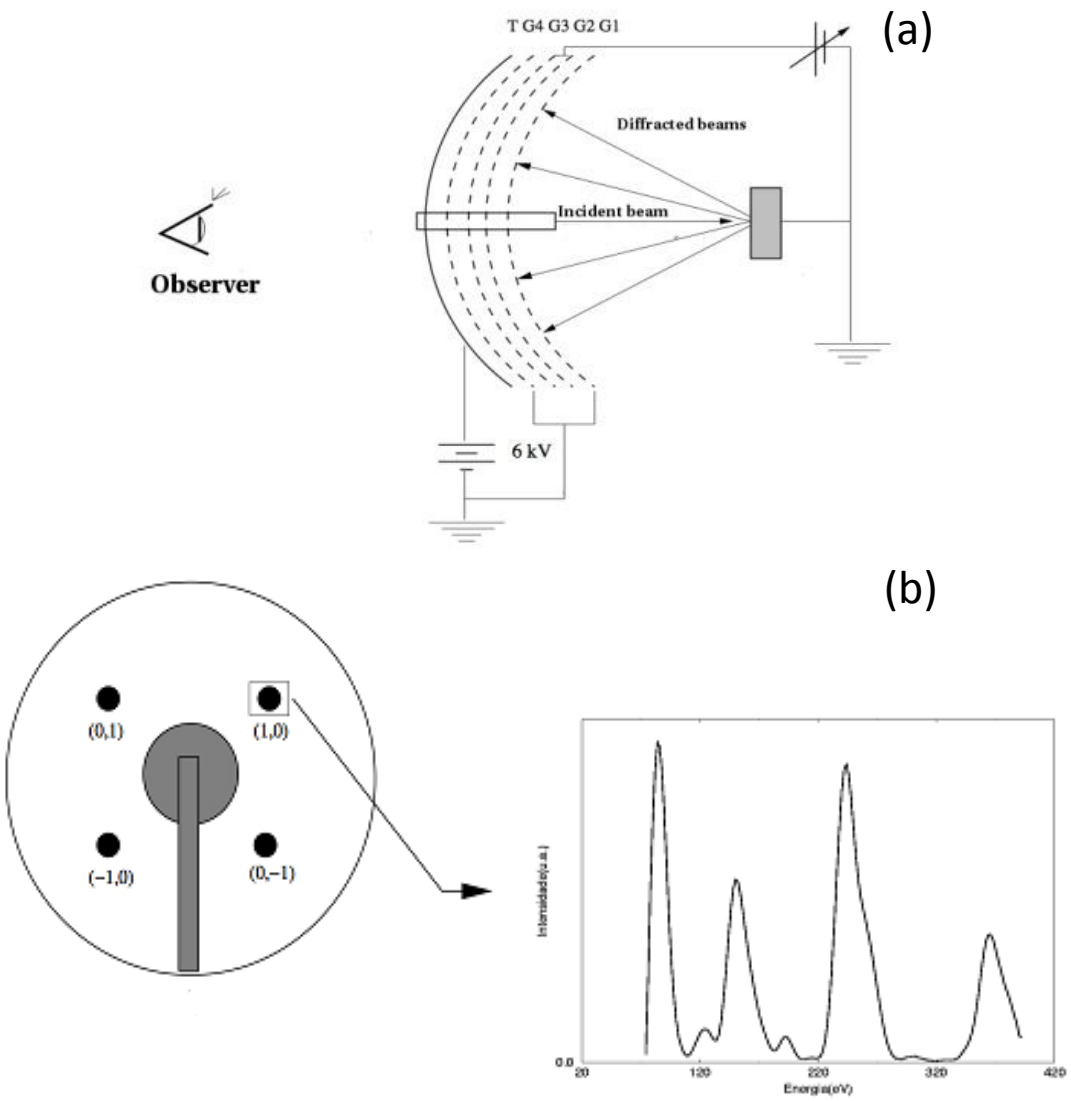

Figure 2.3 (a) Scheme of Retarding Field Analyzer; (b) A typical experimental *I-V* curve collection. Figures adapted from [83]

is a typical scheme of an experimental *I-V* curves collection.

The first step in the procedure of LEED analysis is to set up a model surface structure, which is chosen to be consistent with the bulk terminated structure. In the second step, the calculations using a multiple-scattering theory produce theoretical *I-V* curves, which are compared to the experimental results. The Pendry reliability factor (*R*p) is used to quantitatively describe the experimental and theoretical comparison [84]. The lower R_p factor acquired, the more reliable is surface structural determination. Usually, it is confident if $R_p \leq 0.3$. A modified version of the

symmetrized automated tensor LEED code (SATLEED) was applied in our theoretical calculation [85]. Atomic phase shifts were calculated via the optimized muffin-tin potential approximation method [86]. Debye temperatures for each element in the unit cell were determined from the isotropic mean-square displacements obtained from XRD results.

2.3 Physical Properties Measurement Methods and Analytical Procedures

2.3.1 Resistivity and Hall Coefficient

Electrical resistivity, magnetoresistivity and Hall coefficient measurements are conducted in a commercial Quantum Design Physical Properties Measurement System (PPMS) with a temperature range from 2 K to 400 K. The resistivity, $\rho(T)$, of the crystal is measured as a function of temperature or field using the standard four-probe method in PPMS. As shown in Figure 2.4 (a), a current I is applied via two leads parallel to *ab* plane and passes through the entire transverse cross-section area for measuring ρ_{ab}. The potential difference is measured by two leads (V+ and V-). For out-of-plane resistivity ρ_c (Figure 2.4 (b)), two ring-shaped current contacts are mounted on the opposite *ab* faces. The two voltage contacts are pointlike positioned in the center of rings. For transverse and longitudinal magnetoresistance (MR) measurements, the magnetic field H is applied perpendicular and parallel to the injected current I, respectively.

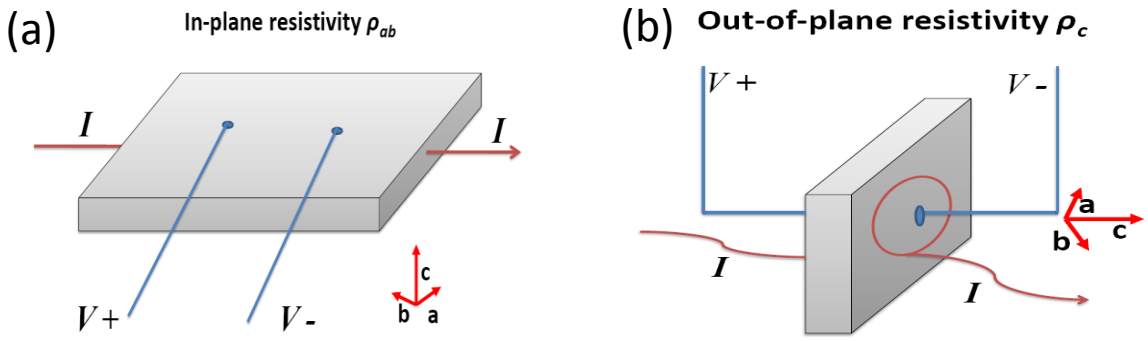

Figure 2.4 Schemes of the measurements for in-plane resistivity ρ_{ab} (a) and out-of-plane resistivity ρ_c (b).

Resistivity measurement is a direct method to classify metal, semiconductor and insulator. It provides information about scattering process when carriers flow in a given system. Fermi liquid theory, dealing with the effects of electron-electron interactions, was postulated by Landau in 1957 [87]. In Landau's theory, the low-lying single particle excitations of the system of interacting electrons are called quasiparticles; they have a one-to-one correspondence with the single particle excitations of the free electron gas and well-defined charge and momentum [88]. Being different from the eigenstates of a Fermi gas, these quasiparticles are not stationary and decay due to the electron-electron collisions. The effective collision cross section σ is

$$\sigma \approx \left(k_B T / \varepsilon_F\right)^2 \sigma_0 \qquad (3)$$

where k_B is Boltzmann constant, ε_F is Fermi energy, σ_0 is the cross section for the electron-electron interaction. The resistivity of a Fermi liquid is concomitant with the aforementioned collision cross section and therefore proportional to AT^2, where A is the Fermi liquid coefficient, which is related to the effective quasiparticle mass M^*. Considering a real metallic system, a residual resistivity term ρ_0 is added so that $\rho(T) = \rho_0 + AT^2$ at sufficiently low temperatures. The resistivity varying as T^2 at low temperature is often taken as an experimental evidence for Fermi liquid behavior. As displayed in the Figure 2.5, a quadratic temperature dependence below 6 K was observed in both $\rho_{ab}(T)$ and $\rho_c(T)$ in $Sr_3Ru_2O_7$, which is the characteristic of a Fermi liquid. If fitting $\rho_{ab}(T)$ via a formula $\rho_{ab}(T) = \rho_0 + AT^2$ below 6 K, where ρ_0 is the resistivity due to elastic scattering at $T = 0$ and A is a temperature-independent coefficient, values of $\rho_0 = 2.8\ \mu\Omega$ cm and $A = 0.075\ \mu\Omega$ cm/K^2 are obtained [38].

The Hall Effect is the production of a voltage difference (Hall potential) across an electrical conductor, transverse to an electric current in the conductor when a magnetic field is applied perpendicular to the current. As shown in Figure 2.6, the current, *I*, is applied in the *ab* plane and passes through the entire cross-section area and the magnetic field, *H*, is applied perpendicular to the

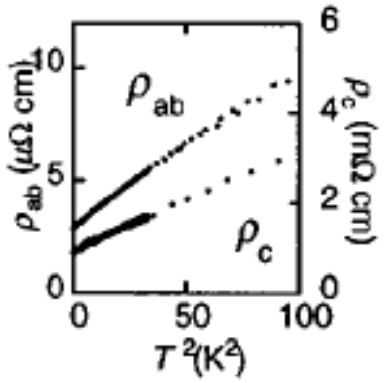

Figure 2.5 The low-temperature electrical resistivity ρ_{ab} and ρ_c against the square of temperature T^2 in $Sr_3Ru_2O_7$. Figure adapted from [38]

ab plane, thus holes accumulate on one side of the sample and electrons on the other side, leading to a potential difference which is called Hall potential. The sign of the Hall potential generally indicates the type of conducting charge carriers. The magnitude of the Hall potential is related to the density of charge carriers in the sample. The Hall coefficient R_H is defined by

$$R_H = {E_h}/{jH} = {V_h A}/{IlH} \qquad (4)$$

where E_h is the Hall field, V_h is the Hall potential, j is the current density given I/A, and l is the separation of the transverse voltage leads [89]. It can also be shown that $R_H = (nq)^{-1}$, with n representing the number of charge carriers concentration in the sample, and q representing the charge of the carriers. We adopt four-probe method to perform the Hall resistance ($R = V_h/I$) measurement via the AC Transport Measurement System (ACT) option in PPMS to obtain Hall coefficient. ρ_H is varying with the magnetic field H. The data must be collected by reversing the direction of the field to eliminate longitudinal contribution. Therefore, a plot of ρ_H versus H for a simple metal will yield a straight line with slope = R_H [89].

2.3.2 Specific Heat Measurement

The specific heat measurement is performed using a thermal relaxation method from 2 K to

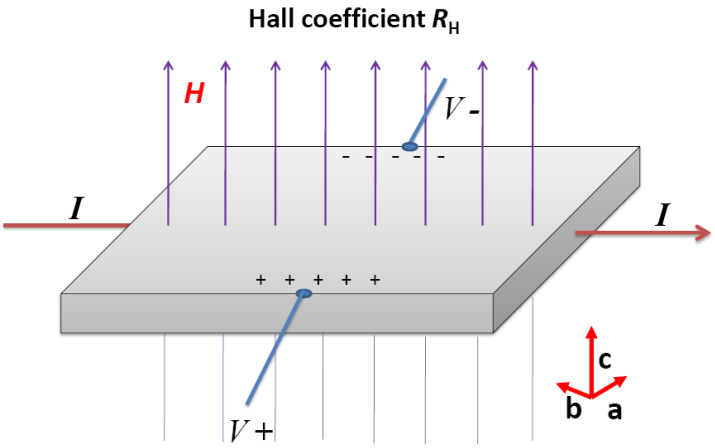

Figure 2.6 Scheme of measurement for Hall coefficient R_H.

300 K in PPMS. Figure 2.7 (a) shows a schematic diagram of specific heat measurement [89, 90]. The sample sits on a platform and thermal contact between this platform and the sample is kept by thin layer of grease. The platform is put in a thermal bath, and is connected with the puck by a wire of known conductivity (K_w). A thermometer and a heater are mounted underneath the sample platform. The whole setup is located in a high-vacuum chamber. A constant power P_0 is applied from the heater for a certain amount of time and this heating period is followed by a relaxation period of the same duration (P = 0 during relaxation). The total heat capacity of the sample and the platform is

$$C\frac{dT}{dt} = -K_w(T - T_p) + P(t) \qquad (5)$$

where T_p is temperature of the puck. The platform achieves equilibrium within time τ. The temperature in time t is given by

$$T(t) = T(0)\left(1 + \Delta T \exp(-t/\tau)\right) \qquad (6)$$

where $\Delta T = P_0/K_w$. It can be inferred from equation (5) and (6) that heat capacity $C = K_w\tau = P_0\tau/\Delta T$. Thus, C can be obtained by measuring the relaxation of the sample temperature. Figure 2.7 (b) is a

typical record of measured temperature as a function of time (t). The heat capacity of addenda (platform and N type of grease) without a sample, $C_{addenda}(T)$, must be measured before the measurement of the total specific heat of the sample and addenda, $C_{total}(T)$. Thus, the heat capacity of the sample is the difference of these two measurements: $C_{sample}(T) = C_{total}(T) - C_{addenda}(T)$ [89, 90].

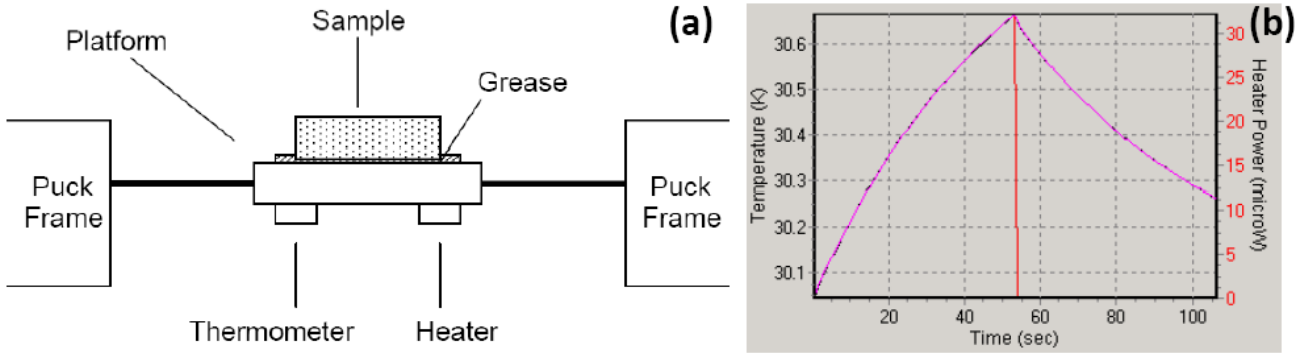

Figure 2.7 (a) Setup of heat capacity measurement via a relaxation method; (b) Record of measured temperature varying as time. Figure adapted from [89, 90]

Specific heat measurement is an ideal tool to directly probe phase transitions. When there is a first order phase transition associated with latent heat, the heat capacity is, in principle, infinite at the transition temperature. In real system, a very narrow sharp peak emerges at the transition temperature. If the system undergoes a second-order phase transition, a broad anomaly in specific heat appears at the transition temperature. As demonstrated in Figure 2.8, a jump in the specific heat of a superconductor is observed at the transition temperature T_c [91].

2.3.3 Magnetization and Susceptibility

The DC magnetization of samples is measured with a commercial superconducting quantum interference device (SQUID) magnetometer [92]. The SQUID consists of Josephson junctions, which form a ring, as shown in Figure 2.9. A current will tunnel through the junction when there is

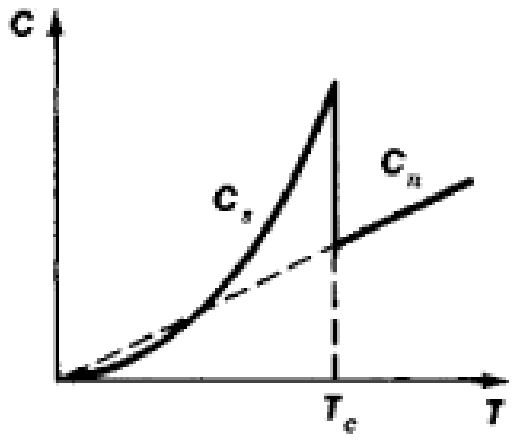

Figure 2.8 Jump in the specific heat of a superconductor at the transition temperature T_c. C_s represents specific heat in the superconducting state; C_n represents specific heat in the normal state. Figure adapted from [91]

no applied voltage. When a voltage is applied, the current will decrease and oscillate proportionally with voltage. The current through the loop depends on the *phase difference* $\Delta\varphi$ of the two superconducting wave functions. The time derivative of $\Delta\varphi$ is correlated with the voltage across the junction. $\Delta\varphi$ is additionally influenced by the magnetic flux Φ through this ring. By linearly changing the flux passing through the ring the circulating current will vary with a sinusoidal signature. The change in current is detected by the counter in the form of voltage pulses. Every voltage peak equates to an increase in one flux quanta. Thus such a system can be used to convert electrical voltage into magnetic flux. The sample is mounted in a plastic straw and fixed onto one end of a metal rod. The sample can be moved up and down through a set of pickup coils, which are connected to the SQUID with superconducting wires. Voltages are read as a function of the sample's position in the pickup coils [92]. The maximum applied magnetic field in SQUID is 7 T and the measured temperature range is 2 K – 400 K. The measurements are taken under both zero-field cooling (ZFC) and field cooling (FC) conditions. ZFC condition means that the field is applied after cooling the sample down to the lowest measured temperature and then the data are collected upon warming process. FC condition means the data are collected upon cooling process under an applied

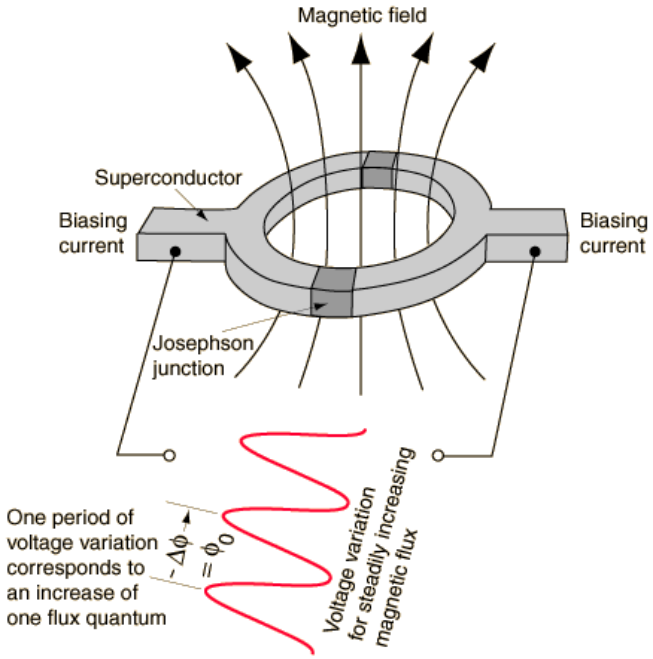

Figure 2.9 Scheme of demonstrating SQUID working principle. Figures adapted from [93]

field.

2.3.4 Elastic Neutron Scattering

Neutron scattering is a powerful technique to investigate the lattice and magnetic structures, lattice dynamics and spin excitations of condensed matter system. Compared with electrons and X-ray, neutrons have many unique properties. Due to charge neutrality, neutrons do not have Coulomb interaction with atoms in the solid and penetrate deeply into the bulk. Neutrons are ideal tool to probe magnetic moment in the solid because a neutron has 1/2 spin with a magnetic moment -1.913 μ_N. The wavelength of thermal neutrons is comparable to the interatomic distance. The energy of thermal neutrons is at the same order of the element excitations in the condensed matter system, making it accessible for the inelastic neutron scattering measurements to probe the element excitations. The basic properties of neutrons are listed in Table 2.1 [94]. Figure 2.10 shows the

geometry of neutron scattering experiment. The sample is usually a collection of atoms. The effective scattering area of each atom to an incident neutron can be expressed as cross-section.

Table 2.1 Basic Properties of Neutrons

Mass	M*n*=1.675 x 10^{-27} *kg*
Charge	0
Spin	½
Magnetic moment	-1.913 μ_N
Energy	
Cold neutron	0.1–10 meV
Thermal neutron	5–100 meV
Hot neutron	100–500 meV

The partial differential cross section can be described as the following:

$d^2\sigma/d\Omega_f dE_f$ = (neutrons scattered sec^{-1} into $d\Omega$ in direction θ, φ with final energy between E and E+dE)/(Φ $d\Omega$)

where Φ is the flux of incident neutrons $area^{-1}time^{-1}$, E is the scattered neutron energy. The detailed derivation of cross section in neutron scattering can be found in Ref. [94].

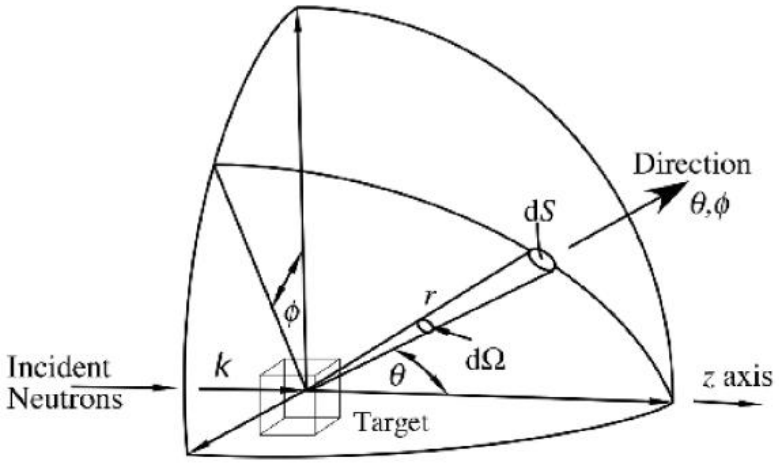

Figure 2.10 Geometry of neutron scattering experiment. Figure adapted from [94]

Any scattering process must satisfy the basic principles of energy and momentum conversation.

$$\vec{Q} = \vec{k}_f - \vec{k}_i \qquad (7)$$

$$\left|\vec{Q}\right| = k_f^2 + k_i^2 - 2k_i k_f \cos\theta_s \qquad (8)$$

$$\hbar\omega = E_i - E_f = \frac{\hbar^2}{2m_n}(k_f^2 - k_i^2) \qquad (9)$$

where the magnitude of the wave vector $k = 2\pi/\lambda$, λ is the wavelength of the neutron beam, m_n is the mass of neutron. The momentum transferred to the crystal is $\hbar\vec{Q}$. The subscript *I* and *f* are for the beam incident on and diffracted beam from the sample, respectively. For the elastic neutron scattering, $E_i = E_f$ and $\left|\vec{k}_i\right| = \left|\vec{k}_f\right| = k$. Here we consider only the Bragg scattering from which we can extract structural information. In scattering process, many different planes within the crystal, satisfying Bragg's law, must be considered. So the equations (7) and (9) can be rewritten as:

$$E_i = E_f \qquad (10)$$

$$\vec{Q} = \vec{k}_f - \vec{k}_i = \vec{G}_{hkl} = h\vec{b}_1 + k\vec{b}_2 + l\vec{b}_3 \qquad (11)$$

where $\vec{G}_{hkl}$ is a reciprocal lattice vector labeled by Miller indices *H*, *k*, and *l* with $\vec{b}_i$ as the respective axis vectors of the reciprocal lattice.

Figure 2.11 (a) is a schematic representation of the setup of a triple-axis neutron scattering spectrometer. Triple axis corresponds to the monochrometer, sample and analyzer axis, respectively. The initial and final neutron energies are determined by exploiting the process of Bragg diffraction from the monochromator and analyzer single crystals. This is achieved by rotating the crystals about their respective vertical axes until Bragg's condition for constructive interference is satisfied. As shown in Figure 2.11 (b), HB-1A is a fixed-incident-energy triple-axis spectrometer at the High Flux

Isotope Reactor (HFIR) at Oak Ridge National Laboratory (ORNL). HB-1A is a spectrometer probing elastic neutron scattering and does not involve any energy transfer. The spectrometer is operated with fixed incident energy (14.6 meV) using a double pyrolytic graphite monochromator system. Two highly oriented pyrolytic graphic filters (HOPG), one after each monochromator, are used to reduce $\lambda/2$ contamination. The typical energy resolution is ~ 1 meV. The more detailed instrument specifications about HB-1A can be found in Ref. [95].

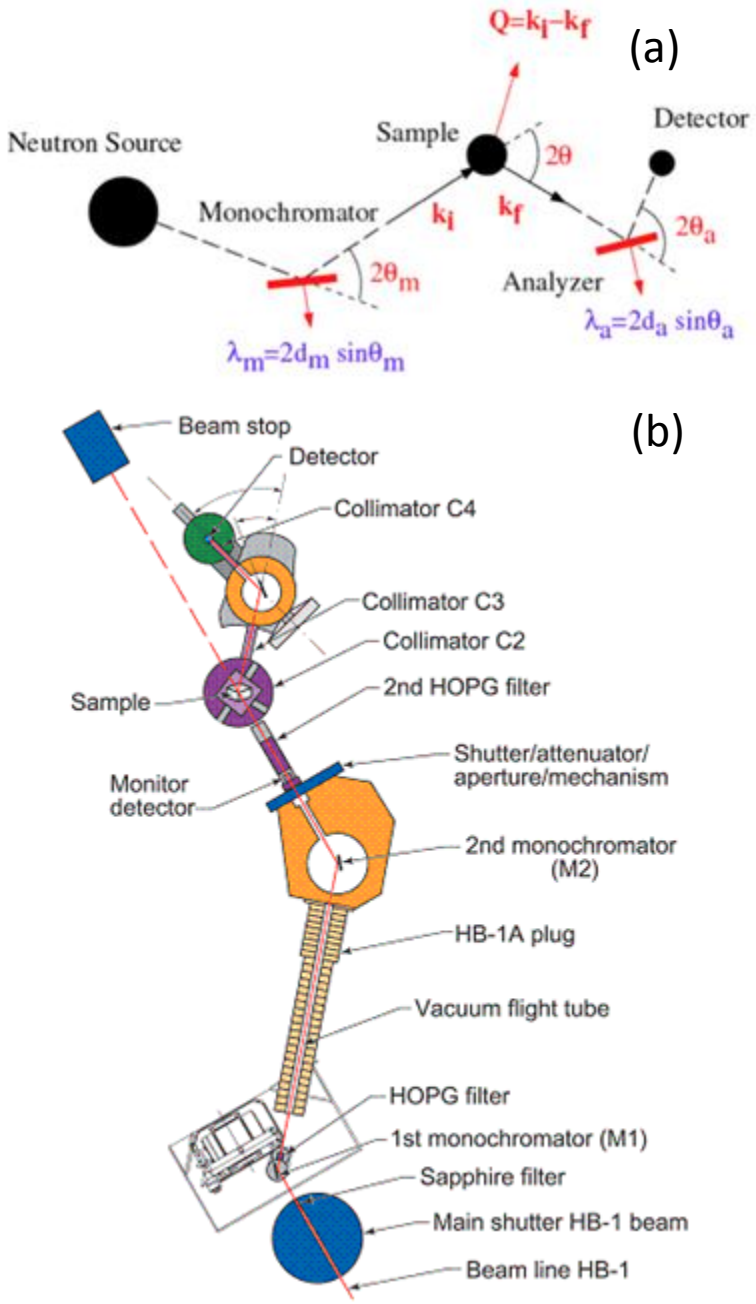

Figure 2.11 Schematic representation of the setup of a triple-axis neutron scattering spectrometer (a). Scheme of HB-1A triple-axis spectrometer at HFIR, ORNL (b). Figure adapted from [95]

Chapter 3 $Sr_3(Ru_{1-x}Mn_x)_2O_7$ Crystal Growth

As mentioned in Chapter 1, the quality of sample plays a key role in the discovery of exotic phenomena in strongly correlated materials. In ruthenium-based RP series, the superconductivity in Sr_2RuO_4 is extremely sensitive to the impurity and the quantum critical behavior in $Sr_3Ru_2O_7$ can only be observed in ultrapure single crystals [29, 48]. Thus it is very important to find an ideal growth method to grow strontium ruthenate single crystals. Flux method, in which components of the desired starting materials are reacted in a solvent, has been used to grow strontium ruthenates [96, 97]. Its advantages are growing the desired crystals below its melting temperature and suitable for materials with incongruent melting points. However, the crystals grown by flux growth method may have impurities from the flux or the container such as crucible used in the growing process. To avoid the above disadvantages in growing ruthenates via the flux method, we use floating zone technique (FZT) to grow the high quality single crystals. The detailed process of single crystal growth of strontium ruthenates using FZT was described in the following sections.

3.1 Material Preparation

The first step for FZT growth is to make a cylindrical polycrystalline rod, so-called feed rod, which is synthesized via a conventional solid-state reaction method. Due to evaporation of RuO_2 at high temperatures (> 1000 ℃), excess Ru was added when preparing the polycrystalline powder. For $Sr_3Ru_2O_7$ growth, we use the ratio of Sr : Ru = 4 : 3 in the starting materials, which has been proven to produce high quality $Sr_3Ru_2O_7$ single crystals and effectively compensate the partial loss of Ru. It can also avoid intergrowths of Sr_2RuO_4 and $Sr_4Ru_3O_{10}$ [98]. The hygroscopic $SrCO_3$ powder is baked at 400 ℃ for approximately 6 hours to remove moisture before the use. $SrCO_3$ and Ru powder is precisely weighed with a molar ratio $SrCO_3$: Ru = 4:3, then ground in air with a ball mill for several hours. The mixture is then put in an alumina crucible and heated 1300 ℃ for 36

hours in a tube furnace in a flow of O_2. The temperature is brought to this point at a rate of 125 ℃/h. The sample is then pulled out of the hot furnace and quenched on an Al plate. The temperature profile is shown in Figure 3.1 (a). The resulting materials are reground and filled in a rubber tube (We use a Latex balloon in our experiment) using a funnel, as shown in Figure 3.2 (a). The balloon is tied at the ends, then wrapped by a moderately rigid A4 blank paper and rolled over on a flat surface on the table back and forth to give a cylindrical shape. As shown in Figure 3.2 (b), the balloon is placed inside a water-filled pressure cell and subjected to a hydrostatic pressure of 50 MPa. The pressure is slowly reduced to zero and the balloon is taken out of pressure cell with a great caution. The balloon is then removed and a feed rod with a length approximately 8 - 10 cm comes out, as shown in Figure 3.1 (b). Then the feed rod is placed on a thin layer of prepared strontium ruthenate bedding powder on top of an alumina crucible and sintered in air at 950 ℃ for 12 hours. For the growth of Mn-doped $Sr_3Ru_2O_7$ single crystals, MnO_2 powder is added in the starting materials with a partial substitution of Ru in a molar ratio $N(MnO_2) : N(Ru) = x : 1\text{-}x$ in all cases. In other words, the ratio $N(SrCO_3)$ **:** $(N(Ru) + N(MnO_2)) = 4 : 3$ remains in synthesizing Mn-doped $Sr_3Ru_2O_7$. The procedure of synthesis of polycrystalline powders and making feed rod for Mn-doped compound is similar to the one described above for the pure compound.

3.2 Single Crystal Growth

We optimize multiple variables to achieve successful growth for specific compounds. The atmosphere condition, the pressure P and the crystal growth speed V_1 are the primary variables, which usually remains unchanged during the growth and largely determine the nature of the crystal [98]. The traveling speed of feed rod V_2, the lamp power W and the rotation speed of rods ω are secondary variables [98]. For the growth of $Sr_3Ru_2O_7$ and Mn-doped compounds, we use a typical speed of 15mm/hr for V_1, approximately 25 mm/hr for V_2, a rotation speed of ω = 20 rpm for both

(a)

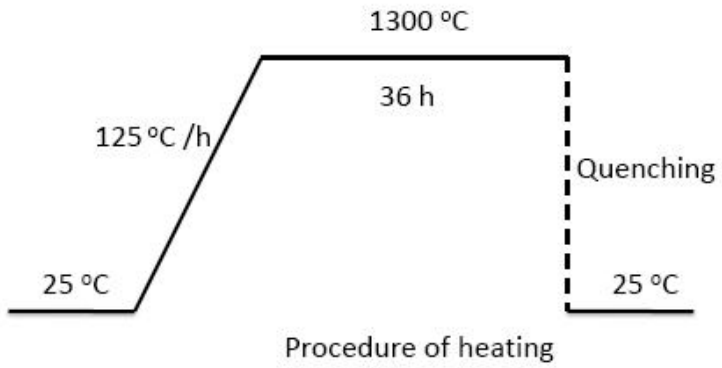

(b)

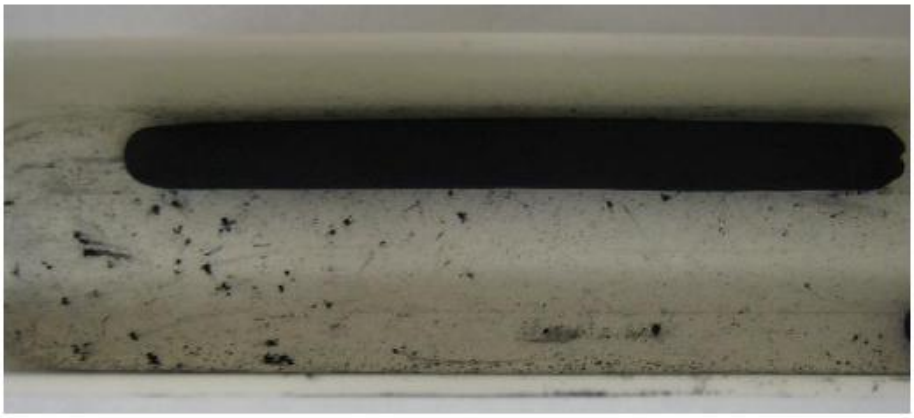

Figure 3.1 (a) Procedure of heating initial powder mixture in tube furnace. (b) Picture of a pressed polycrystalline feed rod with nominal $x = 0.1$.

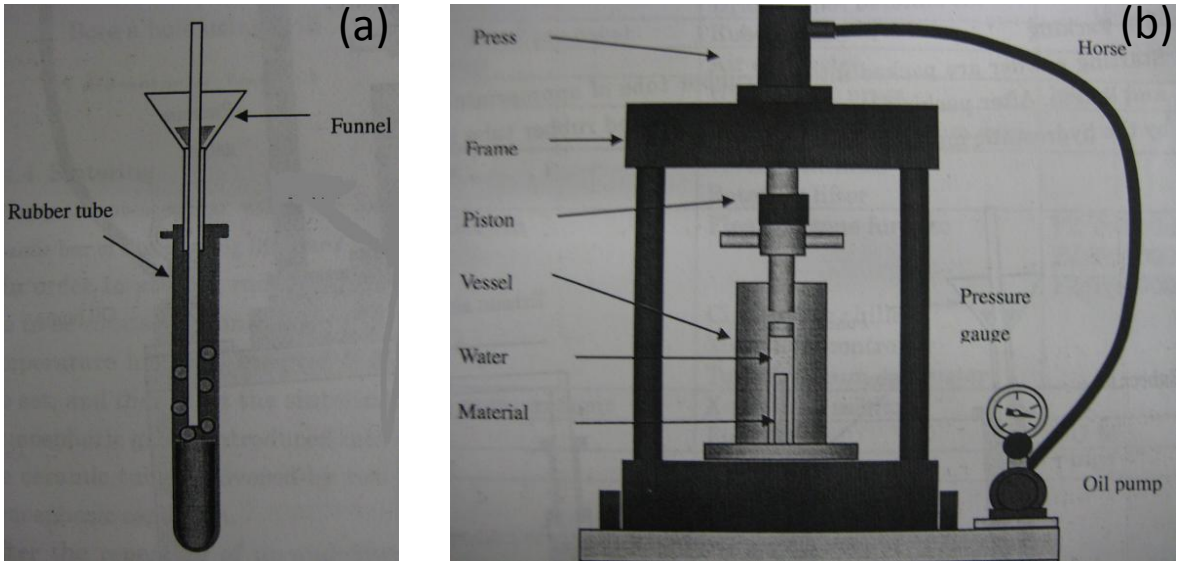

Figure 3.2 (a) Configuration of packing the powders into a rubble tube through a funnel. (b) The packed rubble tube is put into the vessel and pressed by the hydrostatic press method using water. The applied pressure is monitored by the pressure gauge.

the feed and seed rod, and adopt an atmosphere of 50% oxygen and 50% argon under a total pressure about P = 10 bar. We may change the primary and secondary variables and atmosphere in specific growth. A typical as-grown single crystal with a length of several centimeters is shown in Figure 3.3.

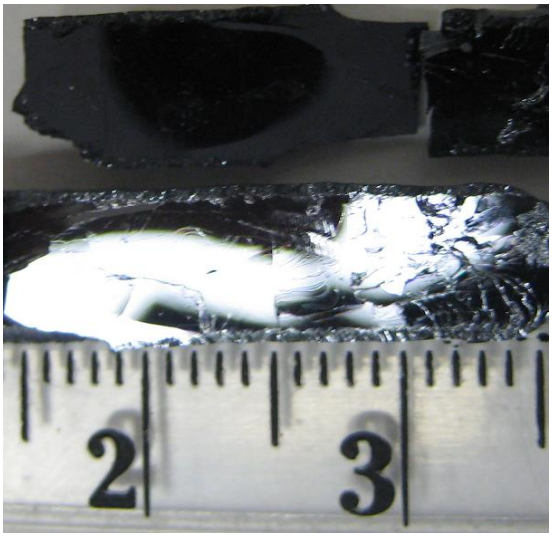

Figure 3.3 Picture of a single crystal with nominal x = 0.1 (actual 0.16) grown by FZT. The shiny face in the picture is the *ab* plane. The scale is in cm.

Chapter 4 Crystallographic Structures of $Sr_3(Ru_{1-x}Mn_x)_2O_7$ ($0 \leq x \leq 0.7$)

4.1 Powder X-ray Diffraction

We use powder XRD to check the phase of as-grown single crystals. The powder XRD diffraction patterns in pulverized single crystal $Sr_3Ru_2O_7$ and $Sr_3(Ru_{0.84}Mn_{0.16})_2O_7$ at room temperature are shown in Figure 4.1 (a) and (b), respectively. The standard patterns are based on our refined tetragonal unit cell with $a = b = 3.889$ Å, $c = 20.732$ Å for $Sr_3Ru_2O_7$ (See Section **4.2**) and with $a = b = 3.911$ Å, $c = 20.456$ Å for $Sr_3(Ru_{0.84}Mn_{0.16})_2O_7$ (See **Appendix A5**). All peaks in Figure 4.1 (a) and (b) exactly correspond to the indices of standard $Sr_3Ru_2O_7$ pattern under the tetragonal space group *I*4/*mmm*. Therefore, the powder XRD pattern indicates the pure phase without any intergrowth of Sr_2RuO_4, $Sr_4Ru_3O_{10}$ or $SrRuO_3$.

4.2 Bulk Crystal Structures of $Sr_3(Ru_{1-x}Mn_x)_2O_7$ ($0 \leq x \leq 0.7$)

The understanding of the crystallographic structures is a prerequisite to study functionalities between crystal structure and the physical properties such as magnetism and electrical resistivity. As mentioned in Chapter 1, crystal structure of $Sr_3Ru_2O_7$ has been known for a long time and indexed in different space groups, *I.e.*, tetragonal space group *I*4/*mmm* (No. 139) [39] or orthorhombic space group *Pban* (No. 40) [40] or *Bbcb* (No. 68) [42]. According to previous neutron-powder-diffraction study, the refined structural parameters depend not only on temperature but also on thermal cycling [41]. We studied temperature dependence of bulk crystal structures on $Sr_3Ru_2O_7$ single crystal via single-crystal XRD technique. Table 4.1 shows the crystallographic parameters for $T = 298$, 200, and 90 K from the first thermal cycle. The $Sr_3Ru_2O_7$ crystal structure is best modeled with the tetragonal space group *I*4/*mmm* (No. 139) with Sr1 (4/*mmm*), Sr2 (4*mm*), Ru (4*mm*), O1 (4/*mmm*), O2 (4*mm*), and O3 (*M*). Figure 4.2 (a) is the bulk unit cell representation of $Sr_3Ru_2O_7$. The structure consists of

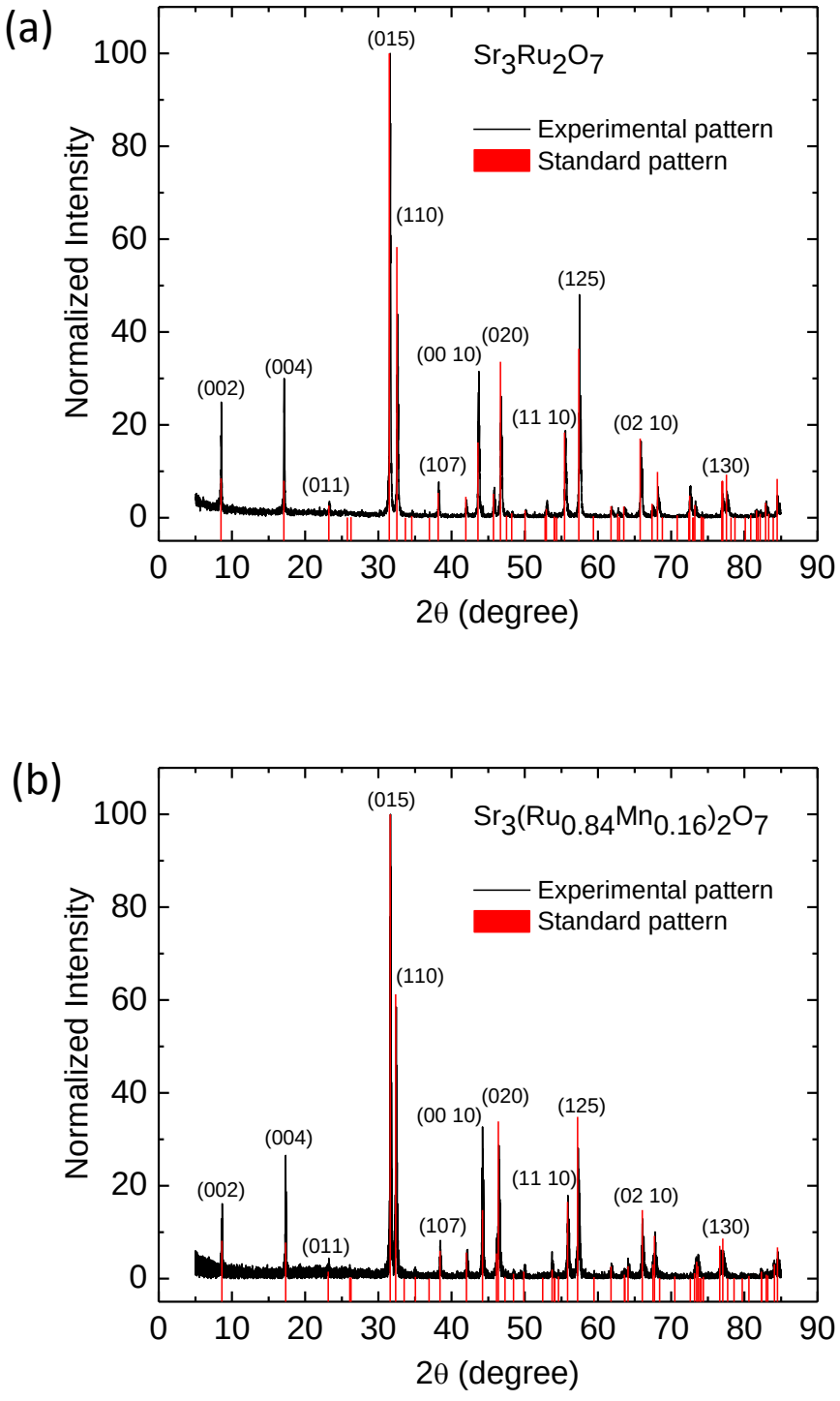

Figure 4.1 The powder X-ray diffraction pattern of $Sr_3Ru_2O_7$ (a) and $Sr_3(Ru_{0.84}Mn_{0.16})_2O_7$ (b). Black line represents experimental intensity while red columns indicate calculated Bragg peak positions and intensity using the *I*4/*mmm* space group. The peaks are indexed in a tetragonal structure.

two layers of corner sharing RuO_6 octahedra interleaved with SrO layers, *I.e.*, $SrO(SrRuO_3)_n$ ($n = 2$). Ru atoms are located in the center of each octahedron with the crystallographic *c*-axis in the vertical direction. Because of the large atomic displacement parameters found the equatorial oxygen atoms, we allowed the atomic position and the occupancy of O3 to be refined. The results of this refinement lead to changing the Wyckoff position from 8*g* to 16*n* and the split occupancy for O3. The atomic displacement parameters for data collected at 298 K yielded a 75% reduction in the anisotropic parameter, U^{22}, of O3 after decreasing the occupancy of the 8*g* site to 0.5 and refining the previously fixed atomic *y* coordinate, as shown in Table 4.2. At room temperature, the O3 position (16*n* site) is 0.23 Å away from the mirror plane corresponding to an octahedral rotation of 6.7(6)° (see Figure 4.2(b)), which is in good agreement with the rotational angles reported in Refs. 40 and 42. However, both the reported structural models using neutron powder diffraction adopt a lower symmetry (orthorhombic) space groups to model $Sr_3Ru_2O_7$ (*i.e. Pban* [40] and *Bbcb* [42]). Looking for the superlattice or weak reflections that might justify lowering the symmetry to one of these reported orthorhombic space groups, two other single crystals were examined with longer data collection time. The absence of superlattice intensities in our XRD data and the ability to model the octahedral rotation with split occupancy of the equatorial O3 atoms allow us to describe the bulk $Sr_3Ru_2O_7$ structure with the higher symmetry space group, *I*4/*mmm*, instead of *Pban* or *Bbcb*. Attempts to model our XRD data with an orthorhombic space group result in divergence of the refinement. Application of a series of suggested space group transformations to resolve the missing symmetry issue ultimately led to modeling the data with the tetragonal space group, *I*4/*mmm*. The data collected at three different temperatures, as shown in Tables 4.1 – 4.4, converge with $R_1 \sim 3\%$ and a final difference map of < 2 eÅ^{-3} with well-behaved atomic displacement parameters.

Table 4.4 provides selected interatomic distances of $Sr_3Ru_2O_7$. As the temperature is

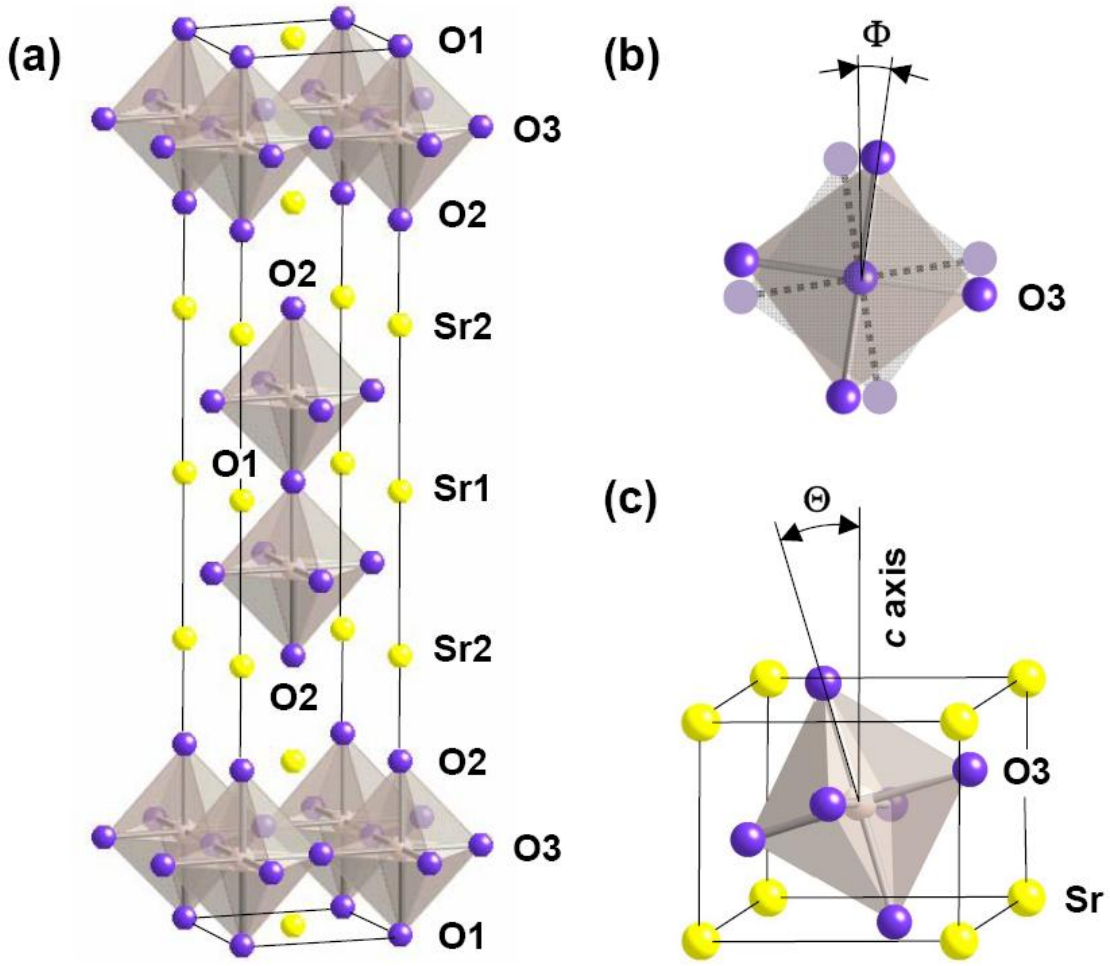

Figure 4.2 (a) Unit-cell representation of $Sr_3Ru_2O_7$ using space group *I*4/*mmm*. The Ru atoms are located in the center of each octahedron. (b) Top view of the RuO_6 octahedron showing the rotation angle (Φ) in the *ab* plane (The dash lines present mirror planes. (c) View of the RuO_6 octahedron showing a tilt angle (Θ). For bulk, Θ = 0.

Table 4.1 Crystallographic Parameters of Crystal with $x = 0$

Crystal data			
Temperature (K)	298(2)	200(2)	90(2)
Formula	$Sr_3Ru_2O_7$	$Sr_3Ru_2O_7$	$Sr_3Ru_2O_7$
Crystal system	Tetragonal	Tetragonal	Tetragonal
Space group	*I*4/*mmm* (No. 139)	*I*4/*mmm* (No. 139)	*I*4/*mmm* (No. 139)
a (Å)	3.8897(10)	3.8800(15)	3.8716(10)
c (Å)	20.7320(60)	20.7669(70)	20.7980(80)
V (Å^3)	313.66(15)	312.70(20)	311.75(15)
Mosaicity ( )	0.427(6)	0.491(6)	0.471(6)
Z	2	2	2
Crystal dimension (mm^3)	0.03×0.08×0.08	0.03×0.08×0.08	0.03×0.08×0.08
2θ range ( )	7.86-54.72	7.84-54.88	7.84-54.68
μ (mm^{-1})	30.032	30.136	30.215
Data collection			
Measured reflections	363	360	345
Independent reflections	142	142	140
Reflections with $I>2\sigma(I)$	139	139	138
[a]R_{int}	0.0363	0.0605	0.0321
H	-5→5	-4→5	-5→5
k	-3→3	-4→5	-3→3
l	-26→23	-24→26	-24→26
Refinement			
Reflections	142	142	140
Parameters	21	21	21
[b]$R_1[F^2>2\sigma(F^2)]$	0.0300	0.0347	0.0318
[c]$wR_2(F^2)$	0.0878	0.0909	0.0802
[d]S	1.314	1.245	1.237
$\Delta\rho_{max}$ (eÅ^{-3})	1.595	1.928	2.214
$\Delta\rho_{min}$ (eÅ^{-3})	-1.077	-1.739	-1.695

[a]$R_{int} = [\Sigma | F_o^2 - F_c^2 \text{ (mean)} | / (n\text{-}p)]^{1/2}$

[b]$R_1 = \Sigma | | F_o | - | F_c | | / \Sigma | F_o |$

[c]$wR_2 = [\Sigma [w(F_o^2 - F_c^2)^2] / \Sigma [w(F_o^2)^2]]^{1/2}$,
$w = 1 / [\sigma^2(F_o^2) + (0.0495P)^2 + 0.6876P]$ for 298 K,
$w = 1 / [\sigma^2(F_o^2) + (0.0573P)^2 + 0.0000P]$ for 200 K,
$w = 1 / [\sigma^2(F_o^2) + (0.0525P)^2 + 0.0172P]$ for 90 K

[d]$S = [\Sigma [w(F_o^2 - F_c^2)^2] / \Sigma (n - p)]^{1/2}$

Table 4.2 Atomic Positions and Equivalent Isotropic Displacement Parameters of Crystal with $x = 0$

Atom	Wyckoff position	x	y	z	Occ.[a]	U_{eq} (Å^2)[b]
T = 298 K						
Sr1	2*b*	1/2	1/2	0	1	0.0071(6)
Sr2	4*e*	1/2	1/2	0.18626(9)	1	0.0070(6)
Ru1	4*e*	0	0	0.09741(5)	1	0.0034(6)
O1	2*a*	0	0	0	1	0.013(3)
O2	4*e*	0	0	0.1958(5)	1	0.013(2)
O3	16*n*	1/2	0.059(5)	0.0964(3)	0.5	0.013(5)
T = 200 K						
Sr1	2*b*	1/2	1/2	0	1	0.0050(6)
Sr2	4*e*	1/2	1/2	0.18634(8)	1	0.0049(6)
Ru1	4*e*	0	0	0.09740(5)	1	0.0023(6)
O1	2*a*	0	0	0	1	0.008(3)
O2	4*e*	0	0	0.1963(5)	1	0.0092(18)
O3	16*n*	1/2	0.066(3)	0.0967(2)	0.5	0.010(3)
T = 90 K						
Sr1	2*b*	1/2	1/2	0	1	0.0030(5)
Sr2	4*e*	1/2	1/2	0.18659(8)	1	0.0032(5)
Ru1	4*e*	0	0	0.09743(5)	1	0.0017(5)
O1	2*a*	0	0	0	1	0.005(2)
O2	4*e*	0	0	0.1958(5)	1	0.0062(16)
O3	16*n*	1/2	0.0707(18)	0.0969(2)	0.5	0.008(3)

[a] Occupancy of atoms

[b] U_{eq} is defined as one-third of the trace of the orthogonalized U^{ij} tensor.

Table 4.3 Anisotropic Atomic Displacement Parameters (Å^2) of Crystal with $x = 0$

Atom	U^{11}	U^{22}	U^{33}	U^{12}	U^{13}	U^{23}
T = 298 K						
Sr1	0.0077(7)	0.0077(7)	0.0059(11)	0.000	0.000	0.000
Sr2	0.0080(6)	0.0080(6)	0.0050(10)	0.000	0.000	0.000
Ru1	0.0038(6)	0.0038(6)	0.0025(8)	0.000	0.000	0.000
O1	0.018(4)	0.018(4)	0.003(7)	0.000	0.000	0.000
O2	0.016(3)	0.016(3)	0.005(4)	0.000	0.000	0.000
O3	0.006(4)	0.021(17)	0.013(4)	0.000(3)	0.000	0.000
T = 200 K						
Sr1	0.0058(7)	0.0058(7)	0.0035(11)	0.000	0.000	0.000
Sr2	0.0057(6)	0.0057(6)	0.0033(10)	0.000	0.000	0.000
Ru1	0.0027(6)	0.0027(6)	0.0015(8)	0.000	0.000	0.000
O1	0.008(3)	0.008(3)	0.009(7)	0.000	0.000	0.000
O2	0.011(2)	0.011(2)	0.005(4)	0.000	0.000	0.000
O3	0.006(3)	0.013(11)	0.011(4)	-0.001(2)	0.000	0.000
T = 90 K						
Sr1	0.0038(6)	0.0038(6)	0.0016(10)	0.000	0.000	0.000
Sr2	0.0038(5)	0.0038(5)	0.0019(9)	0.000	0.000	0.000
Ru1	0.0025(6)	0.0025(6)	0.0003(8)	0.000	0.000	0.000
O1	0.006(3)	0.006(3)	0.002(6)	0.000	0.000	0.000
O2	0.009(2)	0.009(2)	0.000(4)	0.000	0.000	0.000
O3	0.007(3)	0.010(8)	0.006(4)	-0.001(2)	0.000	0.000

Table 4.4 Selected Bond Distances (Å) and Angles (°) of Crystal with $x = 0$

	298K	200K	90K
Distances			
Sr1-O1	2.75065(14)	2.7436(2)	2.73792(14)
Sr1-O3 (×4)	2.635(15)	2.621(7)	2.613(6)
Sr2-O2	2.445(11)	2.438(11)	2.7446(7)
Sr2-O3 (×4)	2.534(15)	2.512(8)	2.891(6)
Ru1-O1	2.0195(11)	2.0227(11)	2.0263(10)
Ru1-O2	2.040(10)	2.053(11)	2.046(9)
Ru1-O3 (×4)	1.958(3)	1.9566(13)	1.9553(10)
Angles			
O1-Ru1-O3 (×4)	89.39(19)	89.56(14)	89.70(15)
O2-Ru1-O3 (×4)	90.61(19)	90.44(14)	90.30(15)
Rotation			
[a]RuO_6 octahedra	6.7(6)	7.5(3)	8.1(2)

[a] This value represents the rotational angle (Φ) for the RuO_6 octahedron. For a view of the rotational angles along the *ab*-plane, please see Figure 4.2(b).

decreased from 298 to 90 K, Ru-O1 (inner apical oxygen) bond distance increases from 2.0195(11) to 2.0263(10) Å. The Ru-O2 (outer apical oxygen) distance and the Ru-O3 (equatorial oxygen) distance do not statistically change within this temperature range. The octahedra are slightly distorted as evident by the small symmetrical buckling of the bond angles for O1-Ru-O3 (which is slightly less than 90˚) and O2-Ru-O3 (which is slightly greater than 90˚). The difference in O1-Ru-O3 and O2-Ru-O3 bond angles becomes smaller while lowering temperature. This indicates that the structure is less buckled at lower temperatures. Figure 4.2 (b) shows a top view of a RuO_6 octahedron at 298 K illustrating the O3-Ru-O3 bond angles with a rotational angle of 6.7(6)˚ off the mirror plane of the 2*mm* position. This RuO_6 octahedron rotational angle increases with decreasing temperature and reveals a rotation angle about 7.5(3)˚ and 8.1(2)˚ for 200 K and 90 K, respectively (see Table 4.4). There were no signs of octahedral tilt (see Figure 4.2 (c)) in the bulk.

We used the same method and procedure as that for $Sr_3Ru_2O_7$ to acquire diffraction patterns and refine the crystal structures for Mn-doped compounds. The evolution of concentration of Mn (x) in $Sr_3(Ru_{1-x}Mn_x)_2O_7$ crystals is investigated. The initial (nominal) molar ratio of $N(MnO_2)/N(Ru)$ is x' : (1-x') in starting mixture powder. Due to the evaporation of Ru at high temperatures, the actual occupancy (x) of Mn in Ru-site is changed in as-grown single crystals. Here we take an example in crystal with x'= 0.05. We collect single crystal XRD data at 298 K and 90 K. In refining the XRD data, Mn occupancy is one of refining parameters. The refinement yields a value of x = 0.08 for x' = 0.05. The refinement results of $Sr_3(Ru_{0.92}Mn_{0.08})_2O_7$ are shown in Table 4.5. Table 4.6 shows atomic positions and equivalent isotropic displacement parameters for x = 0.08 while anisotropic atomic displacement parameters are shown in Table 4.7. Table 4.8 shows selected bond distances and angles for x = 0.08. Comparing Table 4.4 and 4.8, in doping level x = 0.08, the RuO_6 rotation angle (5.7 ° at 298 K and 7.2 ° at 90 K) is smaller than that in pure $Sr_3Ru_2O_7$ (6.7 ° at 298 K and 8.1 ° at 90 K). The

less distorted structure in Mn-doped compound may result from the smaller ionic radii of Mn ion. Refined structural results for compounds with x = 0.06, 0.16, 0.2, 0.33 and 0.7 are listed in **Appendix A**. All Mn-doped compounds have a tetragonal structure in our measured temperatures, 298 K and 90 K.

Table 4.5 Crystallographic Parameters of Crystal with x = 0.08

Crystal data		
Temperature (K)	298(2)	90(2)
Formula	$Sr_3(Ru_{0.92}Mn_{0.08})_2O_7$	$Sr_3(Ru_{0.92}Mn_{0.08})_2O_7$
Crystal system	Tetragonal	Tetragonal
Space group	*I*4/*mmm* (No. 139)	*I*4/*mmm* (No. 139)
a (Å)	3.8980(20)	3.883(4)
c (Å)	20.60300(10)	20.658(1)
V (Å^3)	313.05(25)	311.5(3)
Mosaicity ( )	0.474(4)	0.593(3)
Z	2	2
2θ range ( )	7.9-60.0	7.9-60.0
μ (mm^{-1})	30.03	30.19
Data collection		
Measured reflections	857	1678
Independent reflections	177	177
Reflections with $I>2\sigma(I)$	171	171
[a]R_{int}	0.079	0.103
H	-5→5	-5→5
k	-5→5	-5→5
l	-28→27	-26→28
Refinement		
Reflections	177	177
Parameters	22	20
[b]$R_1[F^2>2\sigma(F^2)]$	0.027	0.032
[c]$wR_2(F^2)$	0.068	0.092
[d]S	1.19	1.26
$\Delta\rho_{max}$ (eÅ^{-3})	1.19	1.62
$\Delta\rho_{min}$ (eÅ^{-3})	-1.83	-1.75

[a]$R_{int} = [\Sigma | F_o^2 - F_c^2 \text{ (mean)} | / (n\text{-}p)]^{1/2}$

[b]$R_1 = \Sigma | | F_o | - | F_c | | / \Sigma | F_o |$

[c]$wR_2 = [\Sigma [w(F_o^2 - F_c^2)^2] / \Sigma [w(F_o^2)^2]]^{1/2}$,
$w = 1 / [\sigma^2(F_o^2) + (0.0338P)^2 + 1.0651P]$ for 298 K,
$w = 1 / [\sigma^2(F_o^2) + (0.0535P)^2 + 0.7793P]$ for 90 K

[d]$S = [\Sigma [w(F_o^2 - F_c^2)^2] / \Sigma (n - p)]^{1/2}$

Table 4.6 Atomic Positions and Equivalent Isotropic Displacement Parameters of Crystal with x = 0.08

Atom	Wyckoff position	x	y	z	Occ.[a]	U_{eq} (Å^2)[b]
T = 298 K						
Sr1	2*b*	1/2	1/2	0	1	0.0090(4)
Sr2	4*e*	1/2	1/2	0.18561(5)	1	0.0083(4)
Mn1	4*e*	0	0	0.09736(3)	0.091(10)	0.0038(4)
Ru1	4*e*	0	0	0.09736(3)	0.909(10)	0.0038(4)
O1	2*a*	0	0	0	1	0.0124(19)
O2	4*e*	0	0	0.1954(3)	1	0.0112(13)
O3	16*n*	1/2	0.050(6)	0.0965(2)	0.5	0.013(4)
T = 90 K						
Sr1	2*b*	1/2	1/2	0	1	0.0053(5)
Sr2	4*e*	1/2	1/2	0.18607(6)	1	0.0053(4)
Mn1	4*e*	0	0	0.09733(5)	0.08(1)	0.0034(5)
Ru1	4*e*	0	0	0.09733(5)	0.92(1)	0.0034(5)
O1	2*a*	0	0	0	1	0.008(2)
O2	4*e*	0	0	0.1950(5)	1	0.008 (2)
O3	16*n*	1/2	0.064(2)	0.0966(3)	0.5	0.008(2)

[a] Occupancy of atoms
[b] U_{eq} is defined as one-third of the trace of the orthogonalized U^{ij} tensor.

Table 4.7 Anisotropic Atomic Displacement Parameters (Å^2) of Crystal with x = 0.08

Atom	U^{11}	U^{22}	U^{33}	U^{12}	U^{13}	U^{23}
T = 298 K						
Sr1	0.0095(4)	0.0095(4)	0.0078(7)	0.000	0.000	0.000
Sr2	0.0095(4)	0.0095(4)	0.0060(6)	0.000	0.000	0.000
Mn1	0.0042(4)	0.0042(4)	0.0030(5)	0.000	0.000	0.000
Ru1	0.0042(4)	0.0042(4)	0.0030(5)	0.000	0.000	0.000
O1	0.018(3)	0.018(3)	0.001(4)	0.000	0.000	0.000
O2	0.015(2)	0.015(2)	0.003(2)	0.000	0.000	0.000
O3	0.005(3)	0.020(13)	0.014(3)	0.000(2)	0.000	0.000
T = 90 K						
Sr1	0.0062(5)	0.0062(5)	0.0034(8)	0.000	0.000	0.000
Sr2	0.0062(5)	0.0062(5)	0.0034(7)	0.000	0.000	0.000
Mn1	0.0041(5)	0.0041(5)	0.0019(7)	0.000	0.000	0.000
Ru1	0.0041(5)	0.0041(5)	0.0019(7)	0.000	0.000	0.000
O1	0.012(3)	0.012(3)	0.000(5)	0.000	0.000	0.000
O2	0.012(2)	0.012(2)	0.000(3)	0.000	0.000	0.000
O3	0.003(3)	0.009(7)	0.011(3)	0.001(2)	0.000	0.000

Table 4.8 Selected Bond Distances (Å) and Angles (°) of Crystal with $x = 0.08$

	298K	90K
Distances		
Sr1-O1	2.7563(3)	2.7457(3)
Sr1-O3 (×4)	2.65(2)	2.617(7)
Sr2-O2	2.452(7)	2.7518(7)
Sr2-O3 (×4)	2.82(2)	2.866(7)
Ru1-O1	2.0059(7)	2.011(1)
Ru1-O2	2.020(7)	2.017(9)
Ru1-O3 (×4)	1.959(2)	1.957(1)
Angles		
O1-Ru1-O3 (×4)	89.5(1)	89.5(2)
O2-Ru1-O3 (×4)	90.5(1)	90.5(2)
Rotation		
[a]RuO_6 octahedra	5.7(7)	7.3(3)

[a] This value represents the rotational angle (Φ) for the RuO_6 octahedra. For a view of the rotational angles along the *ab*-plane, please see Figure 4.2(b).

Figure 4.3 shows the Mn concentration (x) dependence of lattice parameters a (Figure 4.3 a), c (Figure 4.3 b), unit cell volume V (Figure 4.3 c) and ratio c/a (Figure 4.3 d) at 298 K and 90 K. Lattice parameter a reveals nonmonotonical behavior with x, first increasing with x in the range of $0 \leq x \leq 0.2$ and then decreasing with x above $x = 0.2$. Lattice parameter c, V and c/a decrease monotonically with increasing x and show a slope change at $x = 0.2$. The values of a, c, V and c/a at room temperature in the extreme Mn doping compound $Sr_3Mn_2O_7$ are shown as a solid square in Figure 4.3 a-d [74]. The refined bond lengths Ru-O(1) (Figure 4.3 e) and Ru-O(2) (Figure 4.3 f) decrease monotonically with increasing x at both 298 K and 90 K. Bond length Ru-O(3) (Figure 4.3 g) remains more or less constant. To understand the distortion of the octahedron with doping, the ratio of the averaged Ru-O bond lengths [Ru-O(1) and Ru-O(2)] to the equatorial Ru-O bond length [Ru-O(3)]: δ_{JT} = [Ru-O(1) + Ru-O(2)]/2 x Ru-O(3)] is calculated. As demonstrated in Figure 4.3 h, δ_{JT} shows a systematic change with x. The rotation angle of RuO_6 decreases with x and no rotation of

octahedral RuO_6 is found around x = 0.2, as shown in Figure 4.4. Based on the above structural analysis, we conclude that the concentration x = 0.2 is a turning point.

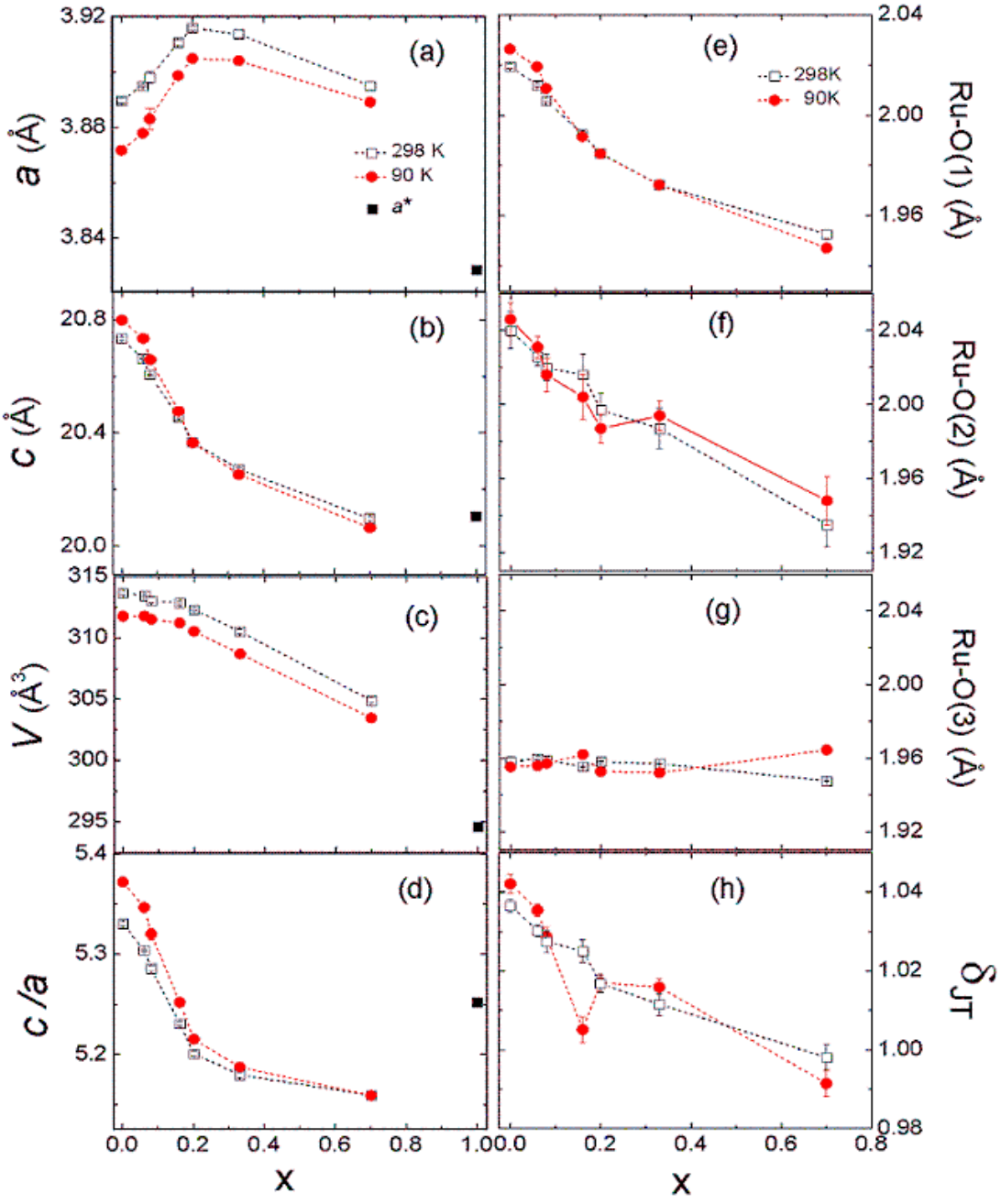

Figure 4.3 The Mn concentration (x) dependence of lattice parameters a, c, unit cell volume V at 298 K (black open squares) and 90 K (red solid circles). The a* (black solid squares) in (a) - (d) represent a, c, V and c/a of polycrystalline $Sr_3Mn_2O_7$, respectively [74]. The refined Ru-O bond lengths at 298 K and 90 K as a function of x: (e) the inner apical, Ru-O(1); (f) the outer apical, Ru-O(2); and (g) the equatorial, Ru-O(3). (h) shows δ_{JT} as a function of x. Dashed lines are guides to eyes.

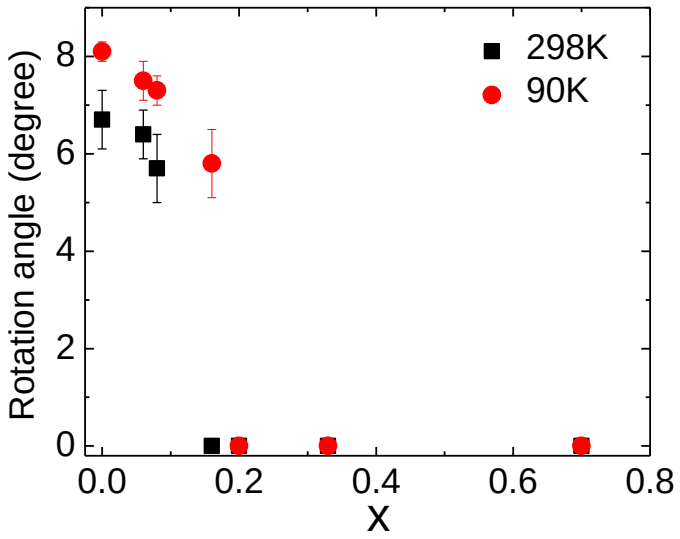

Figure 4.4 Rotation angle of RuO_6 as a function of *x*.

4.3 Surface Structure of $Sr_3Ru_2O_7$ (001)

Breaking the bulk 3-dimensional (3D) symmetry into the 2-dimensional (2D) symmetry causes the surface phase diagram to display different characteristics. Theoretical calculations indicate that the rotation and tilt of RuO_6 octahedra in $Ca_{2-x}Sr_xRuO_4$ are coupled to the ferromagnetism and antiferromagnetism, respectively [63]. Motivated by surface studies on single-layered ruthenate, we are interested in the surface structure of double-layered ruthenate. As mentioned earlier in this chapter, the crystal structure of $Sr_3Ru_2O_7$ can be described in a tetragonal unit cell (*I4/mmm*) with a RuO_6 octahedron rotated about 6.7 ° in bulk at 300K, which is represented by the splitting of the equatorial oxygen occupancy. Although the STM work on $Sr_3Ru_2O_7$ demonstrates the morphology of the surface density of states [99, 100], direct surface structural information is more reliable from quantitative analysis of low-energy electron diffraction (LEED) *I-V* (intensity as a function of voltage). A $Sr_3Ru_2O_7$ single crystal with a size 2.0 x 2.0 x 0.5 mm^3 was cleaved *in situ* under an ultrahigh-vacuum (UHV) chamber with a base pressure of 2×10^{-9} Torr, producing a shiny and flat (001) surface. After cleaving at room temperature, the sample was

immediately transferred into a μ-metal shielded LEED chamber with a base pressure of 7.0×10^{-11} Torr. The sample position was adjusted to reach a normal incidence condition for the primary electron beam. For temperature dependence experiments, we first collected LEED data at 300 K then cooled the sample down. LEED data were collected at 200 K and 80 K. At each setting temperature, the LEED pattern was collected within an energy range of 60 – 600 eV using a home-built video-LEED system. *I-V* curves, which are based on the intensity of the diffraction spots as a function of the energy of the primary electron beam, were generated from digitized diffraction patterns and subsequently normalized to the incident electron beam current, then numerically smoothed with a weighted five-point-averaging method. Considering the controversy on space group in bulk $Sr_3Ru_2O_7$ [39 - 42], the indices of LEED pattern at surface can be based on a tetragonal or orthorhombic basis. But the rotation of octahedral RuO_6 in bulk drives the symmetry into orthorhombic group and makes it more convenient for us to use the orthorhombic basis to describe the surface structure in LEED- *IV* analysis. All *I-V* curves were obtained by averaging symmetrically equivalent beams. Seven [(1,1), (2,0), (2,2), (3,3), (4,0), (4,4) and (3,0)] and ten [(1,1), (2,0), (2,2), (3,3), (4,0), (4,4), (1,2), (1,3), (1,4) and (3,0)] *I-V* curves were collected at 300 K with a total energy range 2056 eV and 80 K with a total energy range 3225 eV, respectively.

Figure 4.5 (a) shows the LEED diffraction pattern of $Sr_3Ru_2O_7$(001) surface at 300 K after a fresh surface cleavage. For a bulk truncated (001) surface, the rotation of the bilayer octahedra will generate glide-lines in the LEED pattern which will produce extinguished diffracted spots. This is illustrated in Figure 4.5 (b), where spots labeled as ($\pm h$, 0) and (0, $\pm h$) (h=1, 3, 5, …) are extinguished at all energies. The dashed lines represent the glide lines. As can be seen in Figure 4.4 (a), one of the glide lines for $Sr_3Ru_2O_7$(001) is absent, and spots such as (3, 0) and (-3, 0) are clearly visible. At subsequent cooling and warming cycle, spots (0, 3) and (0, -3) were always absent, but

spots (3, 0) and (-3, 0) always sustained. Several cleavages from different sample batches reproduced this result. This implies a different symmetry at the surface produced by truncation of the bulk. In a situation very similar to the single layered ruthenates surface [101 - 103], the symmetry consideration indicates that the absence of a glide line is due to a tilt of the top layer octahedra. In bulk $Sr_3Ru_2O_7$, the octahedra are rotated by an angle of ~ 7° at room temperature without any sign of tilt. The surface presents a lower symmetry than bulk. Figure 4.5 (c) schematically presents the rotation and tilt angles of the RuO_6 octahedron at the surface.

The structure determination of the (001) surface of $Sr_3Ru_2O_7$ was performed by employing a quantitative comparison between the experimentally and theoretically generated *I(V)* curves. As mentioned above, the surface has a lower symmetry due to the tilt of top octahedral layer. The surface structure can be described by the plane group, *p2gg* (No. 8). As shown in Figure 4.5 (d) about the configuration of atomic displacements on the surface layer of $Sr_3Ru_2O_7$, calculations for the structure determination was performed with a grid search using the following steps: (1) After setting the top octahedra tilt angle (Θ) at 2^o, the rotation angle (Φ) was optimized (grid search) in the theoretical model in order to minimize R_P (Φ_{MIN}); (2) Using $\Phi=\Phi_{MIN}$, the tilt angle Θ was then optimized (Θ_{MIN}) for minimum R_P; (3) With Θ_{MIN} and Φ_{MIN} fixed, the Sr1 and Sr2 vertical positions [along (001)] were optimized ($Sr1_{BEST}$,$Sr2_{BEST}$); (4) Using Θ_{MIN}, Φ_{MIN}, $Sr1_{BEST}$ and $Sr2_{BEST}$, the motion of O2, Ru and O1 atoms was restricted along O2-Ru-O1 bonding direction and their relative positions were optimized in order to reduce R_P; (5) This procedure was repeated until the R_P reached to a global minimum value. The associated errors in the structural parameters were calculated using the methodology discussed elsewhere [84]. Very good theory-experiment agreement was obtained for both 80 and 300 K data sets, as characterized by the final R_P values of 0.22 and 0.27, respectively.

Figure 4.6 (a) and (b) shows typical theoretical and experimental *I(V)* curves for comparison at 300 K and 80 K, respectively.

Our structural results for the top layer octahedra, presented in Table 4.9, clearly indicate a more distorted structure in the surface than in the bulk. The top layer octahedra present a tilt of (4.5 ± 2.5 °) at 300 K and (2.5 ± 1.7) ° at 80 K, which was not observed from 298 to 90 K in the case of bulk. Within the relative uncertainties, the surface octahedral rotation angle (~ 12 °) does not statistically change within the temperature range between 80 and 300 K. This is contrary and larger than the rotation that occurs in the bulk which has an increase in rotation angle as the temperature decreases (*I*.e. 6.7(6) ° at 298 K to 8.1(2) ° at 90 K). The surface structure is quite distinct from the bulk. It is more distorted with the top RuO_6 octahedron not only rotated with higher angle than the bulk (~ 12°), but also tilted (~ 4°). This tilting structural phase was not observed for bulk at any temperature between 90 and 298 K. The surface rotation angle remains constant with temperature, while the tilting angle slightly decreases as decreasing temperature. This lower tilting angle suggests a more stable structure at lower temperatures. The surface octahedral tilting can lead the surface to present different physical properties, since lattice distortions are strongly coupled with the orbital and spin degrees of freedom in this material. This surface structural change can play a key role in the competition between antiferromagnetic and ferromagnetic interactions. Single-crystal XRD refinements have revealed a RuO_6 rotation in bulk Mn-doped $Sr_3Ru_2O_7$ compounds for crystal $x \leq 0.2$, where the rotation angle monotonically decreases with increasing x. The surface structures of doped compounds are expected to display different features from bulk. The tilt of RuO_6 that emerges in the surface $Sr_3Ru_2O_7(001)$ may eventually disappear in doped one, which need a further study in the future.

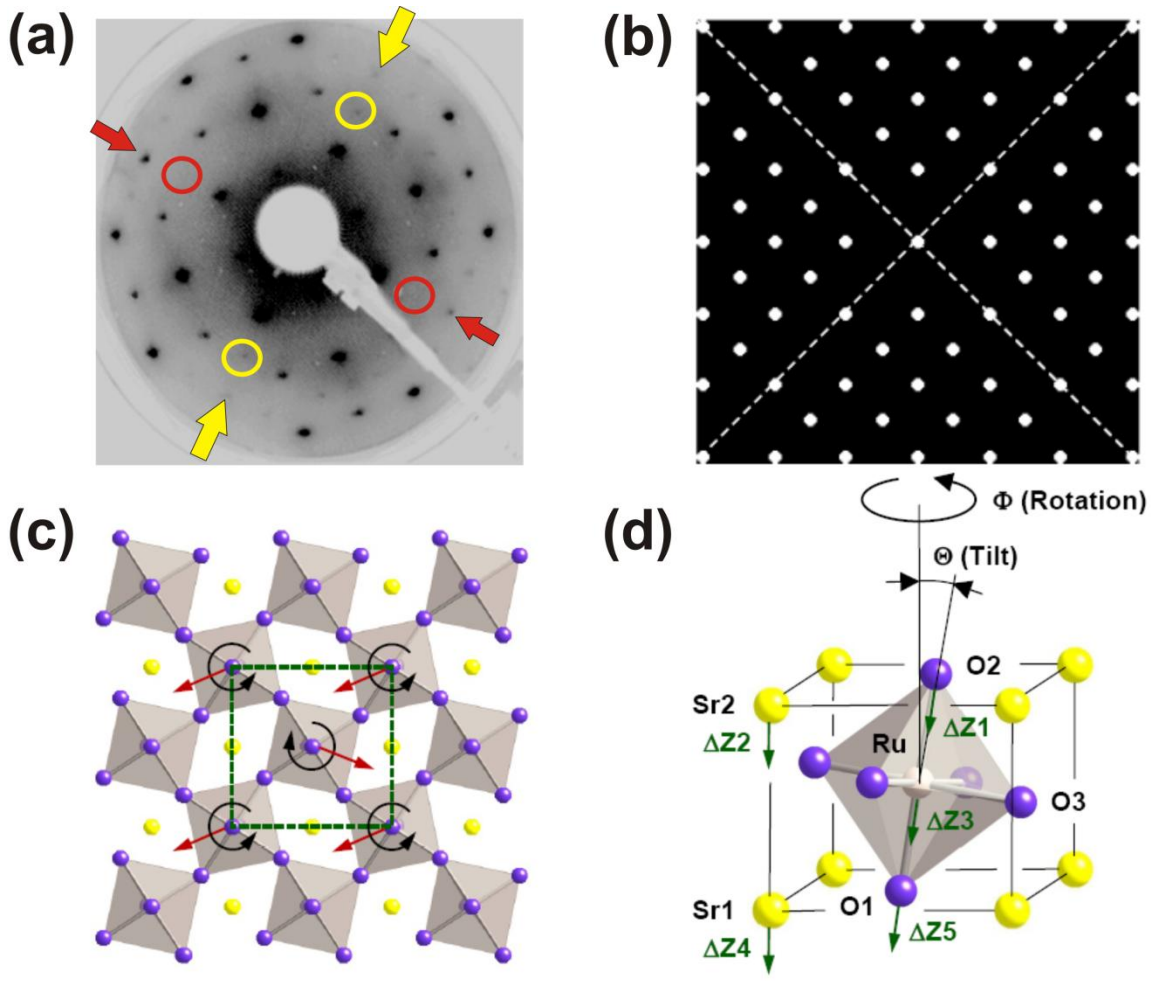

Figure 4.5 (a) LEED diffraction pattern with energy of 225eV at 300K. The red arrows indicate the only existing glide line. The two red circles show the locations of the two extinguished spots [(0, 3) and (0, -3)] along this line. Yellow arrows point the broken glide line, where (3, 0) and (-3, 0) diffracted spots are visible as indicated by the yellow circles. (b) Schematic diffraction pattern for a *p2gg* symmetry with the two glide lines. (c) Top view of the (001) surface of $Sr_3Ru_2O_7$, black and red arrows represent the rotation and tilting of the octahedral, respectively; (d) Schematic illustration of the (001) surface of $Sr_3Ru_2O_7$.

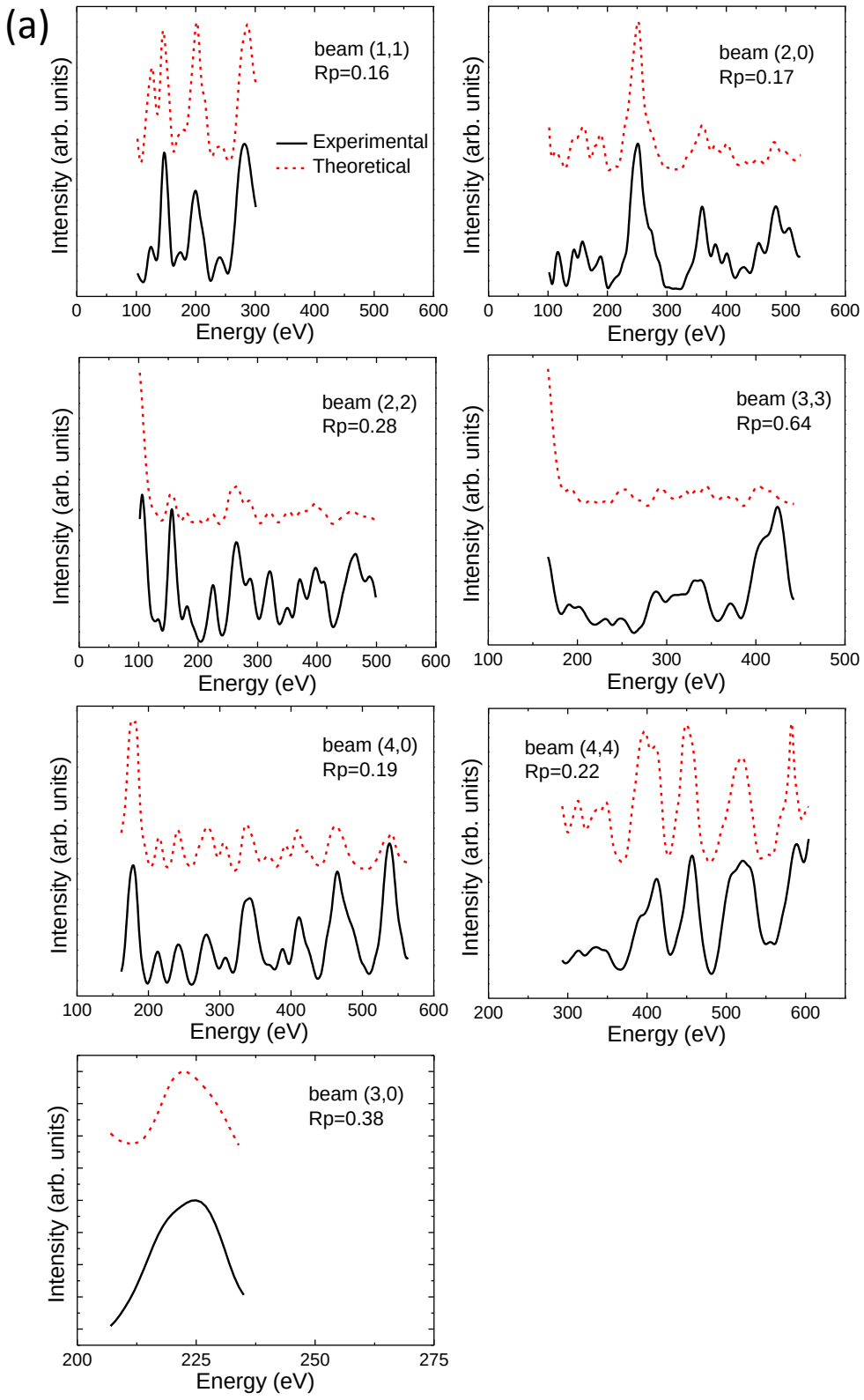

Figure 4.6 Comparison between typical experimental and theoretically generated *I(V)* curves for the final structure obtained for the $Sr_3Ru_2O_7$(001) surface at a temperature of 300 K (a) and 80 K (b).

fig. cont'd

(b)

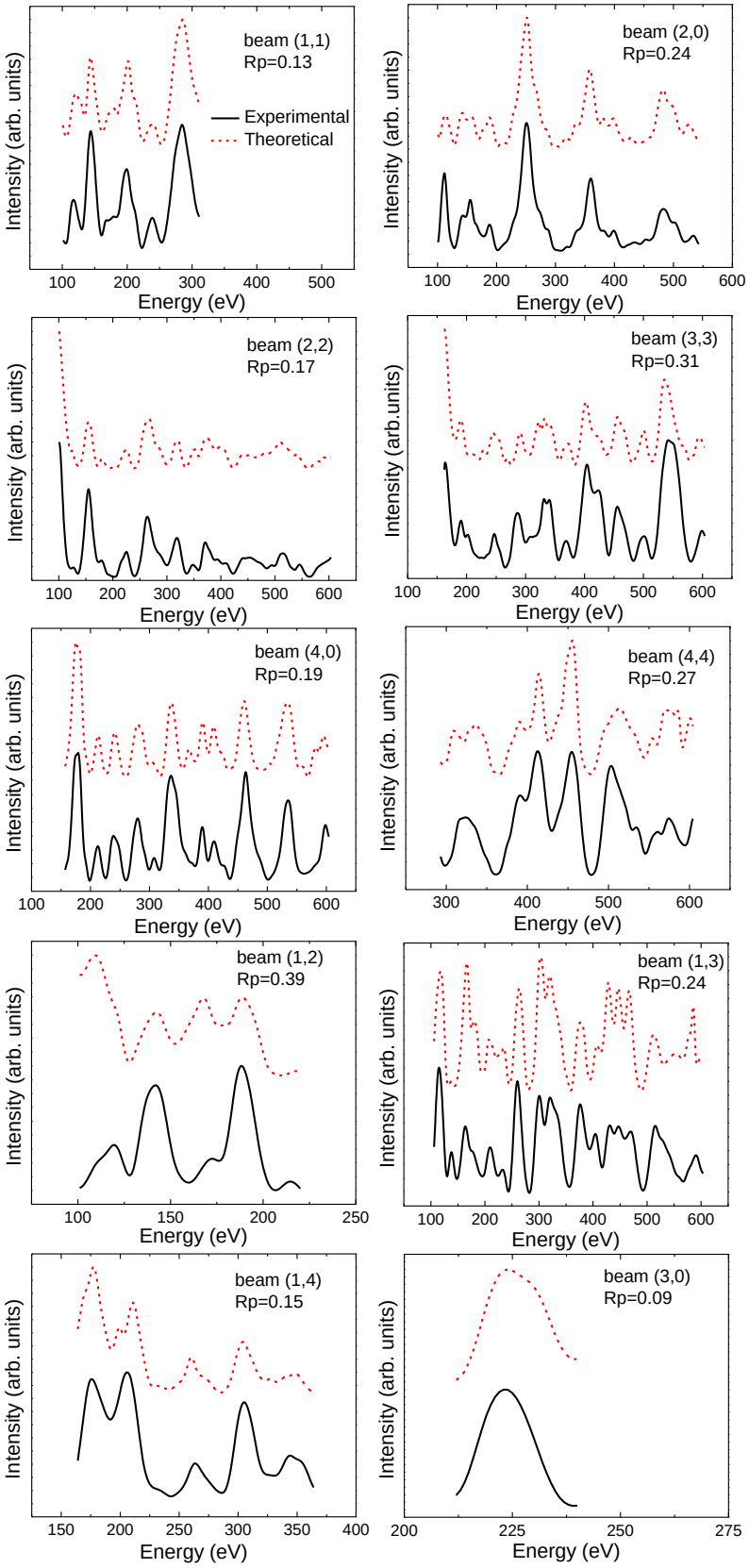
beam (1,1)
Rp=0.13
Experimental
Theoretical
beam (2,0)
Rp=0.24
beam (2,2)
Rp=0.17
beam (3,3)
Rp=0.31
beam (4,0)
Rp=0.19
beam (4,4)
Rp=0.27
beam (1,2)
Rp=0.39
beam (1,3)
Rp=0.24
beam (1,4)
Rp=0.15
beam (3,0)
Rp=0.09
Intensity (arb. units)
Energy (eV)

Table 4.9 Final Structure of $Sr_3Ru_2O_7$(001) Surface at Temperatures of 300 and 80 K. The displacements of the atoms in the surface layer with respect to a bulk truncated structure as determined by our *x*-ray measurements. Bulk values for the octahedra rotation and tilt angles as well as for the Ru-O distances are also presented for comparison.

Parameter	300 K	80 K
$\Delta Z1$ (O(2))	(0.040 ±0.060) Å	(0.060 ± 0.040) Å
$\Delta Z2$ (Sr top)	(0.020 ±0.020) Å	(0.050 ± 0.015) Å
$\Delta Z3$ (Ru)	(-0.010 ±0.020) Å	(0.025 ± 0.020) Å
$\Delta Z5$ (O(1))	(-0.020 ±0.080) Å	(0.015 ± 0.040) Å
$\Delta Z4$ (Sr middle)	(0.020 ±0.030) Å	(0.045 ± 0.015) Å
Ru-O(2)	(1.990 ± 0.040) Å	(2.011 ± 0.030) Å
	Bulk: 2.0400 Å	Bulk: 2.0460 Å
Ru-O(3)	(1.988 ± 0.035) Å	(1.979 ± 0.025) Å
	Bulk: 1.9580 Å	Bulk: 1.9553 Å
Ru-O(1)	(2.009 ± 0.050) Å	(2.016 ± 0.030) Å
	Bulk: 2.0195 Å	Bulk: 2.0263 Å
RuO_6 rotation	(12 ± 5) °	(12 ± 3) °
	Bulk: 6.7 °	Bulk: 8.0 °
RuO_6 tilt	(4.5 ± 2.5) °	(2.5 ± 1.7) °
	Bulk: 0.0 °	Bulk: 0.0 °
Rp	(0.27 ± 0.03)	(0.22 ± 0.02)

Chapter 5 Physical Properties of $Sr_3(Ru_{1-x}Mn_x)_2O_7$ ($0 \leq x \leq 0.7$)

5.1 Physical Properties of $Sr_3(Ru_{1-x}Mn_x)_2O_7$ (x = 0 and 0.06)

The measurement on the temperature dependence of in-plane resistivity ρ_{ab} (I//ab) reveals a metallic-to-insulating crossover in Mn doped samples. As shown in Figure 5.1 (a), ρ_{ab} (T) remains metallic ($d\rho/dT > 0$) in the whole temperature range in undoped compound (x = 0) while $\rho_{ab}(T)$ shows an insulating ($d\rho/dT < 0$) behavior below a certain temperature in x = 0.06 compound. Here we define a metallic-to-insulating crossover temperature (T_{MIT}) where $d\rho/dT = 0$. As displayed in Figure 5.1 (b), ρ_{ab} (T) shows a minimum at T_{MIT} = 18 K for x = 0.06. The insulating behavior in ρ_{ab} (T) at low temperature is suppressed by the applied magnetic field (H//c), as shown in Figure 5.1 (c). A phase diagram of T_{MIT} as a function of applied magnetic field (H) is shown in Figure 5.1 (d), where the insulating region separates from the metallic region. A field with 6 T drives the system into a fully metallic state. Figure 5.2 shows the in-plane transverse magnetoresistance (MR; $H \perp I$, $\Delta\rho_{ab}^{\perp} / \rho_{ab} \equiv (\rho_{ab}(H) - \rho_{ab}(0))/\rho_{ab}(0))$ at different temperatures for x = 0.06. At low temperature, $\Delta\rho_{ab}^{\perp} / \rho_{ab}$ shows negative value and the absolute value of $\Delta\rho_{ab}^{\perp} / \rho_{ab}$ increases with decreasing temperature. $\Delta\rho_{ab}^{\perp} / \rho_{ab}$ achieves a value over –70% in high fields (> 8 T) at 5 K for both H//ab and H//c. The absolute value of $\Delta\rho_{ab}^{\perp} / \rho_{ab}$ for H//ab at each temperature is slightly larger than that of $\Delta\rho_{ab}^{\perp} / \rho_{ab}$ for H//c.

The temperature dependence of out-of-plane resistivity ρ_c (I//c) also shows a metallic-to-insulating crossover with Mn doping. As shown in Figure 5.3 (a), $\rho_c(T)$ remains metallic in the whole temperature range in undoped sample while $\rho_c(T)$ shows an insulating upturn below T^c_{MIT} (= 20 K) for x = 0.06. The upturn in $\rho_c(T)$ at low temperatures is gradually suppressed by the application of magnetic field (H//c), as shown in Figure 5.3 (b). Figure 5.3 (c) shows out-of-plane

longitudinal MR $\Delta\rho_c^{//}/\rho_c$ (H//I; $\Delta\rho_c^{//}/\rho_c \equiv (\rho_c(H) - \rho_c(0))/\rho_c(0)$) at different temperatures for x = 0.06 in field H//c. The absolute value of $\Delta\rho_c^{//}/\rho_c$ increases with decreasing temperature.

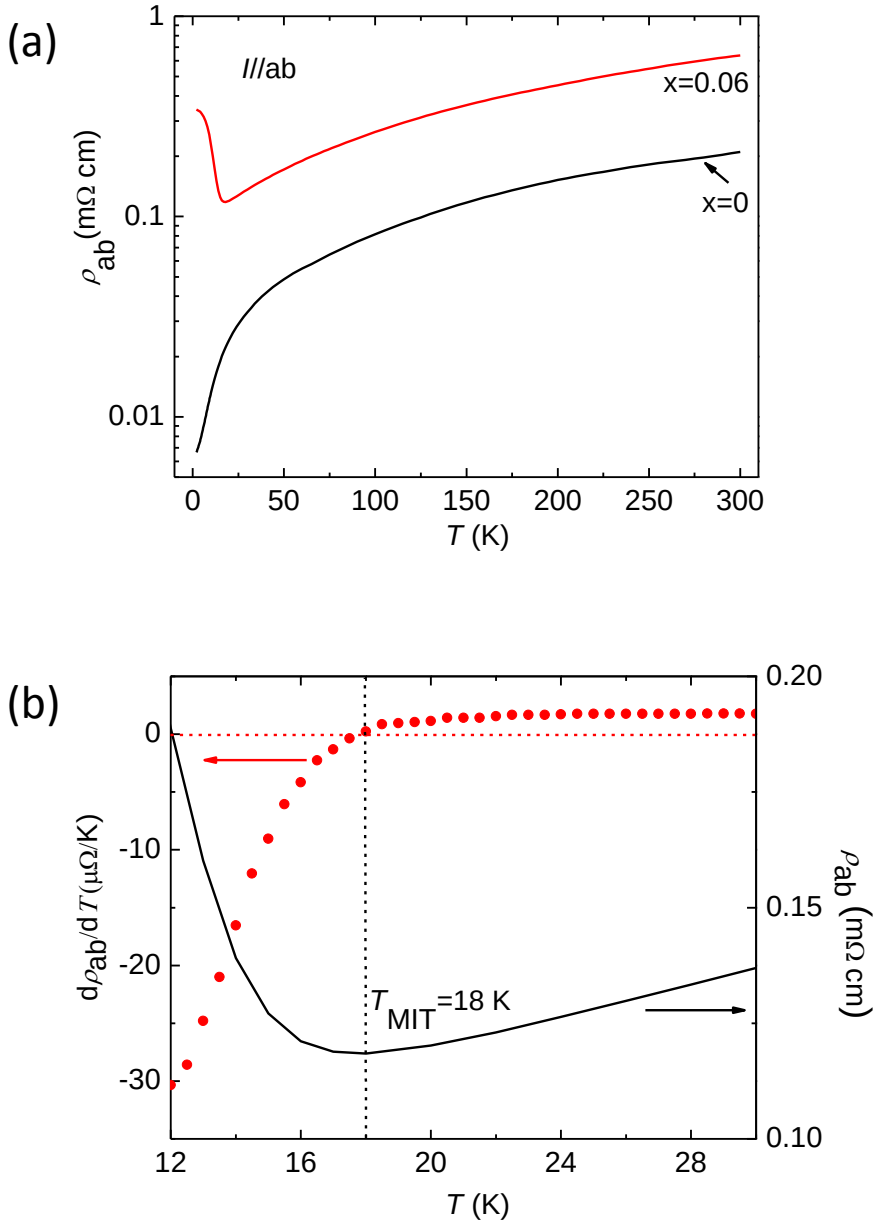

Figure 5.1 (a) Temperature dependences of $\rho_{ab}(T)$ for x = 0 and x = 0.06 under zero field. (b) The derivative of resistivity $d\rho_{ab}(T)/dT$ as a function of T (left axis) and $\rho_{ab}(T)$ as a function of T (right axis). Red dashed line is the guide to eyes. Black dashed line indicates the minimum of ρ_{ab}(T) at T_{MIT} (= 18 K) for x = 0.06. (c) Temperature dependences of $\rho_{ab}(T)$ at low temperatures under different fields (H//c). (d) T_{MIT} as a function of applied magnetic field (H).

fig. cont'd

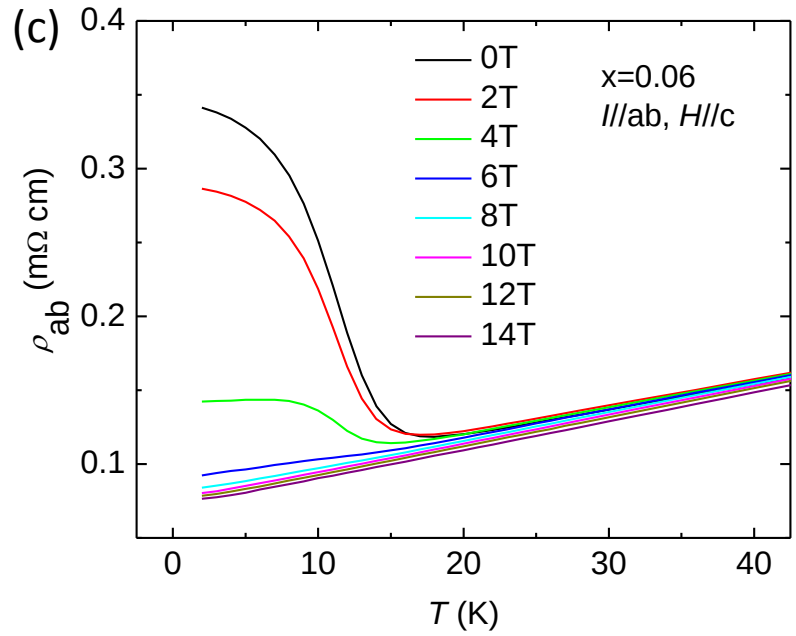
(c)
0.4
0.3
0.2
0.1
ρ_{ab} (mΩ cm)
0T
2T
4T
6T
8T
10T
12T
14T
x=0.06
I//ab, H//c
0
10
20
30
40
T (K)

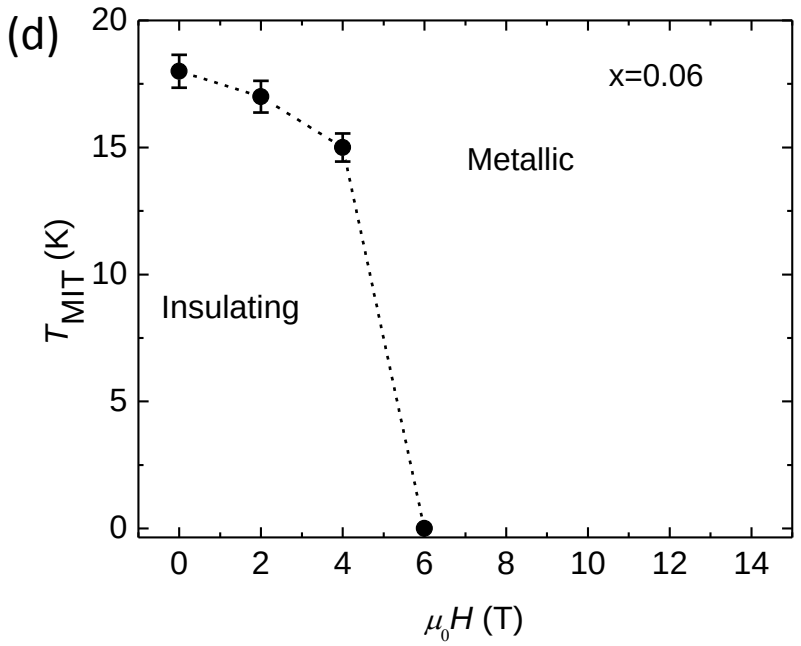
(d)
20
15
10
5
0
T_{MIT} (K)
x=0.06
Metallic
Insulating
0
2
4
6
8
10
12
14
$\mu_0 H$ (T)

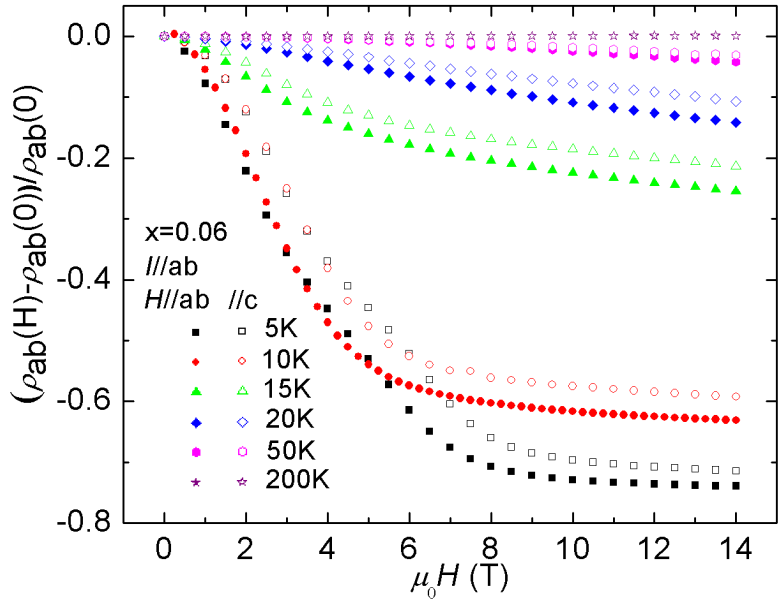

Figure 5.2 In-plane transverse MR $\Delta\rho_{ab}^{\perp} / \rho_{ab}$ in H//c configuration (I//ab, $H \perp I$; open symbols) and H//ab configuration (I//ab, $H \perp I$; solid symbols) for x = 0.06 at different temperatures.

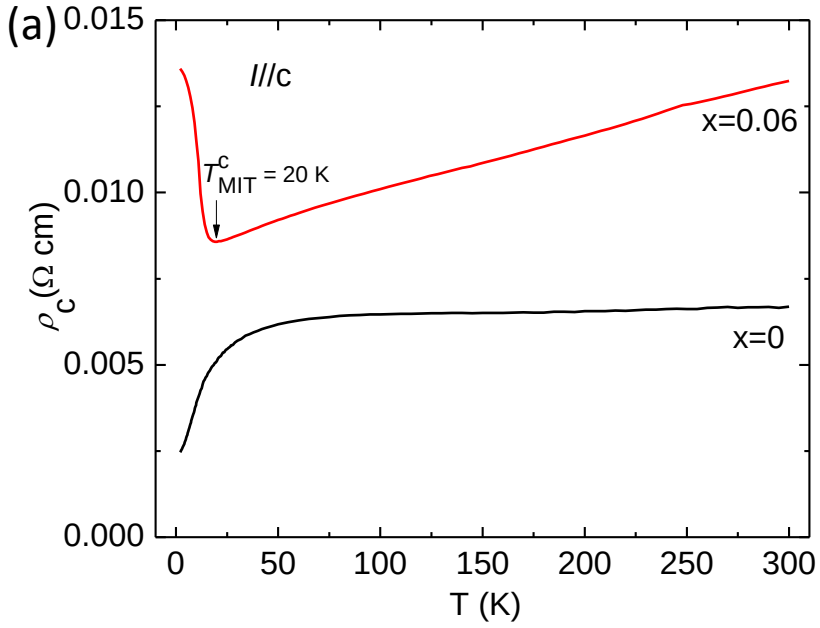

Figure 5.3 (a) Temperature dependences of $\rho_c(T)$ for x = 0 and x = 0.06 under zero field. The arrow indicates the minimum of ρ_c at T^{c}_{MIT} (= 20 K) for x = 0.06. (b) Temperature dependences of $\rho_c(T)$ at low temperatures under different fields (H//c). (c) Out-of-plane longitudinal MR $\Delta\rho_c^{//} / \rho_c$ (H//I, I//c) for x = 0.06 at different temperatures in field H//c.

fig. cont'd

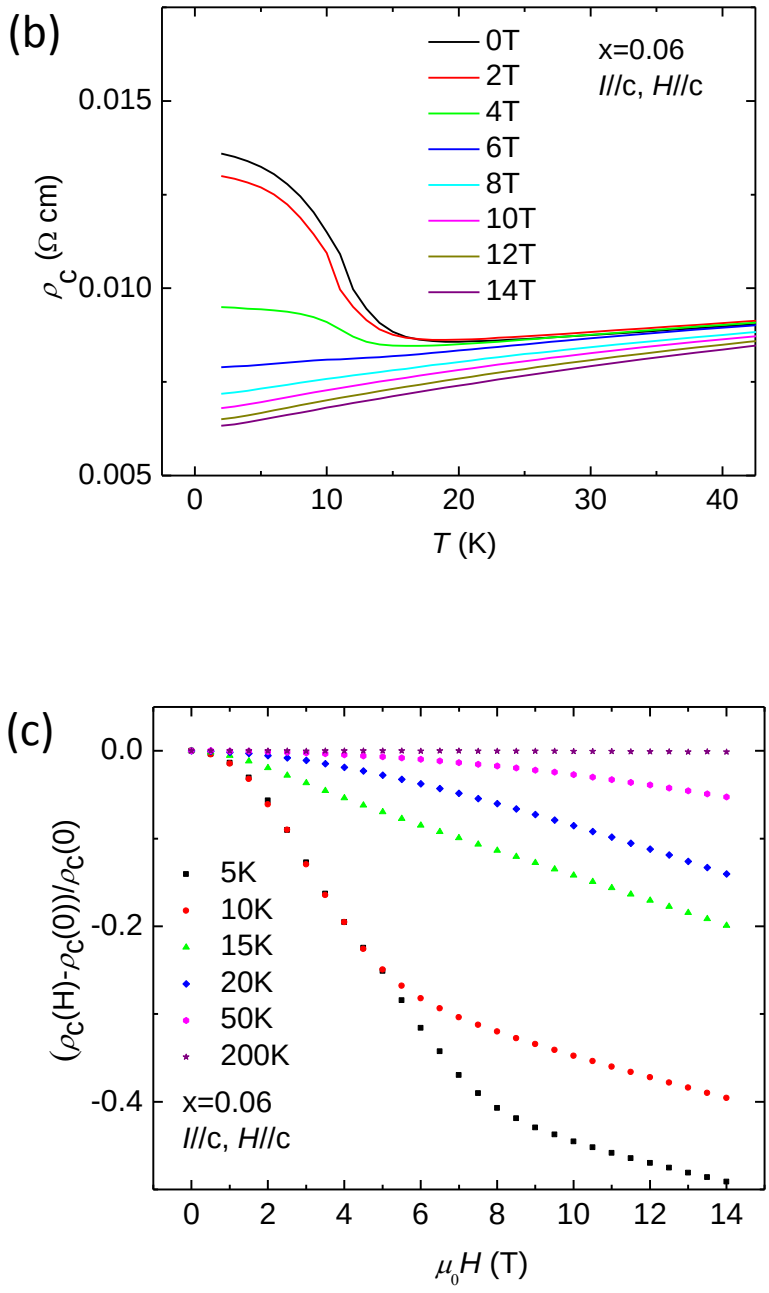

Figure 5.4 (a) shows the magnetic susceptibility $\chi = M/H$ as a function of T in a field of 1 T. The susceptibilities for both χ_{ab} (H//ab) and χ_c (H//c) exhibit a pronounced peak at 15 K for x = 0.06. Here we define a characteristic temperature T_M at the peak position, as shown in the inset of Figure 5.4 (a). Inverse susceptibility $1/\chi$ as a function of T, shown in Figure 5.4 (b), revealed a good linear

behavior at high temperature. We use Curie-Weiss law $\chi(T) = \chi_0 + \chi_{CW}(T)$ to fit magnetic susceptibility data between 175 K and 390 K. Here, χ_0 is the temperature independent term and $\chi_{CW}(T) = C/(T-\Theta_{CW})$ is the Curie-Weiss term with Curie constant $C = N_A p_{eff}^2 \mu_B^2 /(3k_B)$ and Weiss temperature Θ_{CW}, where N_A is the Avogadro number, p_{eff} is the effective Bohr magneton number per Ru, μ_B is the Bohr magneton and k_B is the Boltzmann constant. The green lines in Figure 5.4 (a) and (b) represent the fitting results for χ_{ab} under ZFC condition. The χ_c under ZFC condition was also fitted well by Curie-Weiss law in the same temperature range. The obtained p_{eff} and Θ_{CW} from the fitting for x = 0.06 are p_{eff}^{ab} = 3.14 (p_{eff}^{c} =2.88) and Θ_{CW}^{ab} = -31 K (Θ_{CW}^{c} = -19 K) for H//ab (H//c). The magnetization (M) versus applied field (H) measurement at 2 K shows a tiny hysteresis for both field directions H//ab and H//c, as shown in Figure 5.5. The green line in Figure 5.5 represents M vs H curve at 2 K in H//ab for x = 0, where the behavior of metamagnetism is observed around 5 T.

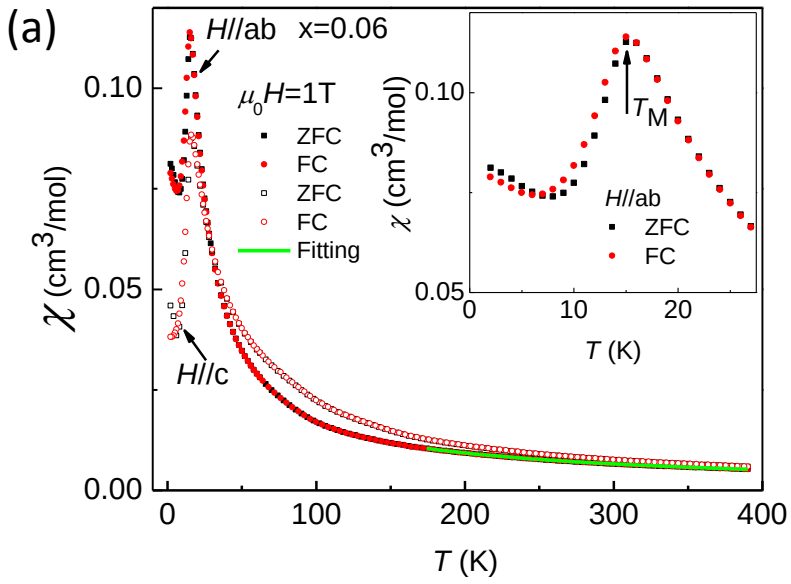

Figure 5.4 (a) Temperature dependences of magnetic susceptibility for in-plane (H//ab) and out-of-plane (H//c) under 1 T field for x = 0.06. The inset shows the defined characteristic temperature T_M at peak position. (b) Inverse susceptibility $1/\chi$ vs T. Solid line (green) is Curie-Weiss law fitting at high temperature range. Squares indicate ZFC condition while diamonds indicate FC condition. Solid symbols represent H//ab while open symbols represent H//c.

fig. cont'd

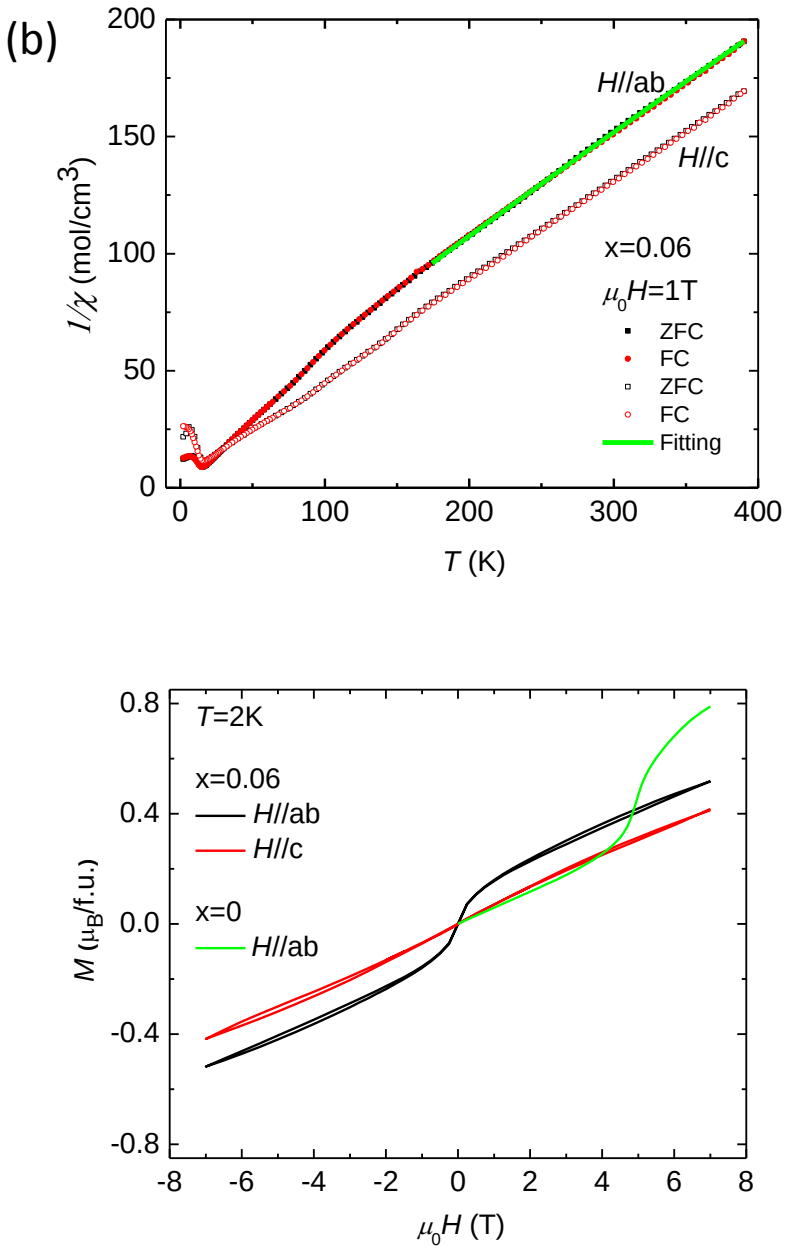

Figure 5.5 Magnetization (M) versus field (H) loops at 2 K for H//ab (black line) and H//c (red line) in crystal with x = 0.06. Green line is M vs H curve of undoped compound at 2 K for H//ab.

The measurement on the temperature dependence of the specific heat (plotted as $C_p(T)/T$ versus T) for x = 0.06 reveals a specific heat anomaly around T_M (15 K), as shown in Figure 5.6 (a). Remarkably, the anomaly is suppressed by the applied magnetic field of 6 and 14 T. The magnetic

susceptibility measurement shows an AFM ordering below T_M. The derived p_{eff} from Curie-Weiss law fitting in $x = 0.06$ is $p_{eff}^{ab} = 3.14$ ($p_{eff}^{c} = 2.88$), yielding $S = 1.15$ (1.03) for H//ab (H//c), where S is derived from $p_{eff} = g\sqrt{S(S+1)}$ with $g = 2$ assuming that the orbital angular momentum is quenched. In $x = 0.06$, the total spin is close to $S = 1$ for Ru^{4+}. In this case, the magnetic entropy removed upon ordering is expected to be $S_M = R \ln(2S+1) = 1.16\ R$ ($R = 8.31$ J/mol K). By integrating the data (zero field) of crystal with $x = 0.06$ after subtraction of a certain base line, the entropy change associated with the transition $\Delta S \sim 0.04 \pm 0.01\ R$ is estimated, which is much smaller than the expected $S_M = 1.16\ R$. This suggests partial entropy above T_M and some spins remain unordered. For the comparison, we also plot specific heat data of $Sr_3Ru_2O_7$ ($x = 0$) (blue line). Figure 5.6 (b) shows plots of C_p/T vs T^2 in zero field for $x = 0$ (black line) and 0.06 (red line). No specific heat anomaly is observed around the characteristic temperature T_M (= 16 K) in $Sr_3Ru_2O_7$. The T^2 dependence of C_p/T does not follow a linear behavior below 15 K, which is contributed by spin fluctuations at the ground state of $Sr_3Ru_2O_7$ [38]. However, the specific heat anomaly is observed around magnetic ordering temperature T_M (= 15 K) in crystal with $x = 0.06$, which indicated a true phase transition at T_M. Both χ_{ab} and χ_c show a maximum at T_M and an upturn at low temperature, suggesting the developing of AFM ordering below T_M. The derived Θ_{CW} from Curie-Weiss law fitting is negative for both H//ab and H//c, which further confirms the AFM feature for $x = 0.06$. Nevertheless, the observation of field dependence of metallic-to-insulating crossover reveals the competition of metallic and insulating phases in crystal with $x = 0.06$, where an electronic phase separation forms at low temperature.

Both Hall coefficients R_H of crystals with $x = 0$ and 0.06 show positive sign in the measured temperature range, as shown in Figure 5.7 (a). The positive sign of R_H suggests that the dominated charge carriers in these two systems are holes. We observed a pronounced peak in R_H around 25 K in crystal with $x = 0$, which agrees well with previous reports [104, 105]. The Hall resistivity ρ_H as a

function of H in crystals with x = 0 and 0.06 is shown in Figure 5.7 (b) and (c), respectively. ρ_H varies linearly with H up to 4 T in crystal with x = 0 at all measured temperatures while the linear behavior in ρ_H versus H up to 4 T develops only above 20 K in crystal with x = 0.06.

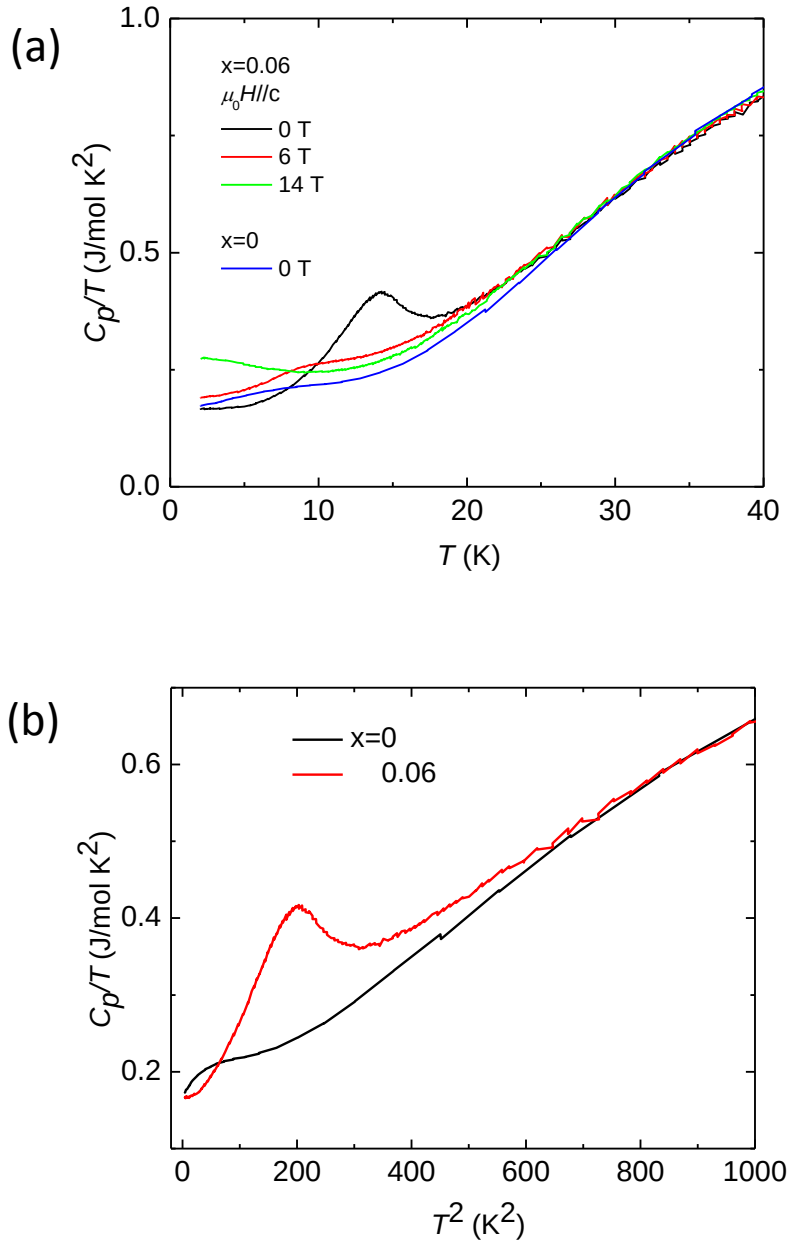

Figure 5.6 (a) Measured specific heat (C_p/T) as a function of T under magnetic field 0 T (black line), 6 T (red line) and 14 T (green line). The blue line represents the specific heat (C_p/T) of x = 0 as a function of T under zero field. (b) Plot of C_p/T vs T^2 in zero field for x = 0 (black line) and 0.06 (red line).

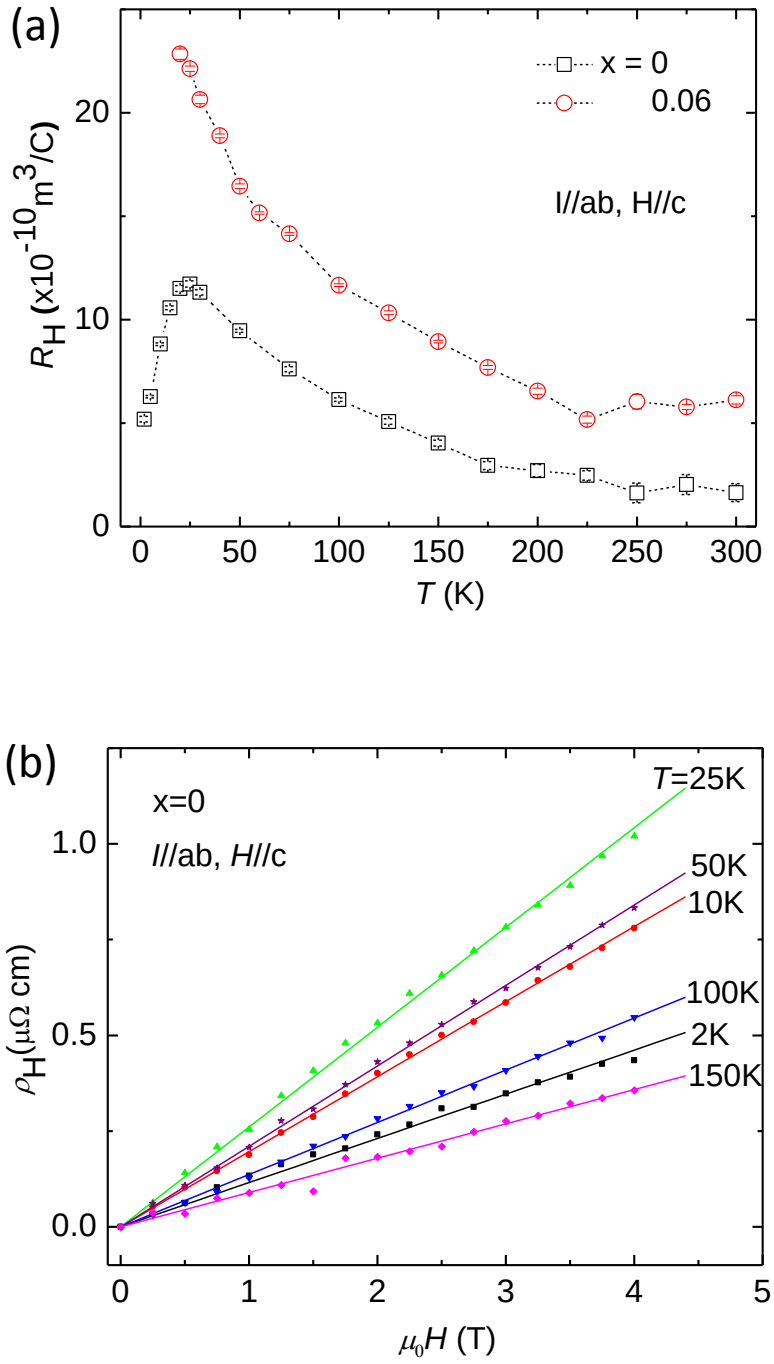

Figure 5.7 (a) Temperature dependence of Hall coefficient R_H for x = 0 (black open squares) and 0.06 (red open circles). Magnetic field dependence of ρ_H at selected temperatures for x = 0 (b) and 0.06 (c). The plot of ρ_H versus H is within 4 T for both samples.

fig. cont'd

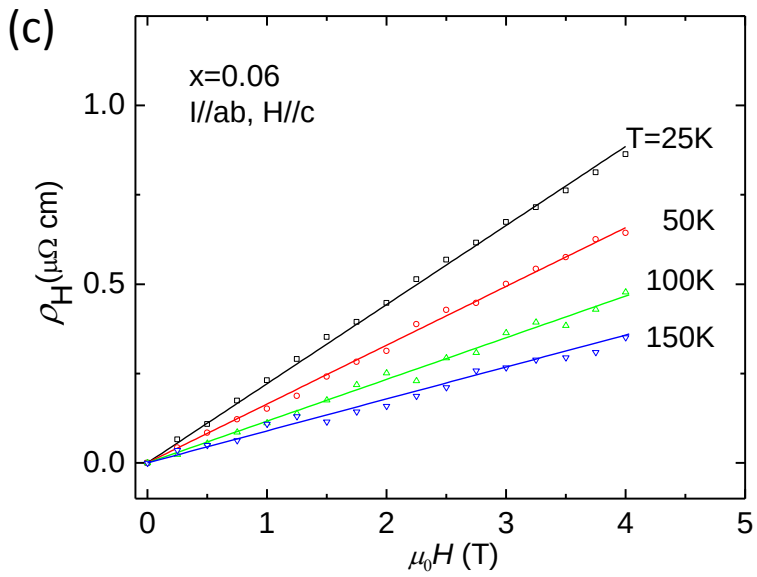

5.2 Physical Properties of $Sr_3(Ru_{1-x}Mn_x)_2O_7$ (x = 0.08)

A field dependence of metal-to-insulating crossover was observed in crystal with x = 0.08, as shown in Figure 5.8 (a). T_{MIT} is about 62.5 K under zero field (inset of Figure 5.8 (a)). The application of magnetic field suppresses the upturn in resistivity (Figure 5.8 (b)) and shifts T_{MIT} to a lower temperature, suggesting an AFM feature of the insulating state below T_{MIT}. As shown in Figure 5.8 (c), T_{MIT} decreases with increasing field, which can be understand from a scenario of electronic phase separation. The in-plane transverse MR $\Delta\rho_{ab}^{\perp} / \rho_{ab}$ (I//ab, H//c) of crystal with x = 0.08 at some selected temperatures are shown in Figure 5.9. $\Delta\rho_{ab}^{\perp} / \rho_{ab}$ is negative below T_{MIT} (e.g. black line (50K)) and positive at high temperatures (e.g. purple line (300K)).

Figure 5.10 (a) displays the temperature dependence of ρ_c (I//c) under zero field in crystal with x = 0.08. ρ_c shows a slope sign change at T^c_{MIT} (= 68 K) under zero field (Inset of Figure 5.10

(a)). The *c*-axis longitudinal MRs $\Delta\rho_c^{//}/\rho_c$ (*I*//c, *H*//c) of crystal with x = 0.08 at selected temperatures are shown in Figure 5.10 (b). $\Delta\rho_c^{//}/\rho_c$ is negative below T^c_{MIT} (*e.g.* 50 K (black line))

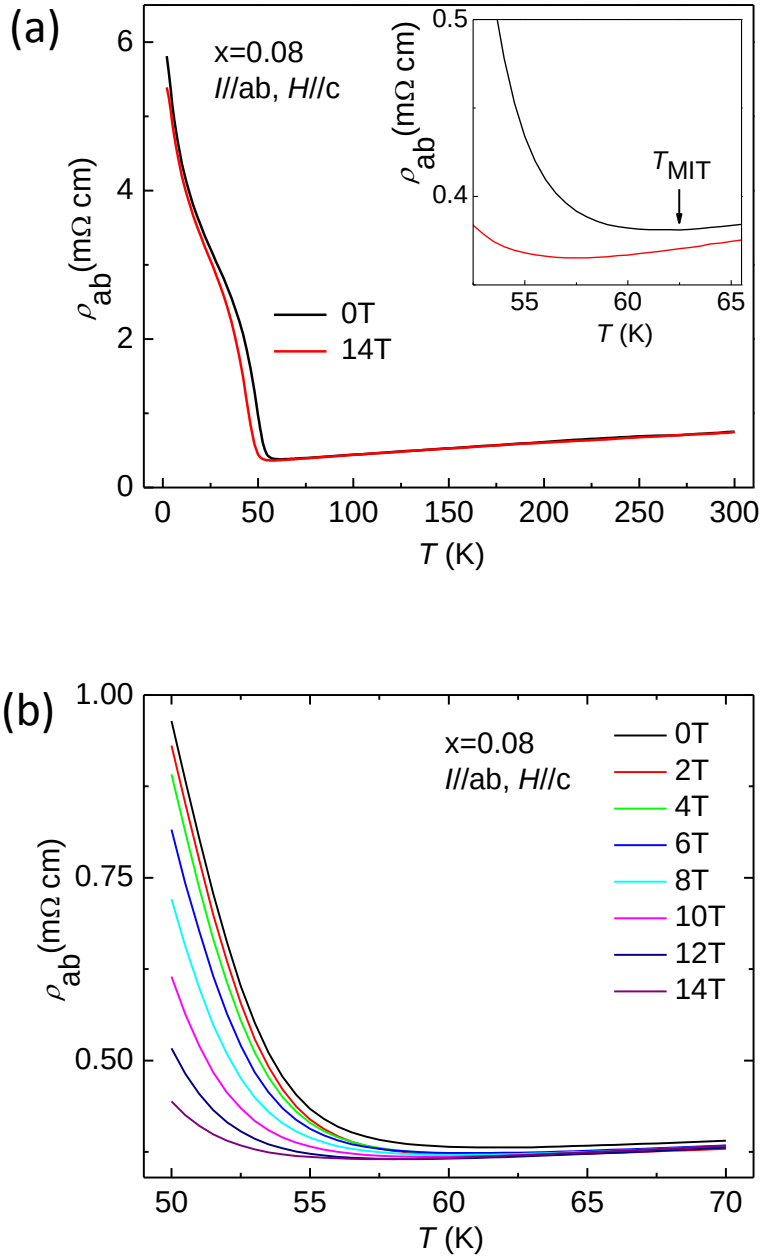

Figure 5.8 (a) Temperature dependences of ρ_{ab} (T) for x = 0.08 under 0 T and 14 T. The applied magnetic field is parallel to *c*-axis. The inset of (a) shows the T_{MIT} for x = 0.08. (b) Temperature dependence of ρ_{ab} in different magnetic field. (c) Field dependence of T_{MIT} for x = 0.08. Dashed line is the guide to eyes.

fig. cont'd

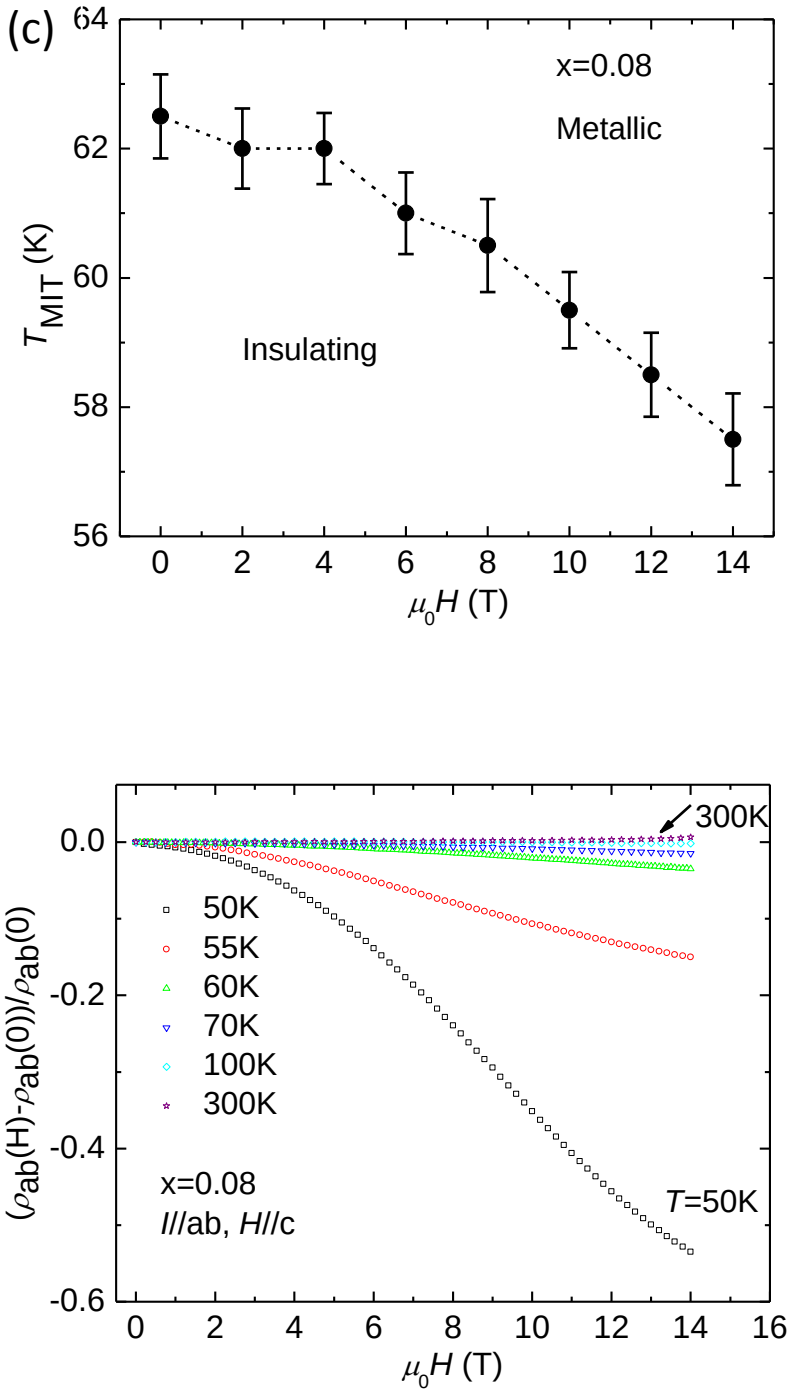

Figure 5.9 In-plane transverse MR $\Delta\rho_{ab}^{\perp}/\rho_{ab}$ (I//ab, $H \perp I$) of crystal with x = 0.08 at selected temperatures for field H//c.

and positive at high temperatures (*e.g.* 300K (purple stars)), which is similar to in-plane transverse MR $\Delta\rho_{ab}^{\perp} / \rho_{ab}$.

Both magnetic susceptibilities χ_{ab} and χ_c show a peak at temperature T_M around 58 K for x = 0.08, as shown in Figure 5.11 (a). A magnetic field of 1 kOe is applied parallel to *ab*-plane or *c*-axis. Inverse susceptibility $1/\chi$ (Figure 5.11 (b)) displays a good linear behavior above 175 K. Both χ_{ab} (T) and χ_c (T) is fitted with the formula $\chi(T) = \chi_0 + \chi_{CW}(T)$ between 175 K and 390 K. The obtained p_{eff} and Θ_{CW} from the fitting for crystal x = 0.08 are p_{eff}^{ab} = 3.04 (p_{eff}^{c} =3.49) and Θ_{CW}^{ab} = -13 K (Θ_{CW}^{c} = -25 K) for H//ab (H//c). The negative values of Θ_{CW} suggest AFM interactions at high temperatures. As shown in Figure 5.12, magnetization (M) versus field (H) measurement at 2 K shows a straight line for H//c while a slight deviation from linearity is discernible for H//ab.

Figure 5.13 (a) shows the temperature dependence of the specific heat (plotted as $C_p(T)/T$ versus T) for sample x = 0.08 between 2 K and 100 K under H = 0 T and 14 T (H//c). Note that the specific heat exhibits an anomaly around T_M (58 K). Remarkably, the anomaly is suppressed by the applied magnetic field of 14 T. The derived p_{eff} from Curie-Weiss law fitting in x = 0.08 yields S = 1.10 (1.31) for H//ab (H//c). The expected magnetic entropy removed upon ordering is between S_M = 1.16 R and 1.28 R. In order to estimate the quantitative magnetic entropy removal near T_M, we fit the experimental data (zero field) at $20 \leq T \leq 30$ K and $70 \leq T \leq 100$ K using a polynomial (Dashed green line in Figure 5.13 (a)). After subtracting the background from the polynomial fitting, we obtain the entropy change associated with the transition $\Delta S \sim 0.64 \pm 0.05$ R, which is much smaller than the expected S_M. This suggests partial entropy above T_M and some spins remain unordered. Figure 5.13 (b) shows plots of C_p/T vs T^2 in zero field for x = 0.08. The T^2 dependence of C_p/T shows a non-linear behavior at low temperatures, which attributes to the magnetic ordering in crystal with x = 0.08.

The temperature dependence of the Hall coefficient R_H in crystal with x = 0.08 is shown in Figure 5.14 (a), where R_H is positive over the entire measured temperature range (2 - 300 K). The Hall resistivity ρ_H as a function of H at different temperatures is shown in Figure 5.14 (b). Hall resistivity ρ_H varies linearly with H up to 7 T over the measured temperature range.

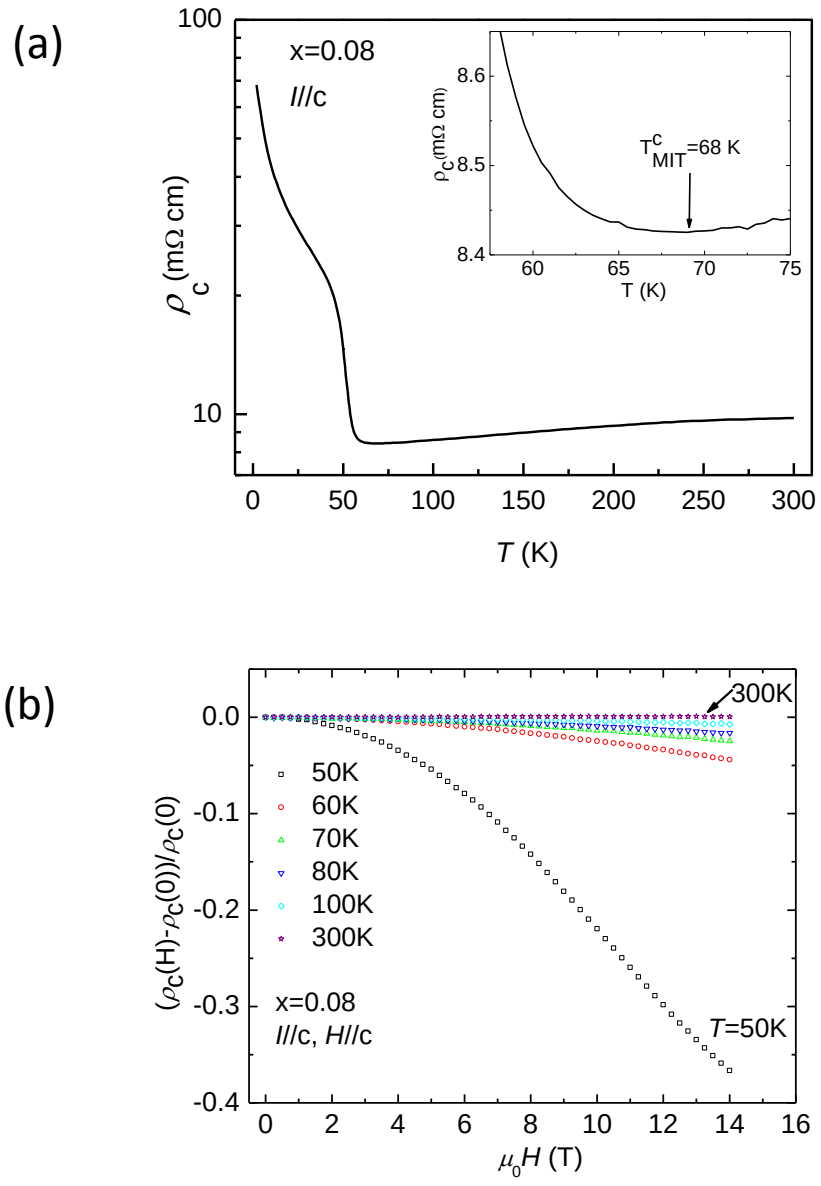

Figure 5.10 (a) Temperature dependences of $\rho_c(T)$ for x = 0.08 under zero field. The inset of (a) shows the T^c_{MIT} of ρ_c for x = 0.08 under zero field. (b) The c-axis longitudinal MR $\Delta\rho_c^{//} / \rho_c$ (I//c, H//I) of crystal with x = 0.08 at selected temperatures in field H//c.

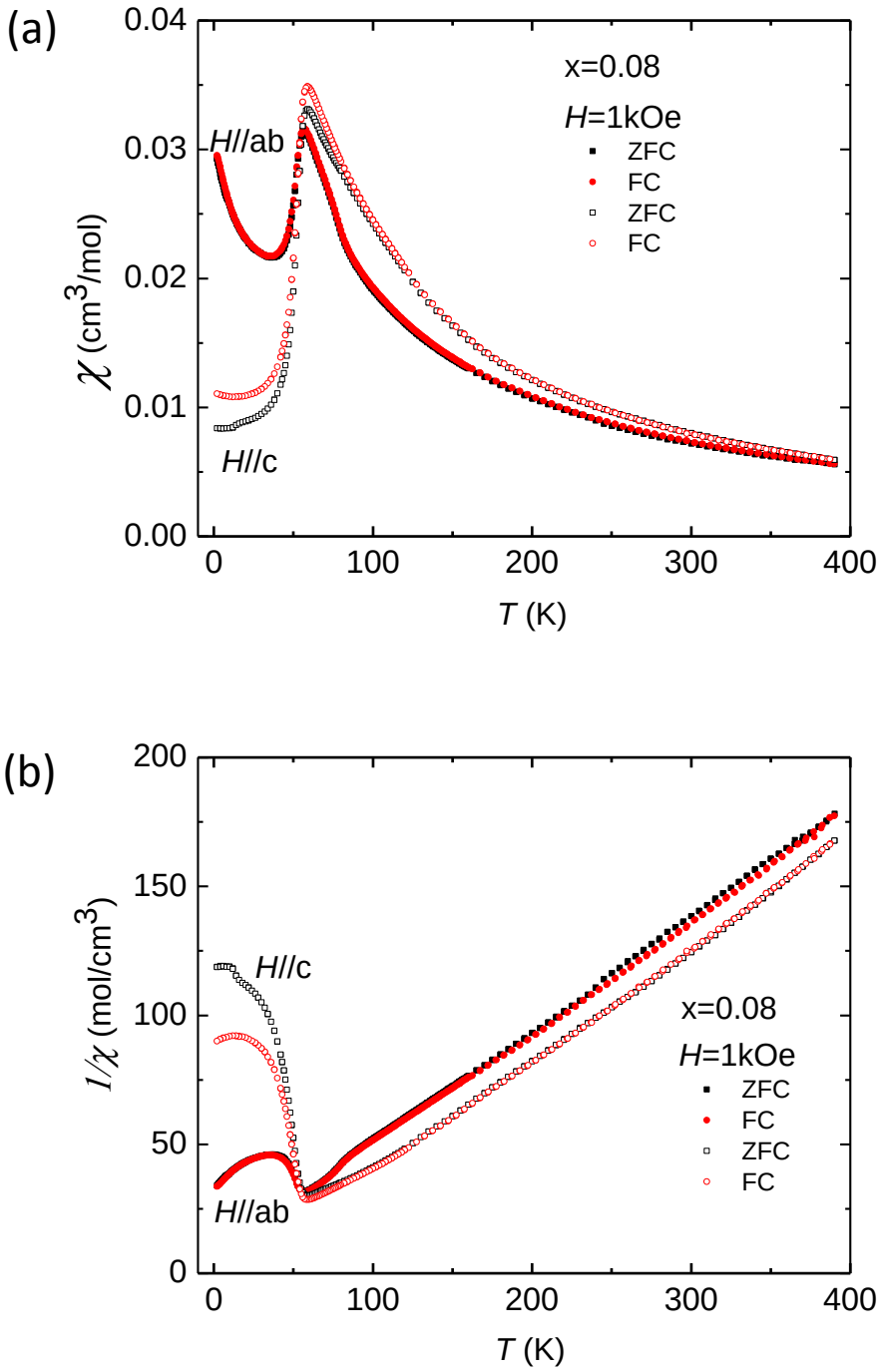

Figure 5.11 (a) Magnetic susceptibility χ as a function of T, measured in 1kOe with H//ab and H//c. (b) Inverse susceptibility $1/\chi$ vs T. Squares indicate ZFC condition while diamonds indicate FC condition. Solid symbols represent H//ab while open symbols represent H//c.

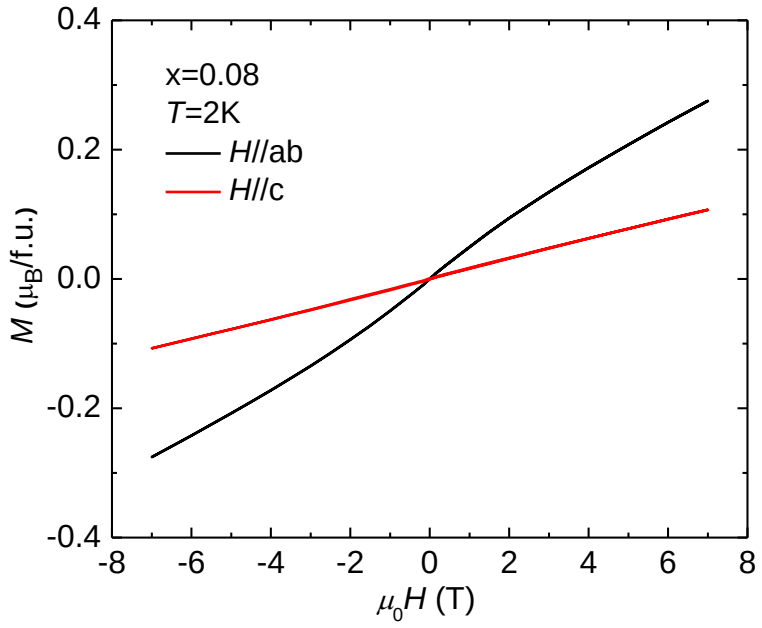

Figure 5.12 M vs H loops at 2 K for H//ab and H//c in crystal with x = 0.08.

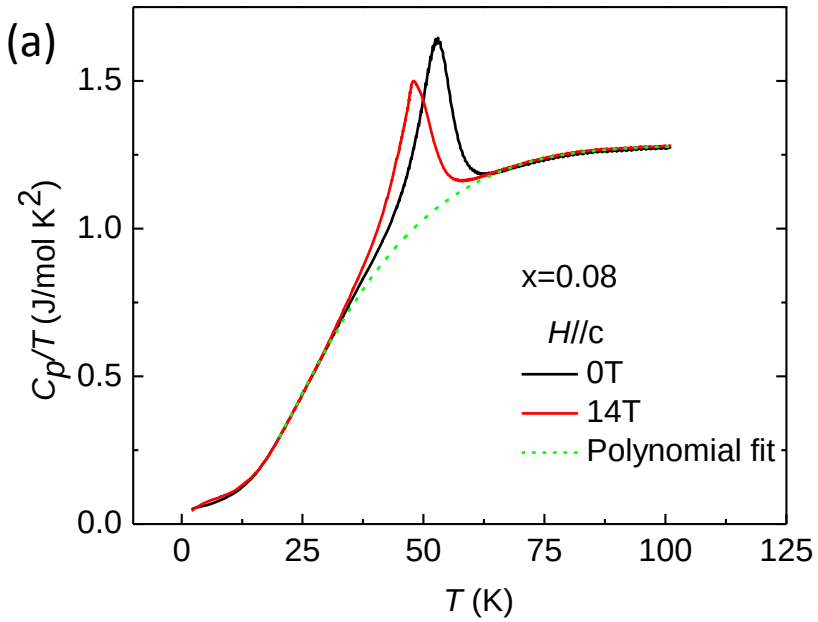

Figure 5.13 (a) Measured specific heat (C_p/T) as a function of T under 0 and 14 T magnetic fields. The dashed line represents the polynomial fit of specific heat data away from the transition regime. (b) Plot of C_p/T vs T^2 in zero field.

fig. cont'd

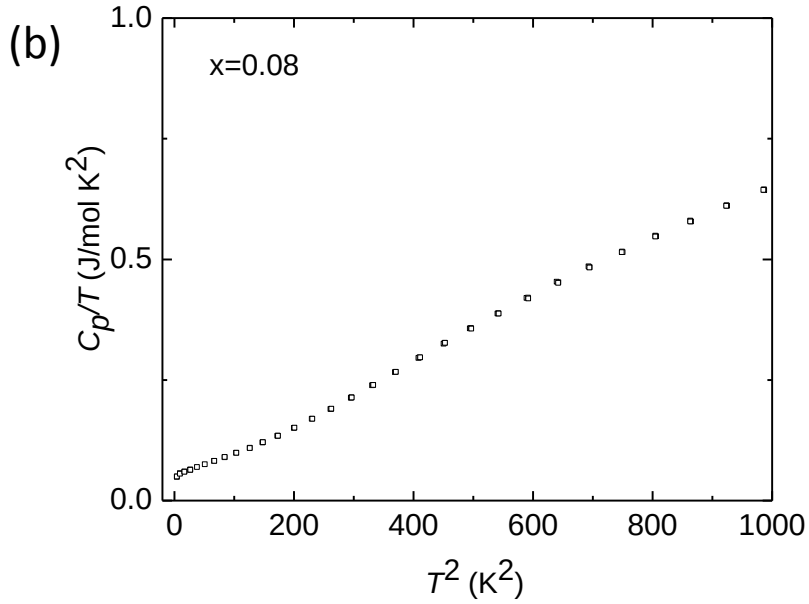

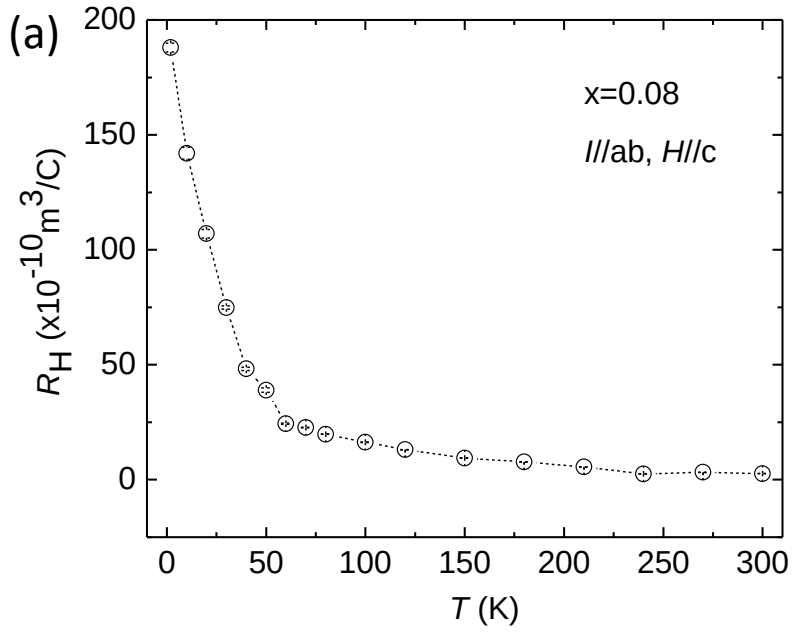

Figure 5.14 (a) Temperature dependence of Hall coefficient R_H in crystal with x = 0.08. (b) Field dependence of ρ_H at selected temperatures. The plot of ρ_H versus H is within 7 T.

fig. cont'd

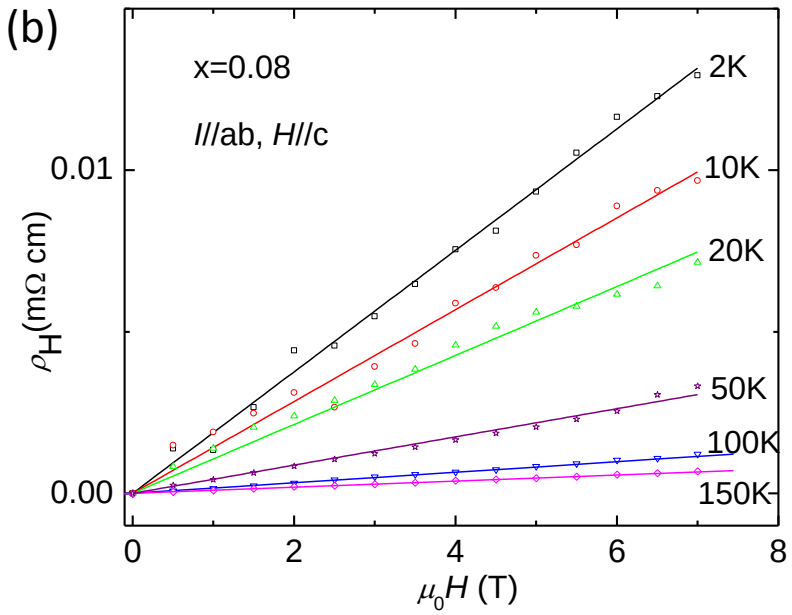

Here we recall field dependences of T_{MIT} in crystal with x = 0.06 (Figure 5.1 (d)) and x = 0.08 (Figure 5.8 (c)). How can we understand such a phenomenon? As mentioned in Chapter 1, our previous microscopic study on $Sr_3(Ru_{0.8}Mn_{0.2})_2O_7$ (nominal doping level x = 0.2) via SEM and STM/S revealed a phase separation scenario [26]. As shown in Figure 5.15 (a), the SEM image is homogeneous at high temperatures. When cooling down the sample to below T_{MIT} (about 135K), the SEM images show dark stripes (Figure 5.15 (b - d)). The *in-situ* STS *dI*/*dV* curve indicates a gap in the dark domains, meaning that the dark regions are insulating (Figure 5.15 (e)). The quantitative analysis of the domain areal change in a region of 30 x 30 μm^2 with temperature is displayed in Figure 5.15 (f). The area of insulating region increases with decreasing T until T reachs T_M (=50K). Below T_M, the insulating area tends to saturate. Moreover, as shown in Figure 1.5, the application of mechanical stress changes domain area, where the insulating phase expands dramatically at the expense of the metallic phase at a constant temperature. This dynamic evolution of domain area with applied stress in $Sr_3(Ru_{0.8}Mn_{0.2})_2O_7$ rendered a direct evidence of phase separation.

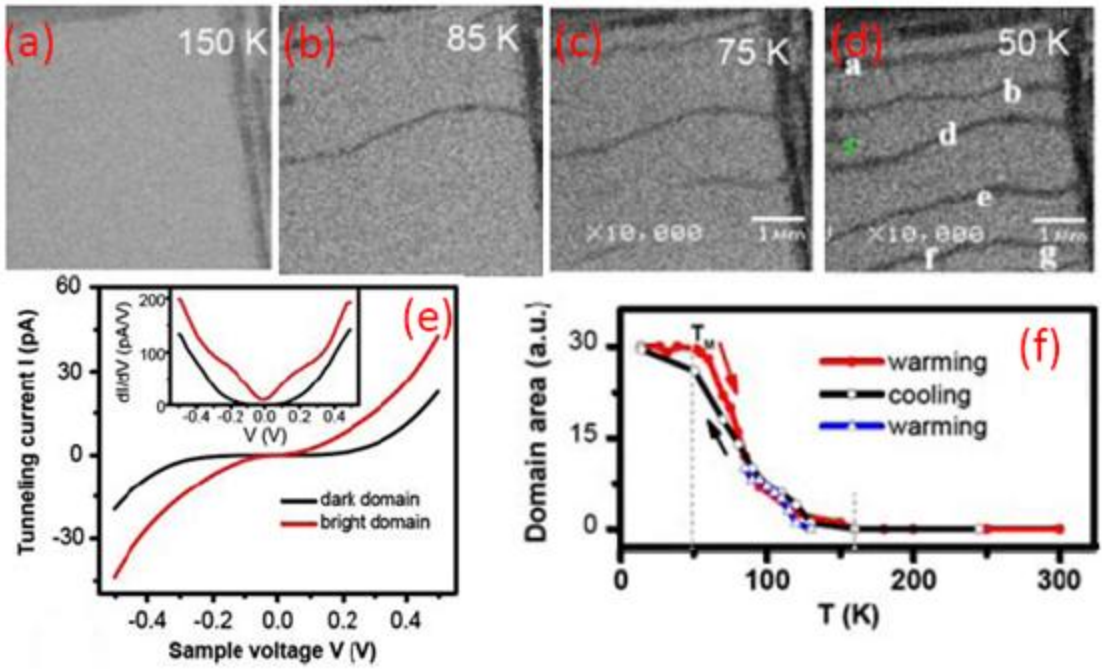

Figure 5.15 Temperature dependent phase percolation in $Sr_3(Ru_{0.8}Mn_{0.2})_2O_7$. (a) - (d) Domain images measured at various *T* for the same sample location. (e) Averaged tunneling *I(V)* curves and derivative conductance (*dI/dV*) curves measured in bright and dark domains. An energy gap is seen in tunneling *I(V)* curve of dark domain, which is further confirmed by *dI/dV* data. Figures adapted from [26]

Stimulated by this direct experimental fact on phase separation scenario, we believe that the origin of the strong field dependences of T_{MIT} is due to the modification of electronic phase distribution. As illustrated in Figure 5.16, the shaded region represents insulating domains while the bright region represents metallic domains. The insulating domains in the crystal connect each other to form a dense insulating network under zero field (Figure 5.16 (a)). The shape and size of insulating and metallic domains may change as applied magnetic field. Under magnetic field, the metallic domains likely expand at the expense of the insulating one and become larger to form a metallic percolation network in the entire crystal (Figure 5.16 (b) and (c)). Electrons or holes choose the easiest channel to move through the crystal. Thus, the scattering rate reduces greatly and the upturn of resistivity below T_{MIT} is suppressed by applied magnetic field.

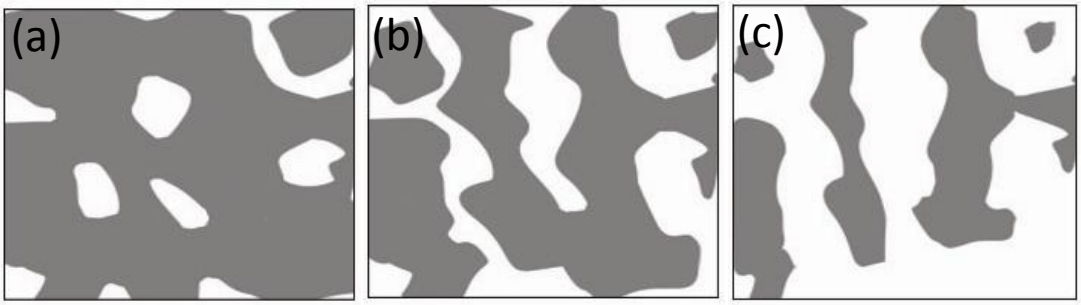

Figure 5.16 Illustration of electronic phase separation. The shaded area represents insulating domains while the bright area represents metallic domains.

5.3 Physical Properties of $Sr_3(Ru_{1-x}Mn_x)_2O_7$ (x = 0.16)

We observe a metallic-to-insulating crossover in crystal with x = 0.16, as shown in Figure 5.17. The slope $d\rho_{ab}/dT$ changes its sign at T_{MIT} = 136 K (inset of Figure 5.17 (a)) under zero field. The in-plane transverse MRs $\Delta\rho_{ab}^{\perp}/\rho_{ab}$ (I//ab, $H \perp I$) of crystal with x = 0.16 at selected temperatures for H//ab and H//c are shown in Figure 5.17 (b). The MRs of crystal with x = 0.16 for ρ_{ab} are negative at low temperatures (e.g. black squares (2 K)) and positive at high temperatures (e.g. purple stars (300 K)). Figure 5.18 (a) shows the temperature dependence of ρ_c (I//c) under zero field in crystal with x = 0.16. ρ_c monotonically increases with decreasing T at the whole temperature range. The out-of-plane longitudinal MR $\Delta\rho_c^{//}/\rho_c$ (I//c, H//I) and transverse MR $\Delta\rho_c^{\perp}/\rho_c$ (I//c, $H \perp I$, H//ab) of crystal with x = 0.16 at selected temperatures are shown in Figure 5.18 (b). Obviously, the absolute values of $\Delta\rho_c^{//}/\rho_c$ are smaller than those of $\Delta\rho_c^{\perp}/\rho_c$ at high fields.

The temperature dependences of χ_{ab} (H//ab) and χ_c (H//c) magnetic susceptibility are shown in Figure 5.19 (a). A magnetic field of 1 kOe is applied parallel to *ab*-plane or *c*-axis. The measurements are taken under both ZFC and FC conditions. Both χ_{ab} and χ_c show a peak at T_M = 80 K. Inverse susceptibility $1/\chi$ as a function of T is shown in Figure 5.19 (b). Above 175 K $1/\chi$ shows a good linear behavior and both $\chi_{ab}(T)$ and $\chi_c(T)$ can be fitted with a formula $\chi(T) = \chi_0 + \chi_{CW}(T)$ at high temperature range. The obtained p_{eff} and Θ_{CW} from the fitting on ZFC measurement between

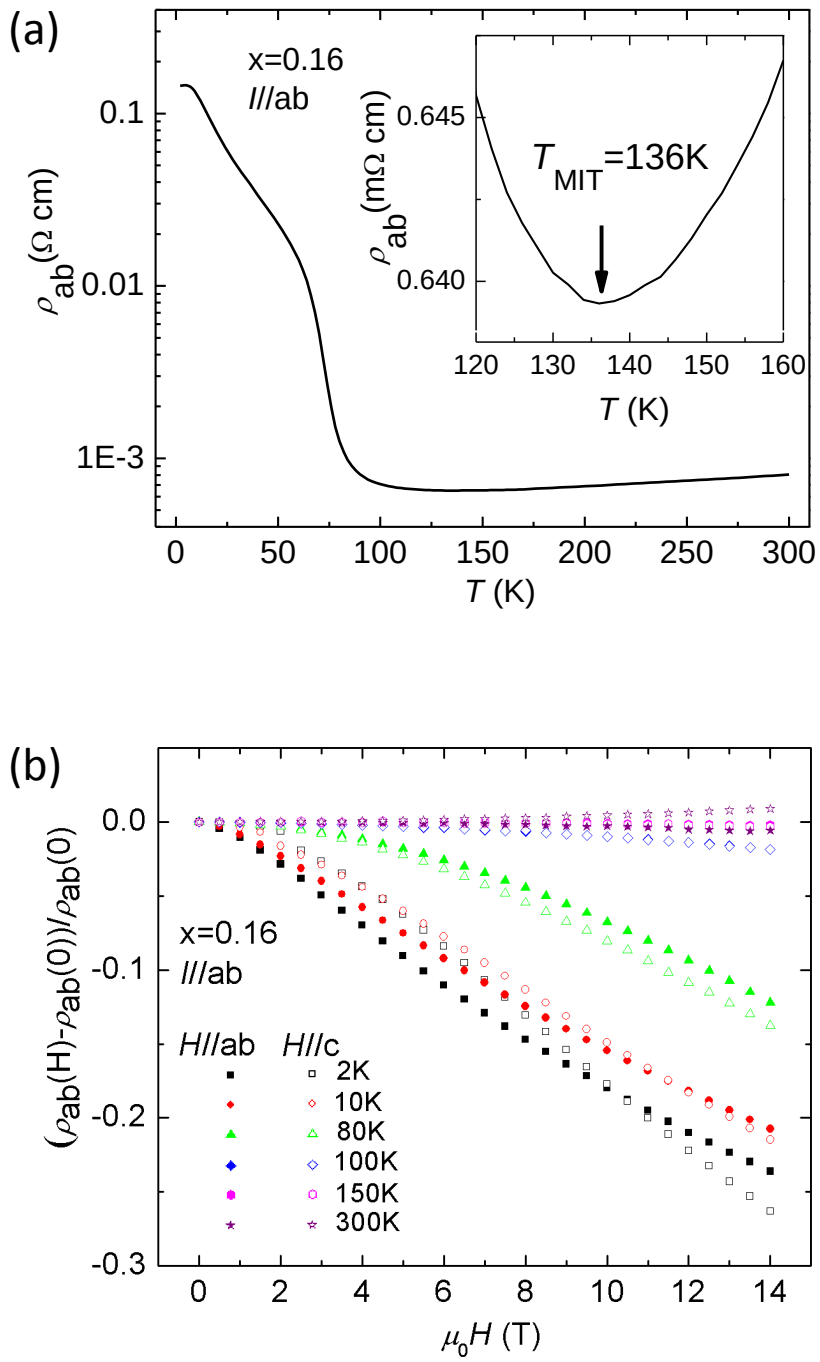

Figure 5.17 (a) Temperature dependences of ρ_{ab} (T) for x = 0.16 under zero field. The inset of (a) shows the T_{MIT} (= 136 K) of ρ_{ab} for x = 0.16 under zero field. (b) In-plane transverse MR $\Delta\rho_{ab}^{\perp} / \rho_{ab}$ in H//c configuration (I//ab, $H \perp I$; open symbols) and H//ab (I//ab, $H \perp I$; solid symbols) for x = 0.16 at different temperatures.

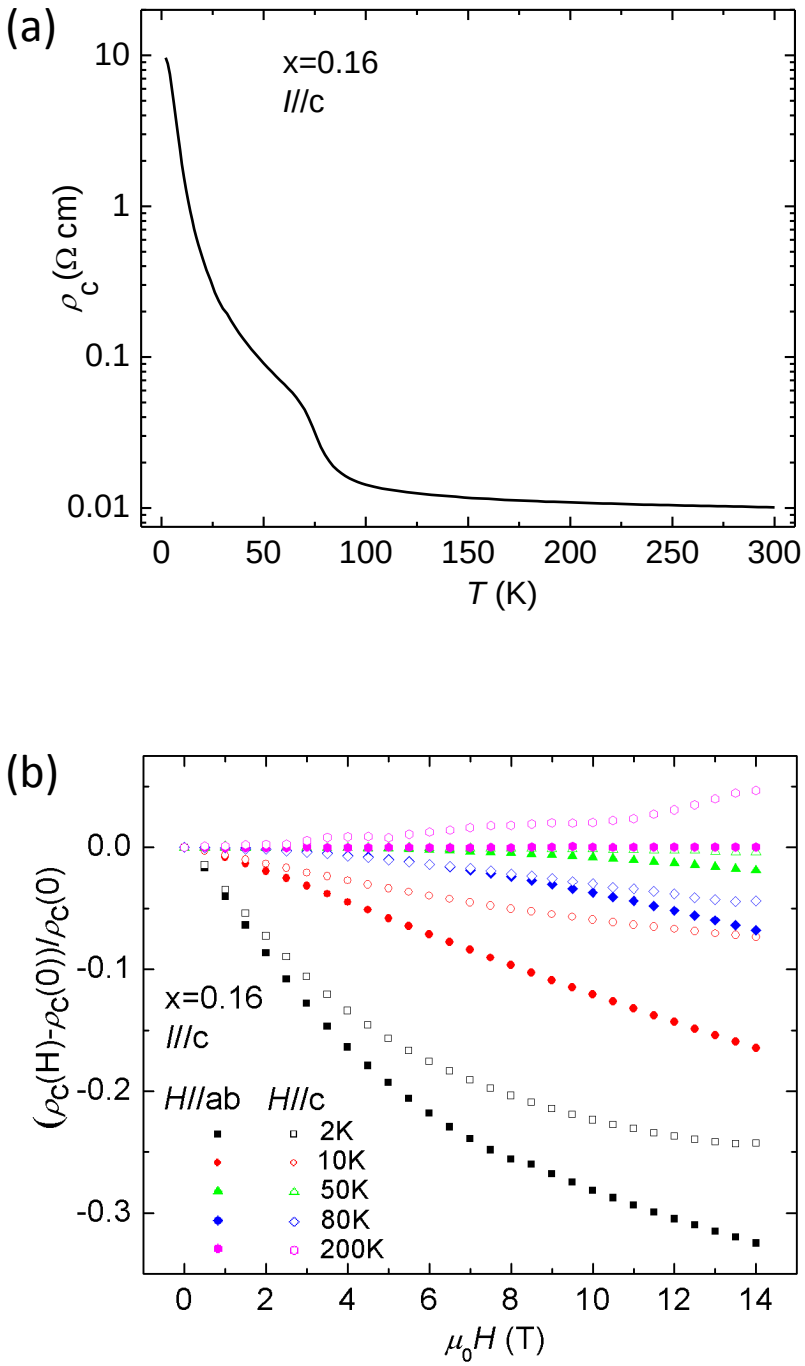

Figure 5.18 (a) Temperature dependences of ρ_c (T) for x = 0.16 under zero field. (b) Out-of-plane longitudinal MR $\Delta\rho_c^{//} / \rho_c$ (I//c, H//c; open symbols) and transverse MR $\Delta\rho_c^{\perp} / \rho_c$ (I//c, $H \perp I$, H//ab; solid symbols) for x = 0.16 at selected temperatures.

175 K and 390 K for crystal x = 0.16 are p_{eff}^{ab} = 3.36 (p_{eff}^{c} =3.37) and Θ_{CW}^{ab} = -3 K (Θ_{CW}^{c} = -1 K) for H//ab (H//c). The negative values of Θ_{CW} suggest AFM interactions at high temperatures. As shown in Figure 5.20, magnetization (M) versus field (H) measurement at 2 K shows a straight line for H//c while a slight deviation from linearity is discernible for H//ab.

The temperature dependence of the specific heat for x = 0.16 shows a specific heat anomaly around T_M (80 K), as shown in Figure 5.21 (a). Similar to crystal with x = 0.08, there is a clear change with an applied 14 T field. The derived p_{eff} from Curie-Weiss law fitting in x = 0.16 yields S = 1.25 for both H//ab and H//c. The expected magnetic entropy removed upon ordering is S_M = 1.25 R. In order to estimate the quantitative magnetic entropy removal near T_M, we fit the experimental data (zero field) at 30 ≤ T ≤ 50 K and 100 ≤ T ≤ 200 K using a polynomial (Dashed green line in Figure 5.21 (a)). After subtracting the background from the polynomial fitting, we obtain the entropy change associated with the transition $\Delta S \sim 0.77 \pm 0.03$ R, which is much smaller than the expected S_M. This suggests partial entropy above T_M and some spins remain unordered. Figure 5.21 (b) shows plots of C_p/T vs T^2 in zero field for x = 0.16. The T^2 dependence of C_p/T shows a non-linear behavior at lower temperatures, which may attribute to the magnetic ordering in crystal with x = 0.16.

We have observed evidences of AFM ordering features in crystal with x = 0.06, 0.08 and 0.16 from magnetic susceptibility and MR and specific heat measurements. In x = 0.06 and 0.08, the T_{MIT} is very close to T_M while they are far apart in x = 0.16. To understand the nature of magnetic ordering at T_M, we carried out elastic neutron scattering experiment on crystal with x = 0.16. The sample is a half-cylinder shape (diameter ~ 5mm; height ~ 21mm) crystal with a mass 1.63 gram. The skin layer of the sample, comprising tiny purity phase Sr_2RuO_4, has been removed by scratching with great caution. The crystal is oriented in the tetragonal [h k 0] scattering plane and mounted in a closed-cycle He^4 refrigerator. Horizontal collimation is chosen as 48'-48'-40'-60' between source

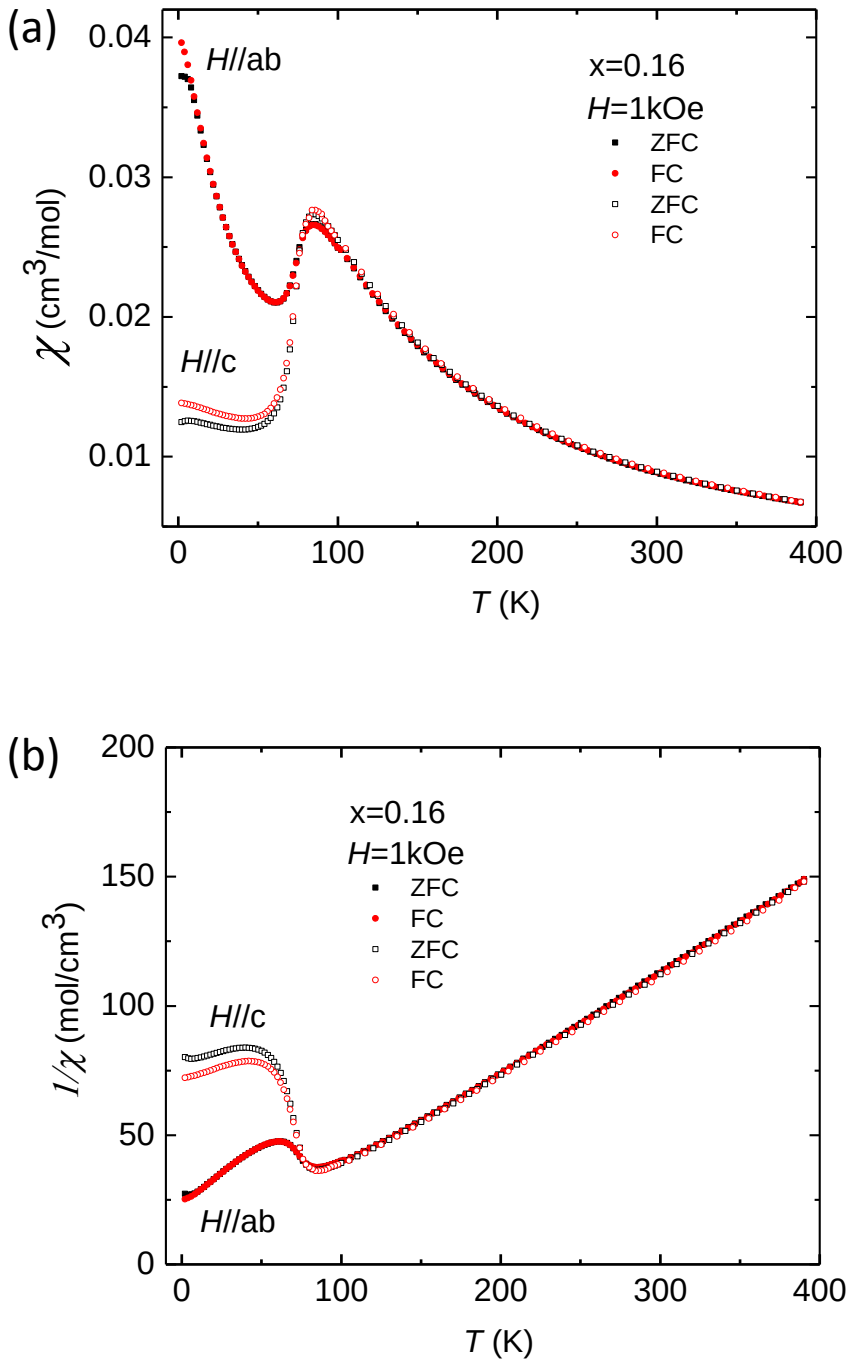

Figure 5.19 (a) Magnetic susceptibility χ as a function of T, measured in 1 kOe in-plane and out-of-plane in crystal x = 0.16. (b) Inverse susceptibility $1/\chi$ vs T.

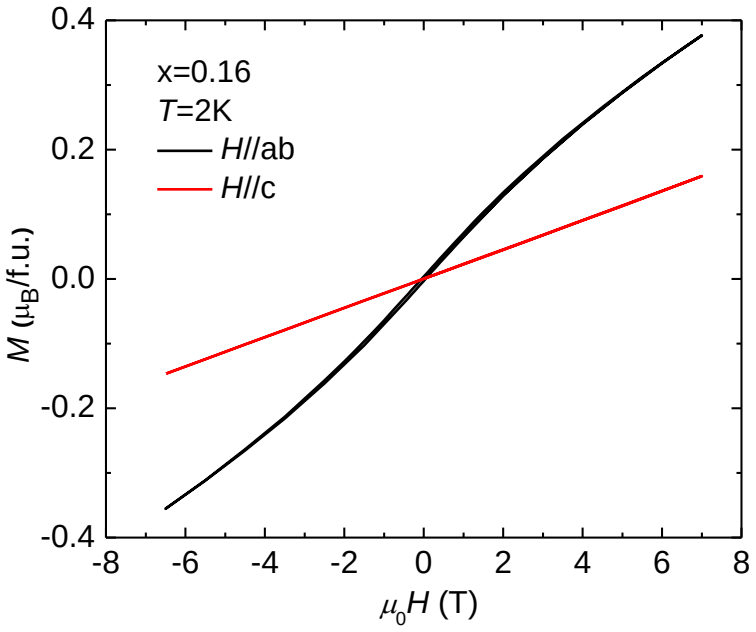

Figure 5.20 Magnetization (M) vs field (H) loops at 2 K for H//ab and H//c in crystal with x = 0.16.

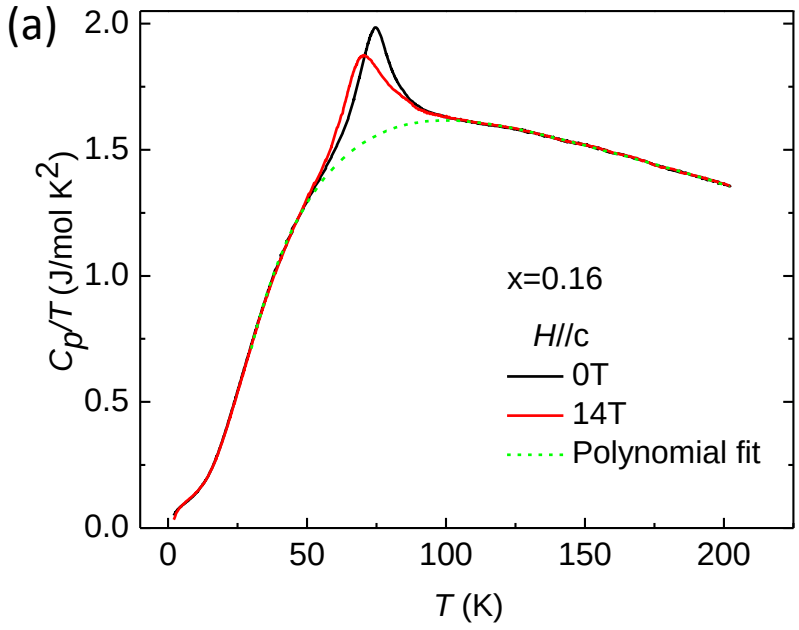

Figure 5.21 (a) Measured specific heat (C_p/T) as a function of T under 0 and 14 T magnetic fields in crystal with x = 0.16. The dashed line represents the polynomial fit of specific heat data away from the transition regime. (b) Plot of C_p/T vs T^2 in zero field.

fig. cont'd

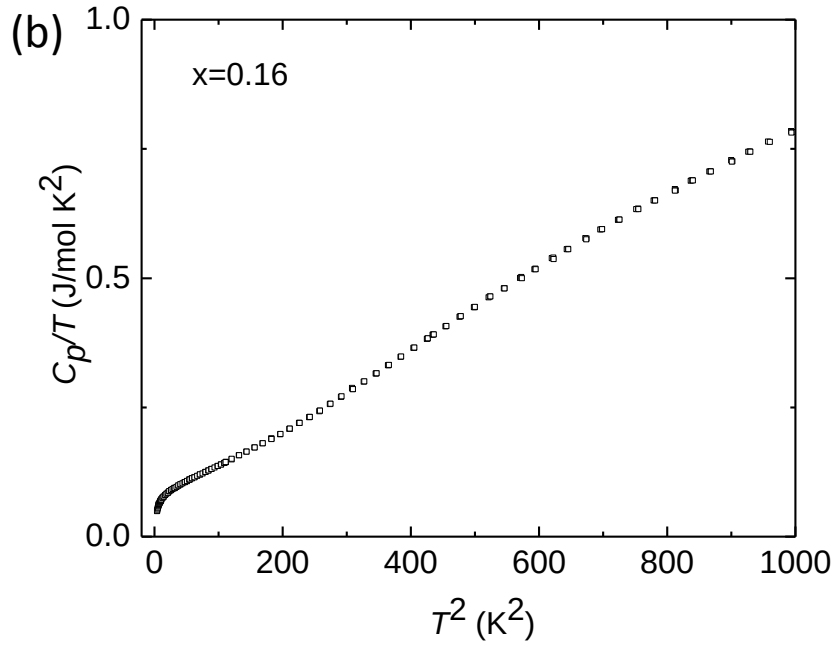

and monochromator, monochromator and sample, sample and analyzer, and analyzer and detector, respectively. All data presented here result from fixing the incident energy is $E_i = 14.6\,\text{meV}$.

We observe a magnetic reflection (1/4, 1/4, 0) at lower temperature, which reflect an AFM ordering and is adopted as an order parameter to study the magnetic ordering in crystal with x = 0.16. Figure 5.22 (a) is the integrated intensity of peak (1/4, 1/4, 0) as a function of temperature (left axis). The intensity drastically increases with decreasing temperature around 80 K, and then shows a trend to saturation up to our measured base temperature (12 K). These phenomena clearly indicate a magnetic transition below T_M. To probe the nature of magnetic ordering in crystal with x = 0.16, we use Gaussian function to fit peak (1/4, 1/4, 0) below T_M and Lorentzian function above T_M to extract temperature dependence of full width of half maximum (FWHM). FWHM (right axis in Figure 5.22) remains unchanged from 75 K to base temperature 12 K and is close the HB1A instrument resolution limit, suggesting a long-range AFM ordering at low temperatures. To probe possible short-range

magnetic correlations above T_M, we study diffuse scattering via a long time scan along (*h*, *h*, 0) direction around peak (1/4, 1/4, 0). Figure 5.23 shows scans along (*h*, *h*, 0) around (1/4, 1/4, 0) at 80 K (a), 85 K and 90 K (b). A common background has been subtracted for T = 80 K, 85 K and 90 K. The peak (1/4, 1/4, 0) at 12 K is very sharp and drastically decreases when approaching 80 K upon warming and the FWHM becomes larger. The intensity of peak (1/4, 1/4, 0) becomes much weaker at 85 K and the FWHM becomes much wider associated with a large error (Figure 5.22 right axis). As displayed in Figure 5.23 (b), only a trace of peak is shown at 90 K (dashed blue line). So we conclude that there is a long-range AFM ordering below T_M in crystal with x = 0.16 and a possible short-range magnetic correlations above T_M because they only survive in a very narrow temperature range.

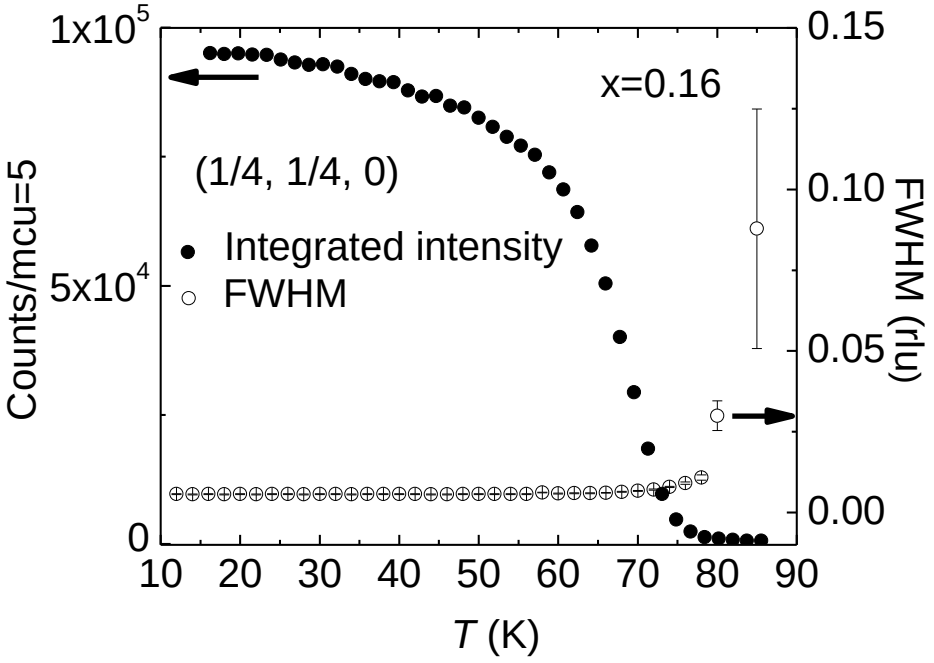

Figure 5.22 Temperature dependence of integrated intensity (left axis) and FWHM (right axis) of peak (1/4, 1/4, 0) in crystal with x = 0.16.

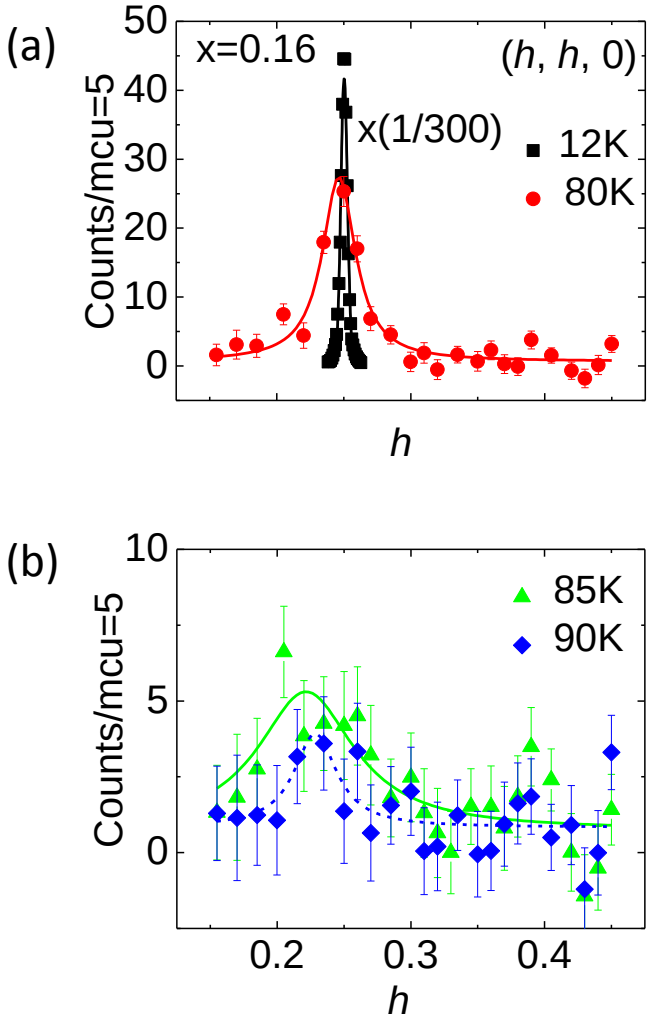

Figure 5.23 Long time scans along (*h*, *h*, 0) direction around peak (1/4, 1/4, 0) at 12 K and 80 K (a), 85 K and 90 K (b). Dashed line is a guide to eyes.

Based on the preliminary results from elastic neutron scattering measurement on crystal with $x = 0.16$, we suggest an *E*-type AFM magnetic structure. Figure 5.24 shows the proposed magnetic structure. The solid black square represents a crystallographic lattice unit cell. The dashed green square indicates magnetic lattice unit cell. Spin has a configuration of up up down down along either *ab* plane or *c* axis. The full determination of magnetic structure needs to take four-circle neutron diffraction measurement.

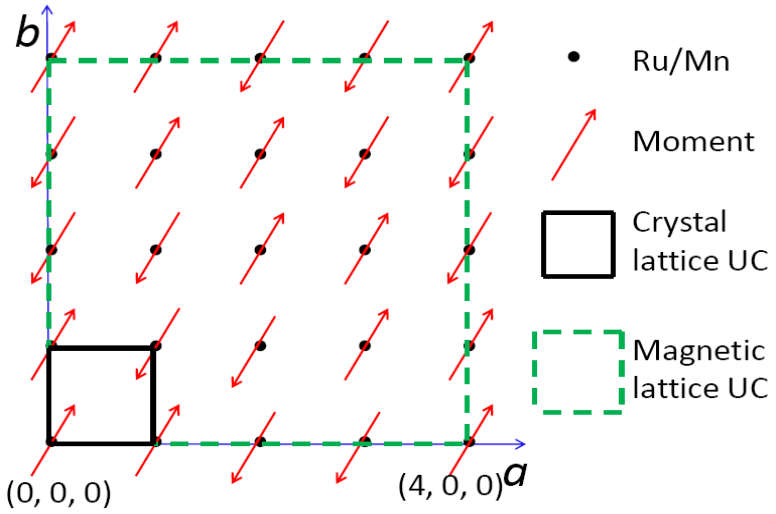

Figure 5.24 Proposed *E*-type AFM magnetic structure in crystal with $x = 0.16$.

The temperature dependence of the Hall coefficient R_H in crystal with $x = 0.16$ is shown in Figure 5.25 (a), where R_H is negative at low temperatures and positive at high temperatures. The sign of R_H changes around T_M, suggesting the change of the type of dominated charge carriers.

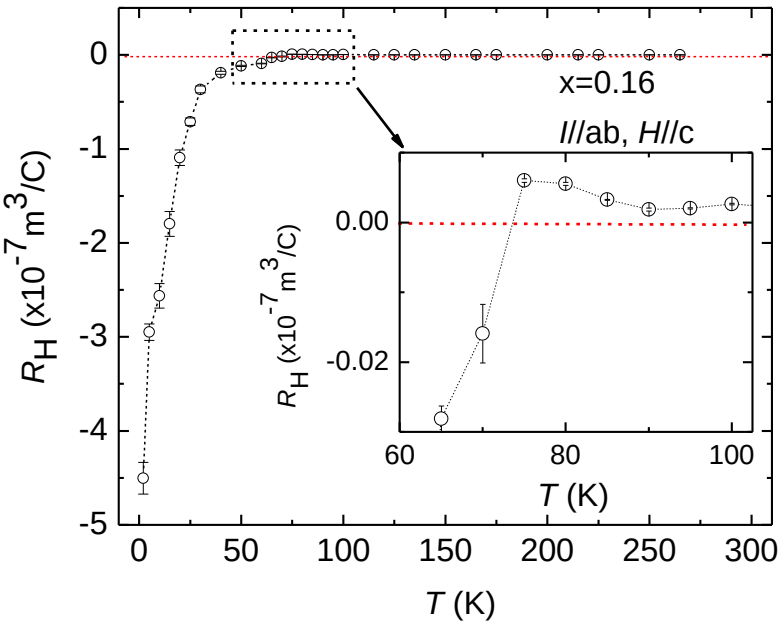

Figure 5.25 (a) Temperature dependence of Hall coefficient R_H in crystal with $x = 0.16$. The inset shows an enlargement of ρ_H versus T around T_M.

5.4 Physical Properties of $Sr_3(Ru_{1-x}Mn_x)_2O_7$ (x = 0.2)

The temperature dependences of ρ_{ab} and ρ_c for crystal with x = 0.2 are shown in Figure 5.26. The slope $d\rho_{ab}/dT$ changes the sign at T_{MIT} = 260 K (inset of Figure 5.26) while ρ_c monotonically increases with decreasing T at the whole temperature range. The in-plane transverse MR $\Delta\rho_{ab}^{\perp} / \rho_{ab}$ (I//ab, H//c) of crystal with x = 0.2 at selected temperatures are shown in Figure 5.27. The MR is negative at low temperatures (*e.g.* red circles (50K)) and positive at high temperatures (*e.g.* purple stars (300K)).

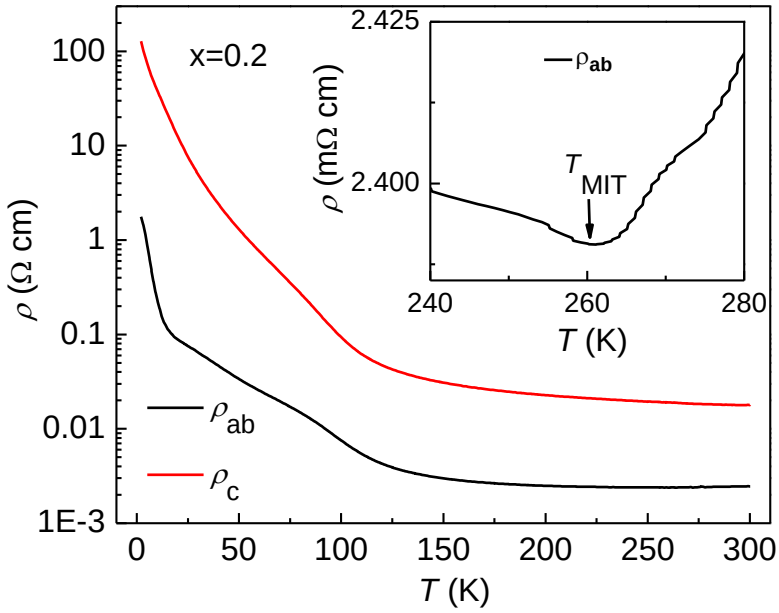

Figure 5.26 Temperature dependences of ρ_{ab} (black line) and ρ_c (red line) in crystal with x = 0.2.

Figure 5.28 (a) shows the temperature dependences of χ_{ab} and χ_c magnetic susceptibility for crystal with x = 0.2. A magnetic field of 1 kOe is applied parallel to *ab*-plane or *c*-axis. Both χ_{ab} and χ_c show a peak at T_M = 32 K. Inverse susceptibility $1/\chi$ as a function of T is shown in Figure 5.28 (b). Above 175 K $1/\chi$ shows good linear behavior and both $\chi_{ab}(T)$ and $\chi_c(T)$ can be fitted with a formula

$\chi(T) = \chi_0 + \chi_{CW}(T)$ at high temperature range. The obtained p_{eff} and Θ_{CW} from the fitting on ZFC measurement between 175 K and 390 K for crystal with $x = 0.2$ are $p_{eff}^{ab} = 3.29$ ($p_{eff}^{c} = 3.44$) and

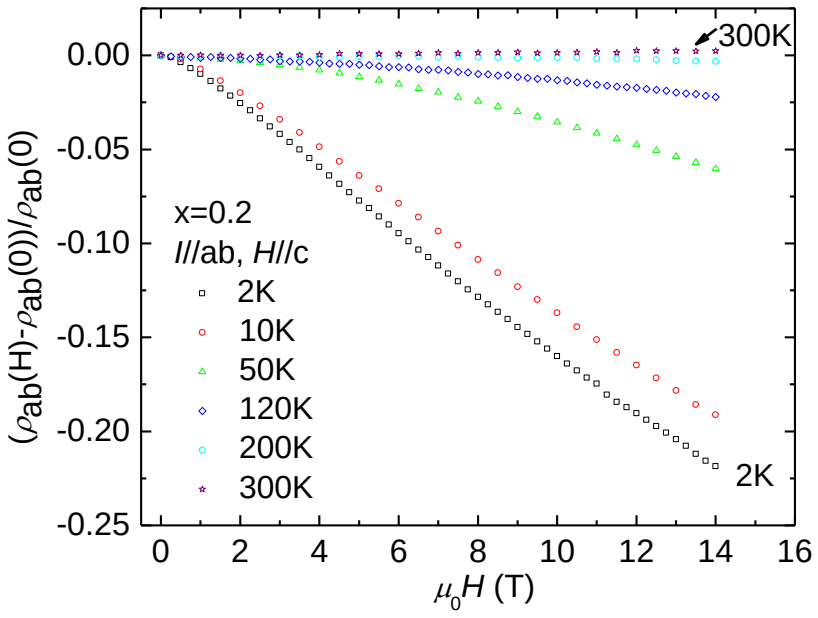

Figure 5.27 In-plane transverse MR $\Delta\rho_{ab}^{\perp} / \rho_{ab}$ (I//ab, H//c) of crystal with $x = 0.2$ at selected temperatures.

$\Theta_{CW}^{ab} = 21$ K ($\Theta_{CW}^{c} = 8$ K) for H//ab (H//c). The positive values of Θ_{CW} suggest FM interactions at high temperatures. Magnetization (M) versus field (H) measurements on crystal with $x = 0.2$ display a hysteresis for both directions at 2 K and 10 K, as shown in Figure 5.29. The loop area in 10 K is much smaller than that in 2 K.

Figure 5.30 (a) shows the temperature dependence of the specific heat (plotted as $C_p(T)/T$ versus T) for sample $x = 0.2$ between 2 K and 300 K under $H = 0$ T and 7 T (H//c). Different from those crystals with $x = 0.06$, 0.08 and 0.16, no specific heat anomaly emerges around T_M (32 K) under both 0 T and 7 T. As shown in Figure 5.30 (b), the data plotted as $C_p(T)/T$ vs T^2 shows a nonlinear behavior at lower temperatures. In addition, the temperature dependence of the Hall

coefficient R_H in crystal x = 0.2 is shown in Figure 5.31, where R_H is negative at the whole temperature range. The charge carriers in crystal with x = 0.2 are dominated by electrons.

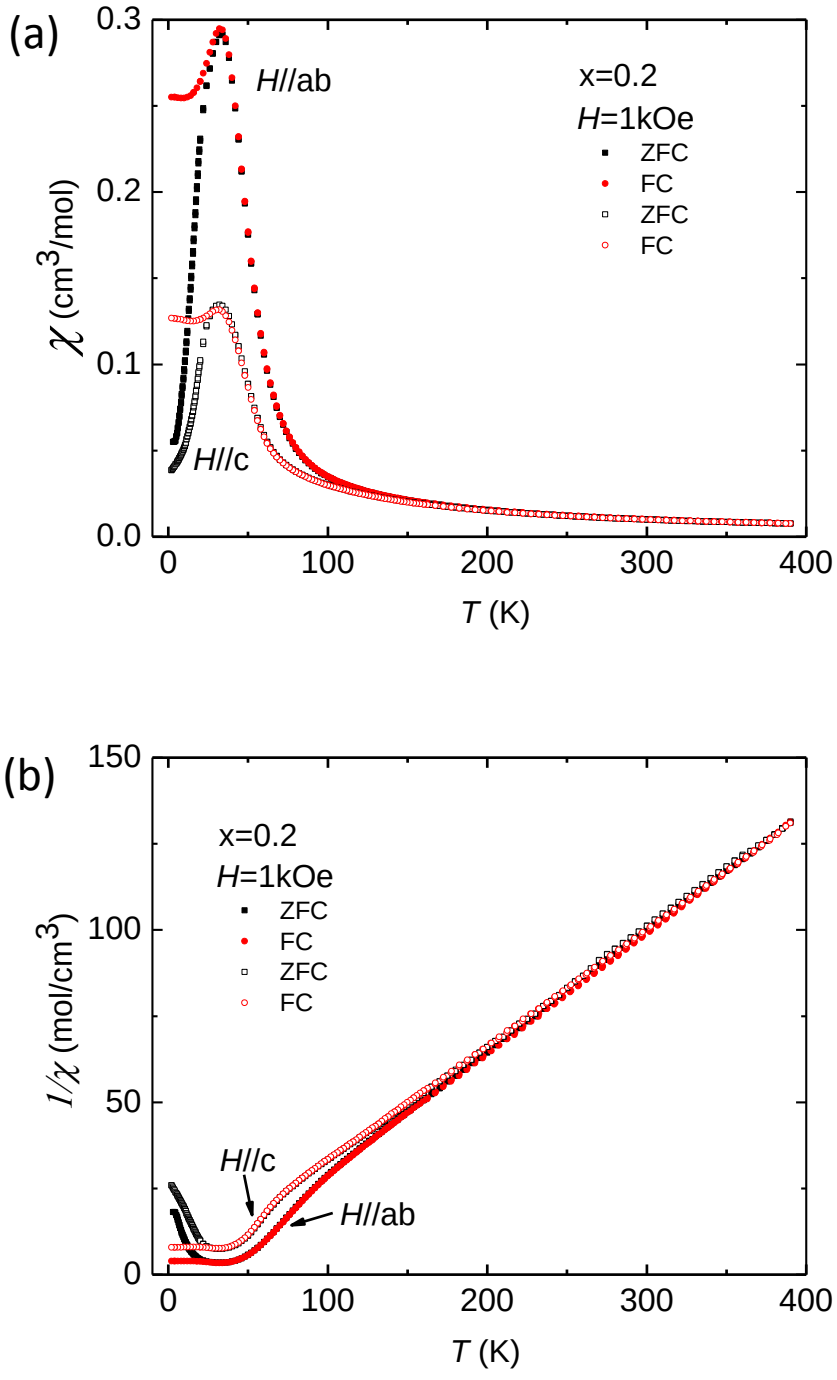

Figure 5.28 (a) Magnetic susceptibility χ as a function of T, measured in a field 1kOe for H//ab and H//c in crystal with x = 0.2. (b) Inverse susceptibility $1/\chi$ vs T.

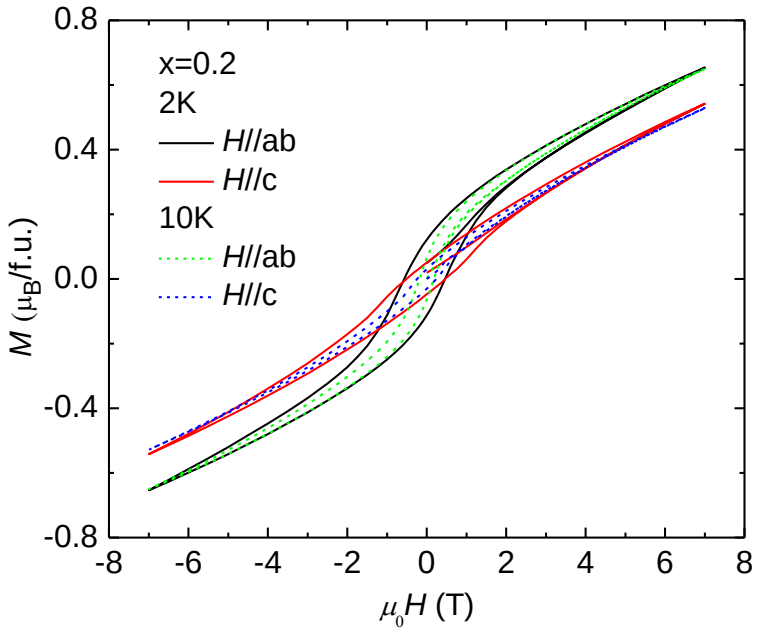

Figure 5.29 Magnetization (M) vs field (H) curves at 2 K (solid lines) and 10 K (dashed lines) for H//ab and H//c in crystal with x = 0.2.

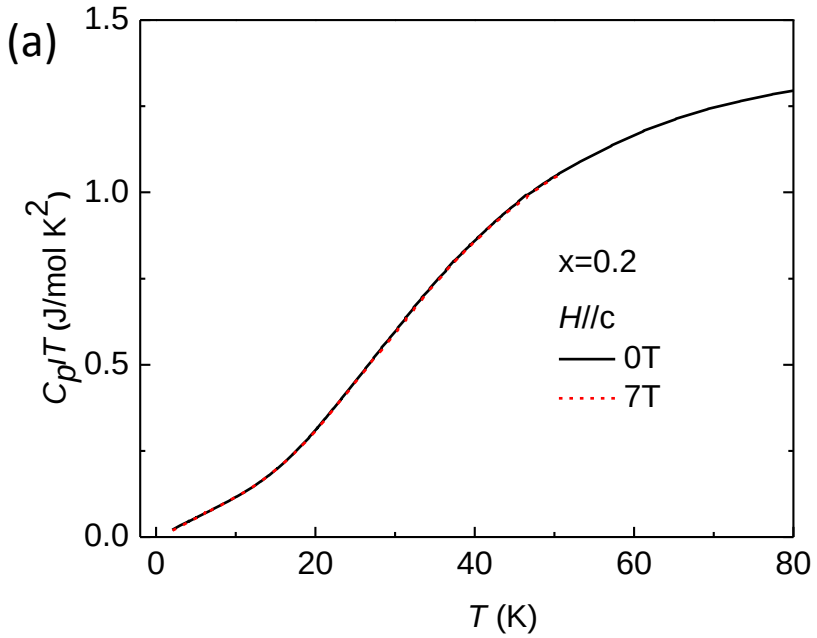

Figure 5.30 (a) Measured specific heat (C_p/T) as a function of T under 0 (solid black line) and 7 T (dashed red line) magnetic fields in crystal with x = 0.2. (b) Plot of C_p/T vs T^2 in zero field.

fig. cont'd

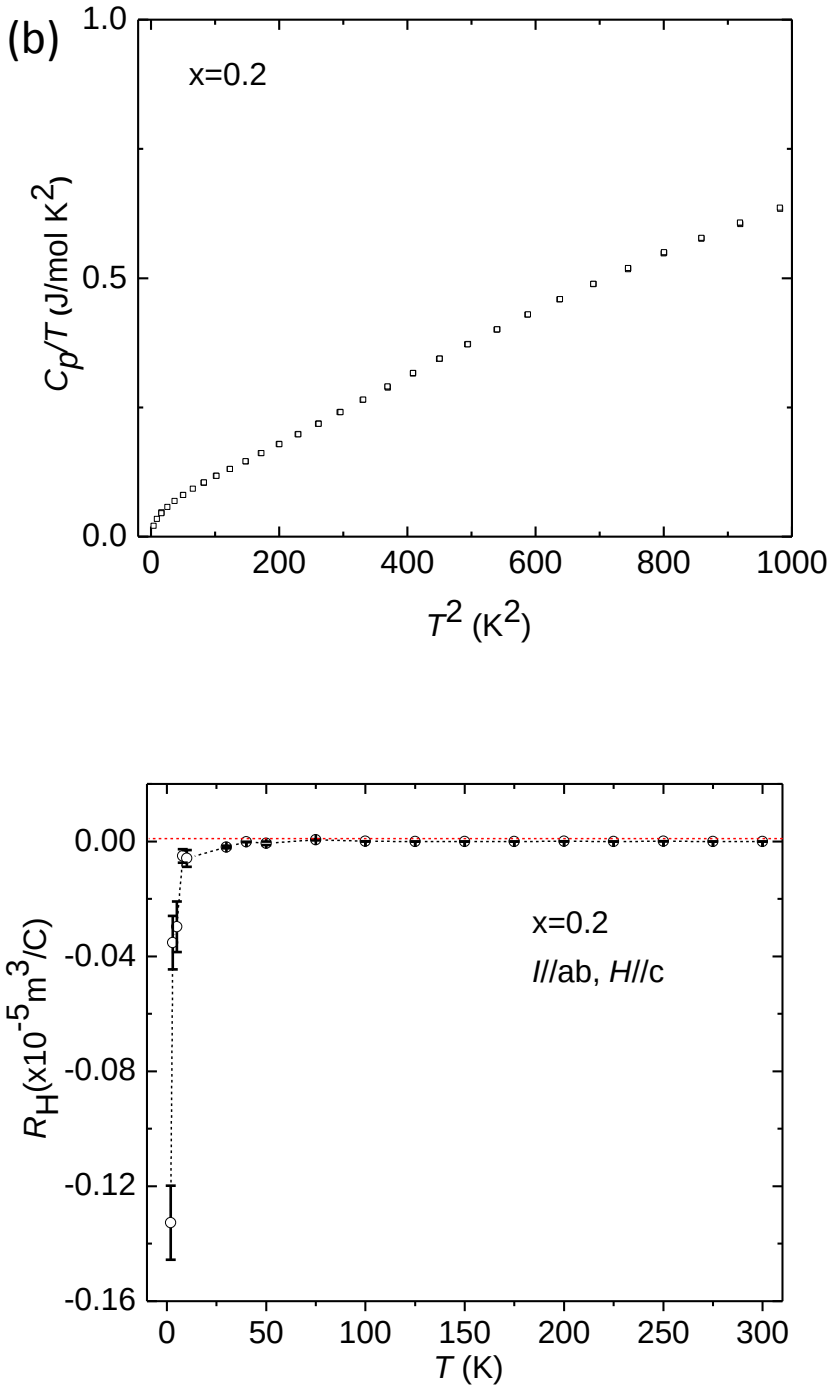

Figure 5.31 Temperature dependence of Hall coefficient R_H in crystal with x = 0.2.

5.5 Physical Properties of $Sr_3(Ru_{1-x}Mn_x)_2O_7$ (x = 0.33 and 0.7)

The temperature dependence of ρ_{ab} and ρ_c for crystal x = 0.33 and 0.7 are shown in Figure 5.32 and 5.33, respectively. The slope $d\rho_{ab}/dT$ in x = 0.33 changes the sign around 335 K while ρ_c monotonically increases with decreasing T at the whole temperature range. For crystal with x = 0.7, both ρ_{ab} and ρ_c show insulating behavior between 2 K and 390 K and do not show any sign change in $d\rho/dT$.

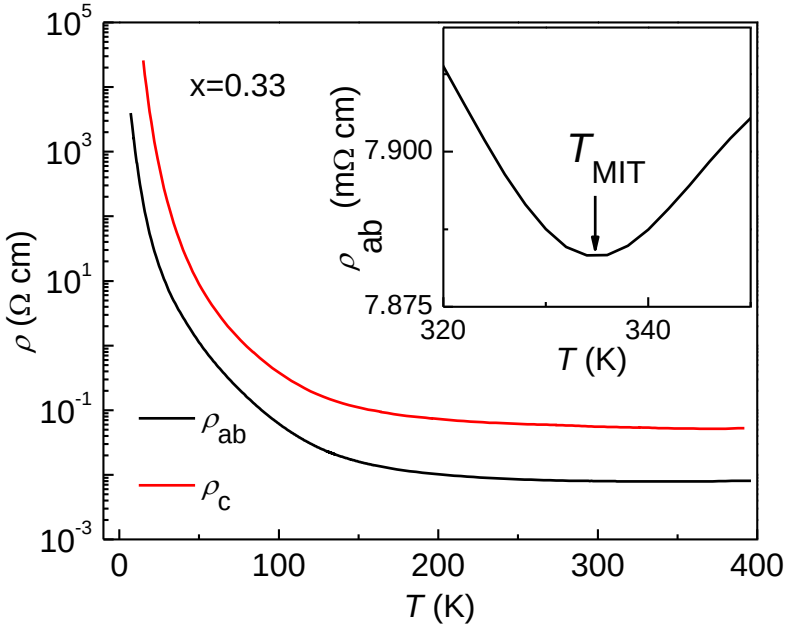

Figure 5.32 Temperature dependences of ρ_{ab} and ρ_c in crystal with x = 0.33. The inset shows the T_{MIT} (= 335 K) of ρ_{ab} for x = 0.33 under zero field.

The temperature dependences of χ_{ab} and χ_c magnetic susceptibility for crystal x = 0.33 and 0.7 are shown in Figure 5.34 (a) and 5.36 (a), respectively. A magnetic field of 1 kOe is applied parallel to *ab*-plane or *c*-axis. The measurements are taken under both ZFC and FC conditions. The T_M of crystal with x = 0.33 and 0.7 is 28 K and 27 K, respectively. The inverse susceptibility $1/\chi$ as a function of T in crystal with x = 0.33 and 0.7 is shown in Figure 5.34 (b) and 5.36 (b), respectively. $1/\chi$ shows linear behavior above 175 K in both compounds. Both χ_{ab} (T) and χ_c (T) can be fitted with

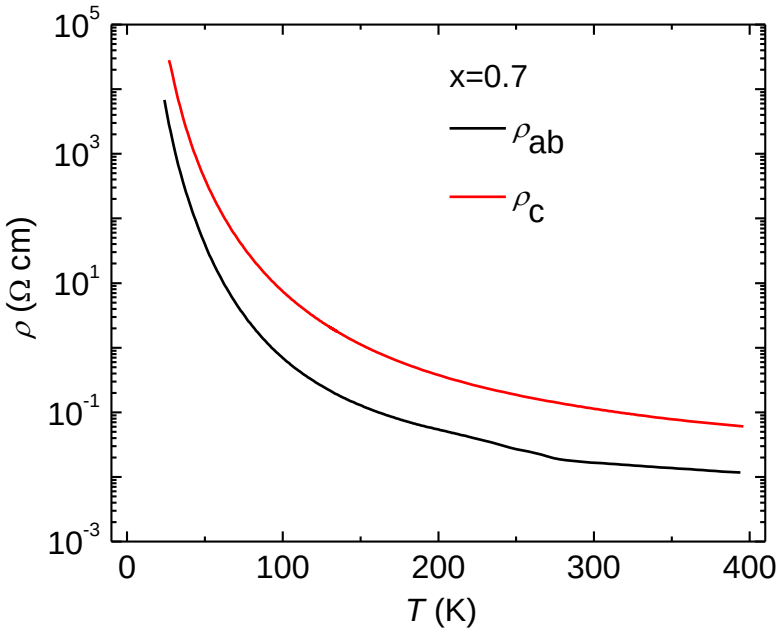

Figure 5.33 Temperature dependences of ρ_{ab} and ρ_c in crystal with x = 0.7.

a formula $\chi(T) = \chi_0 + \chi_{CW}(T)$ at high temperature range. The obtained p_{eff} and Θ_{CW} from the fitting on ZFC measurement between 175 K and 390 K for crystal x = 0.33 are p_{eff}^{ab} = 3.43 (p_{eff}^{c} = 3.49) and Θ_{CW}^{ab} = 13 K (Θ_{CW}^{c} = -5 K) for H//ab (H//c). The values of p_{eff} and Θ_{CW} in crystal with x = 0.7 are p_{eff}^{ab} = 3.70 (p_{eff}^{c} = 3.65) and Θ_{CW}^{ab} = 10 K (Θ_{CW}^{c} = -15 K) for H//ab (H//c). The mixed sign of values of Θ_{CW} in H//ab and H//c suggest a mixed FM and AFM interactions at high temperatures. Magnetization (M) versus field (H) measurements at 2 K for both crystal x = 0.33 (Figure 5.35) and 0.7 (Figure 5.37) display an evident hysteresis in both field directions. The loop area becomes smaller when increasing T, *e.g.* 28 K in x = 0.33 and 10 K in x = 0.7.

The temperature dependences of the specific heat for sample with x = 0.33 and 0.7 between 2 K and 200 K under H = 0 T and 7 T (H//c) are shown in Figure 5.38 (a) and 5.39 (a), respectively. No anomaly peak emerges around their respective T_M in both compounds. As shown in Figure

5.38(b) and 5.39 (b), the data plotted as $C_p(T)/T$ vs T^2 in both crystals with x = 0.33 and 0.7 show nonlinear behavior at lower temperatures.

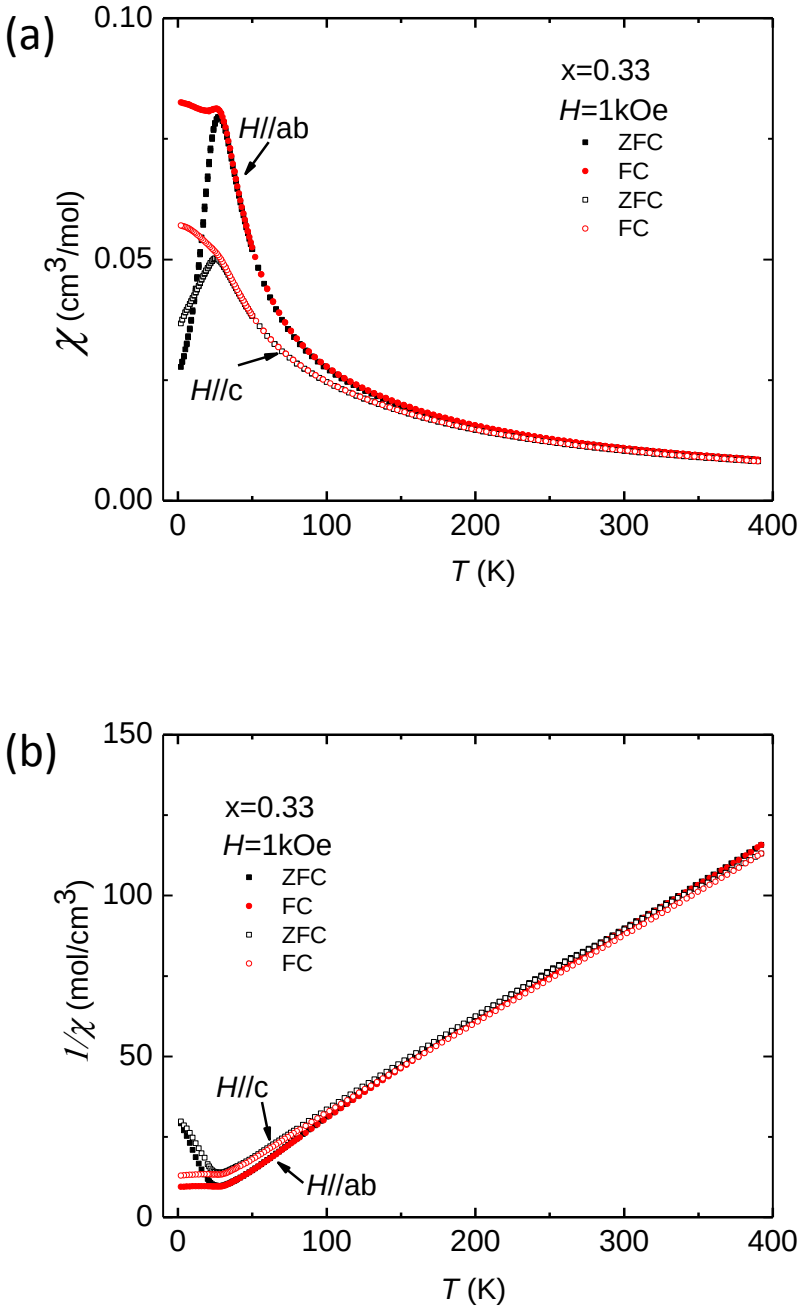

Figure 5.34 (a) Magnetic susceptibility χ as a function of T, measured in a field 1 kOe for H//ab and H//c in crystal with x = 0.33. (b) Inverse susceptibility $1/\chi$ vs T.

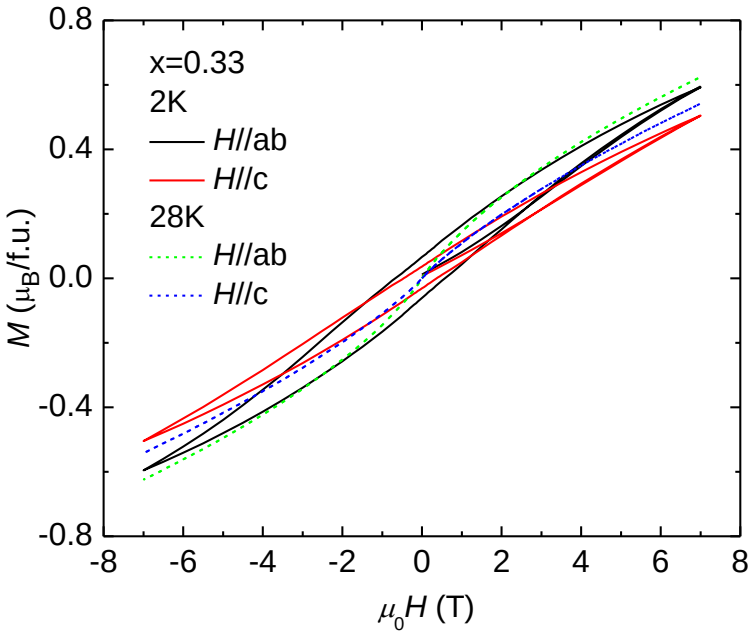

Figure 5.35 Magnetization (M) versus field (H) curves at 2 K (solid lines) and 28 K (dashed lines) for H//ab and H//c in crystal with x = 0.33.

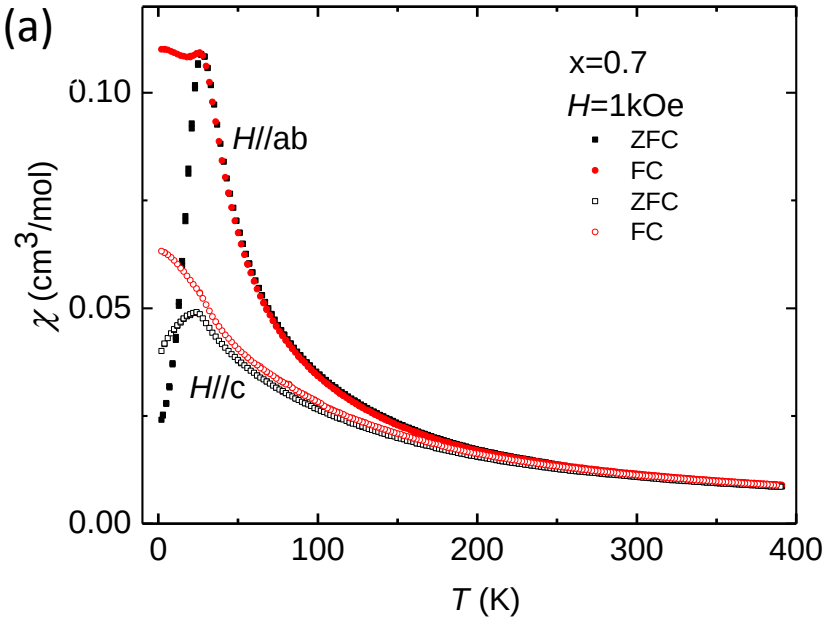

Figure 5.36 (a) Magnetic susceptibility χ as a function of T, measured in a field 1 kOe for H//ab and H//c in crystal with x = 0.7. (b) Inverse susceptibility $1/\chi$ vs T.

fig. cont'd

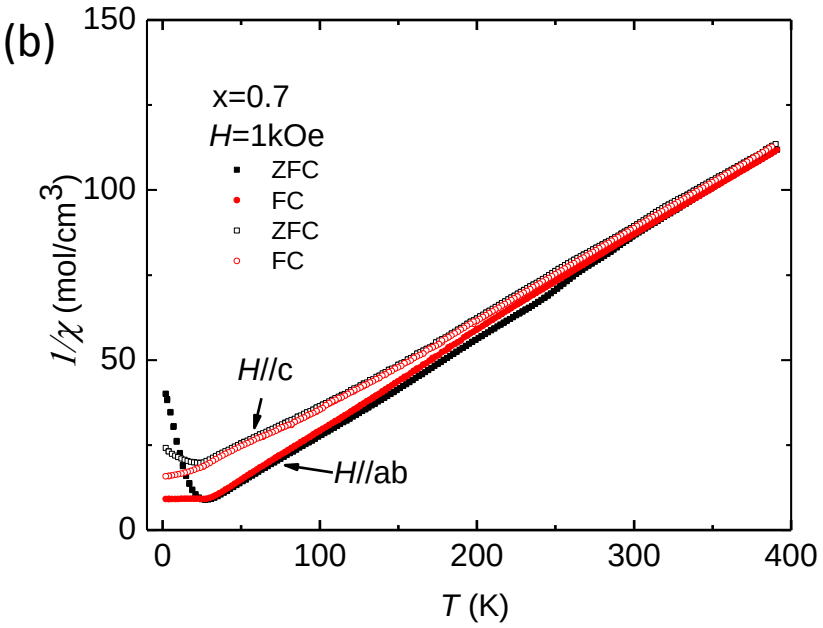

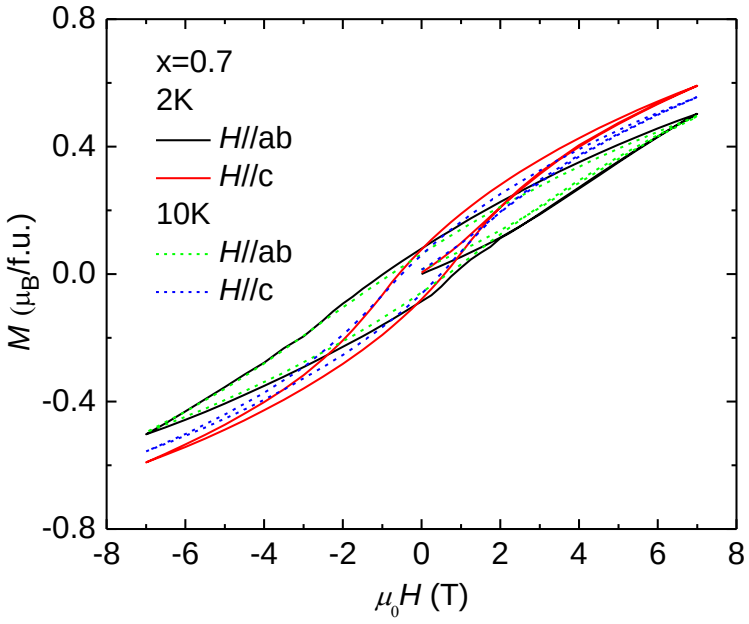

Figure 5.37 Magnetization (M) versus field (H) curves (solid lines) at 2 K and 10 K (dashed lines) for H//ab and H//c in crystal with x = 0.7.

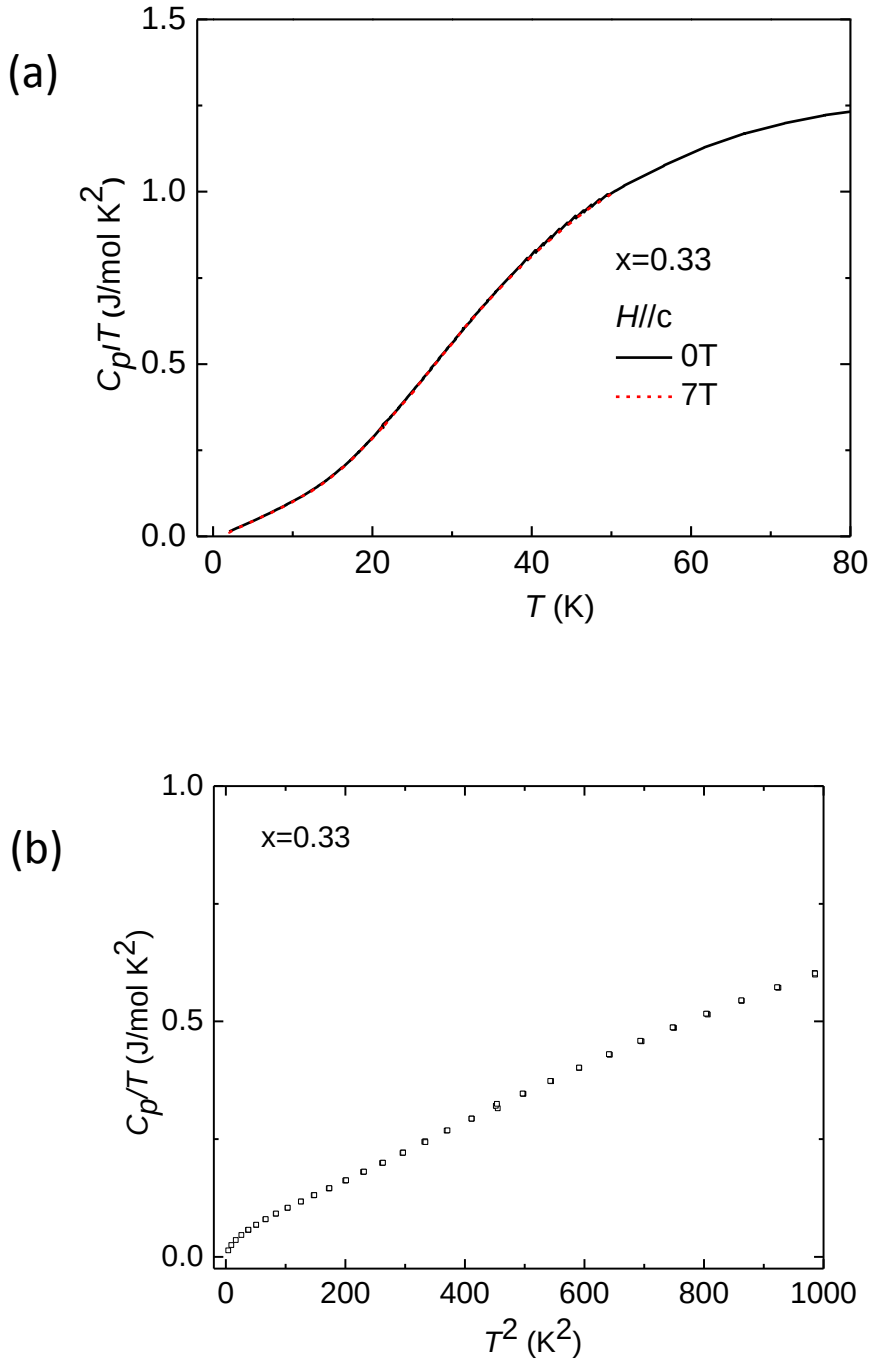

Figure 5.38 (a) Measured specific heat (C_p/T) as a function of T under 0 (black solid line) and 7 T (red dashed line) magnetic fields in crystal with x = 0.33. (b) Plot of C_p/T vs T^2 in zero field.

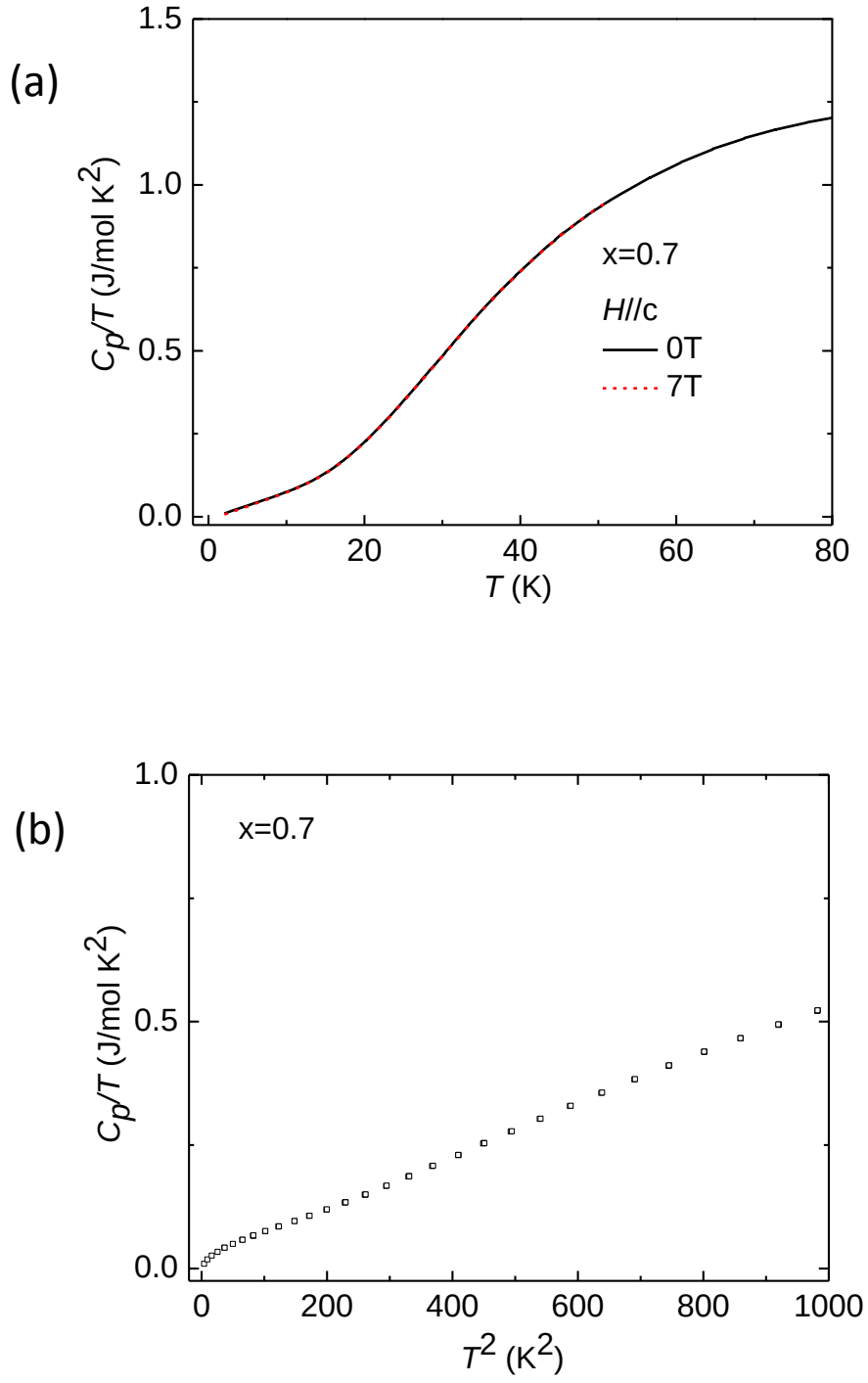

Figure 5.39 (a) Measured specific heat (C_p/T) as a function of T under 0 (black solid line) and 7 T (red dashed line) magnetic fields in crystal with x = 0.7. (b) Plot of C_p/T vs T^2 in zero field.

5.6 Phase Diagram of $Sr_3(Ru_{1-x}Mn_x)_2O_7$

Combining both results from the electrical and magnetic properties measurements, we obtain the doping (x) dependence of resistivity and magnetic susceptibility. Figure 5.40 shows the temperature dependences of ρ_{ab} (Fig. 5.40 a) and ρ_c (Fig. 5.40 b) with different x. Metallic-to-insulating crossover is observed in x = 0.06, 0.08, 0.16, 0.2 and 0.33. Both ρ_{ab} and ρ_c monotonically increase with increasing x. Temperature dependences of χ_{ab} and χ_c at different x are shown in Figure 5.41 (a) and (b), respectively. Figure 5.42 shows the resistivity anisotropy ρ_c/ρ_{ab} (left axis) and magnetic susceptibility anisotropy χ_c/χ_{ab} (right axis) as a function of x at 300 K. Both ρ_c/ρ_{ab} and χ_c/χ_{ab} tends to decrease with increasing x, which are consistent with the trend in ratio c/a (shown in Figure 4.3 (d)).

The Curie-Weiss law fitting results are shown in Figure 5.43 (a) and (b). The obtained Θ_{CW} and p_{eff} from the fitting for $Sr_3Ru_2O_7$ are Θ_{CW}^{ab} = -39 K (Θ_{CW}^{c} = -48 K) and p_{eff}^{ab} = 2.62 (p_{eff}^{c} =3.18) for H//ab (H//c). Upon doping Mn into $Sr_3Ru_2O_7$, both Θ_{CW}^{ab} and Θ_{CW}^{c} are negative and monotonically increase with x for $0 \leq x \leq 0.16$ and become positive in x = 0.2 for both field directions, as shown in Figure 5.43 (a). Above x = 0.2, Θ_{CW}^{ab} is positive and Θ_{CW}^{c} is negative, suggesting a mixed FM and AFM interactions in compounds with higher doping level. Derived from Curie constant, both p_{eff}^{ab} and p_{eff}^{c} do not change remarkably with doping above x = 0.2, as shown in Figure 5.43 (b), revealing a trace of saturation trend with increasing x. Figure 5.44 shows M versus H results of samples $0 \leq x \leq 0.16$ (a) and $0.2 \leq x \leq 0.7$ (b) at 2 K for H//ab. A metamagnetism occurs around at H = 5 T (H//ab) in crystal with x = 0, which is consistent with the previous report [40]. The M vs H results in $0 \leq x \leq 0.16$ (a) and $0.2 \leq x \leq 0.7$ (b) at 2 K for H//c are shown in Figure 5.45. Clear hysteresis loops are

observed in the data of crystals $0.2 \leq x \leq 0.7$ in both field orientations, indicating the existence of ferromagnetism in these samples.

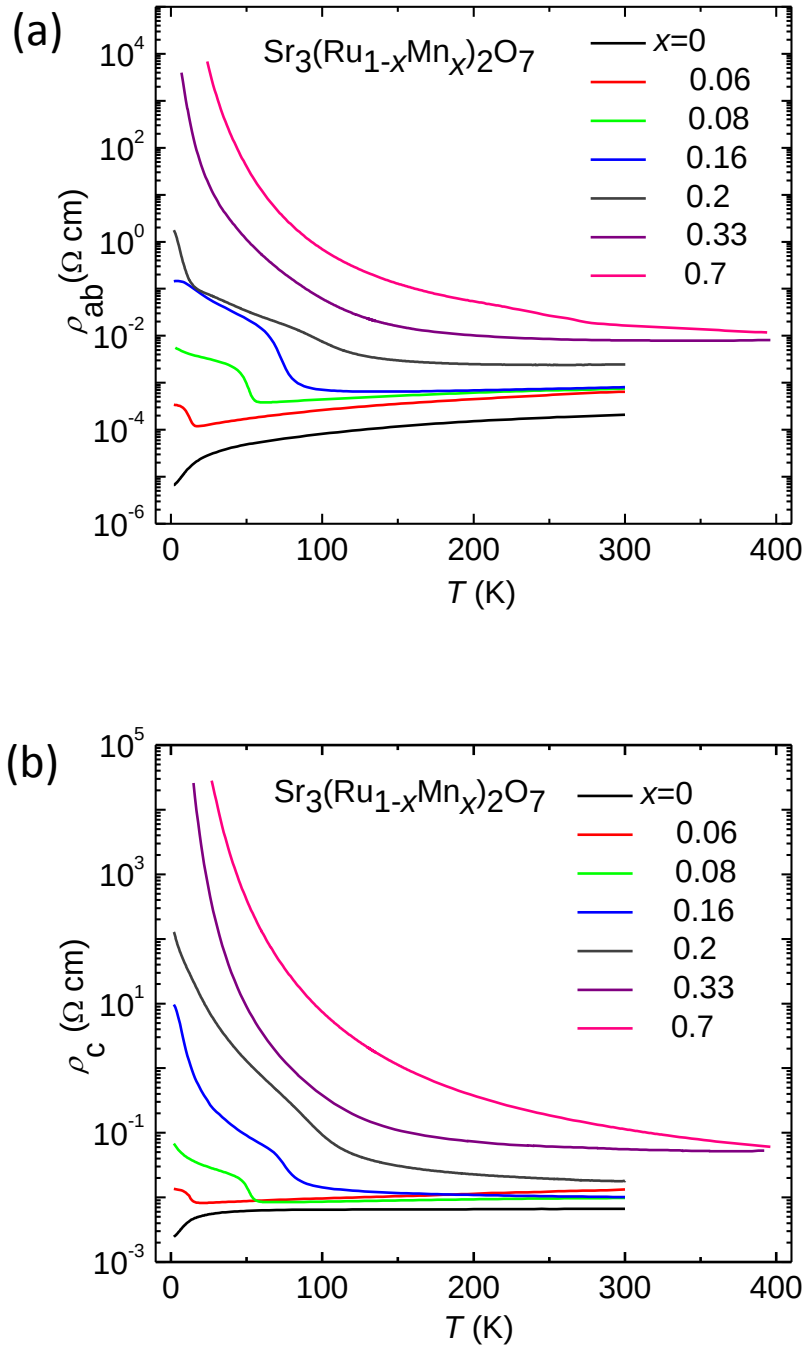

Figure 5.40 Temperature dependence of ρ_{ab} (a) and ρ_c (b) at different x.

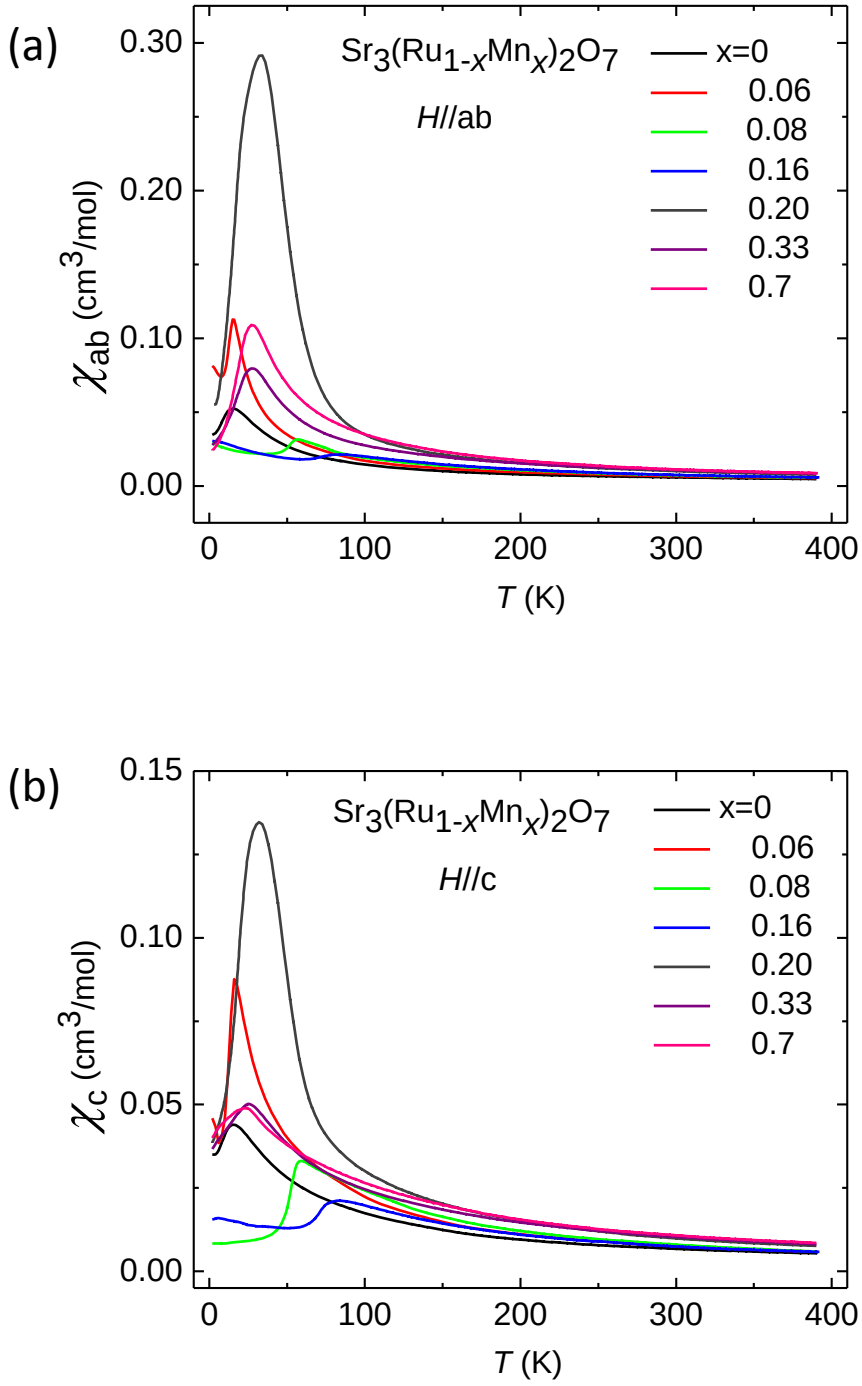

Figure 5.41 Temperature dependence of χ_{ab} (a) and χ_c (b) at different *x*.

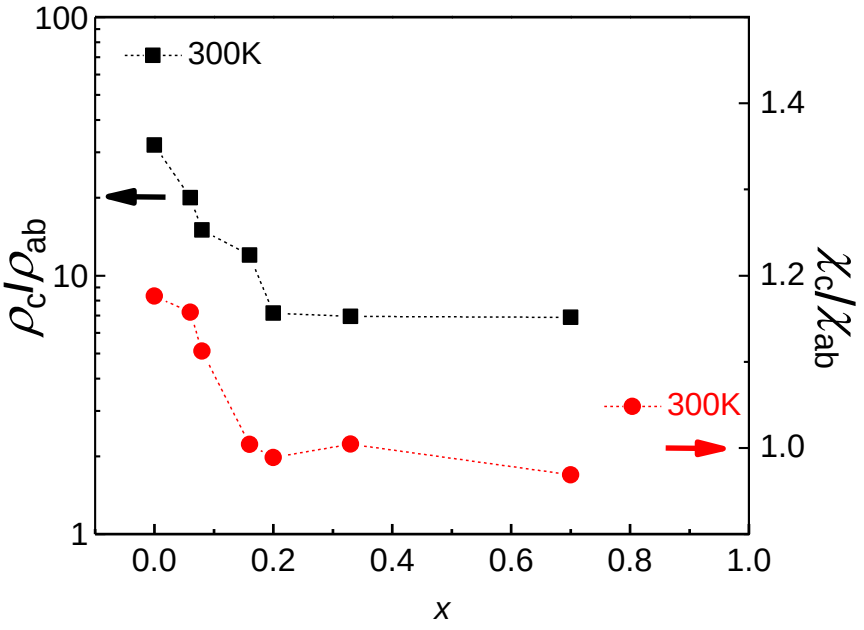

Figure 5.42 Resistivity anisotropy ρ_c/ρ_{ab} (left axis) and magnetic susceptibility anisotropy χ_c/χ_{ab} (right axis) as a function of x at 300 K.

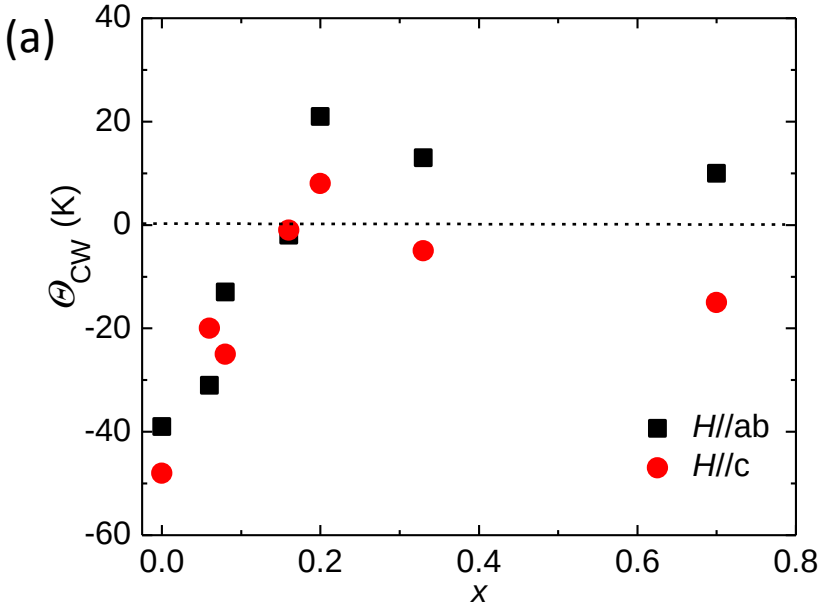

Figure 5.43 The x dependences of Θ_{CW} (a) and p_{eff} (b) for both H//ab and H//c.

fig. cont'd

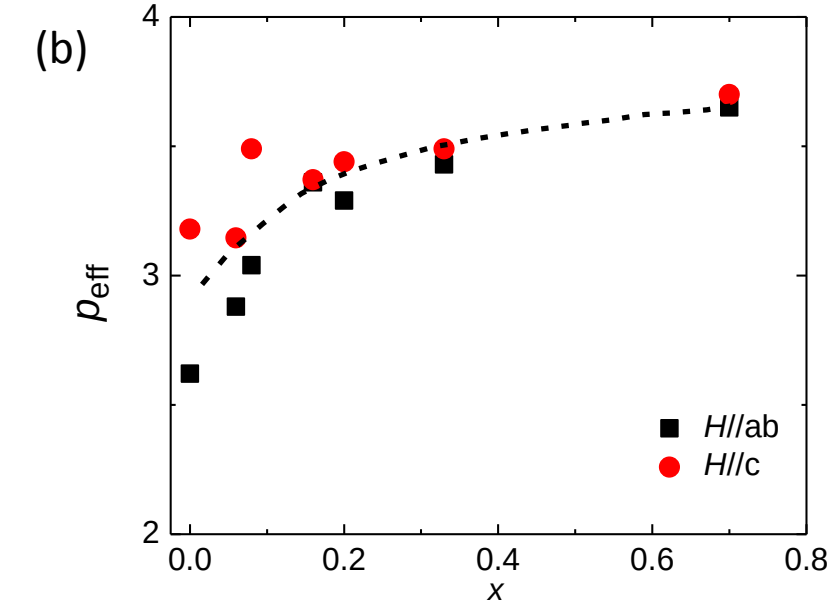

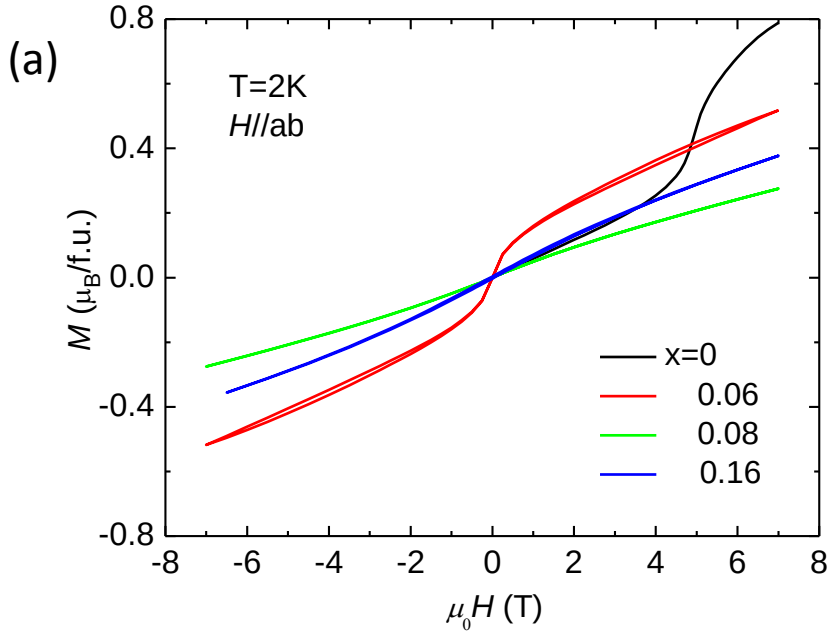

Figure 5.44 M versus H curves at 2 K for H//ab in $0 \leq x \leq 0.16$ (a) and $0.2 \leq x \leq 0.7$ (b). The f.u. represents per formula unit.

fig. cont'd

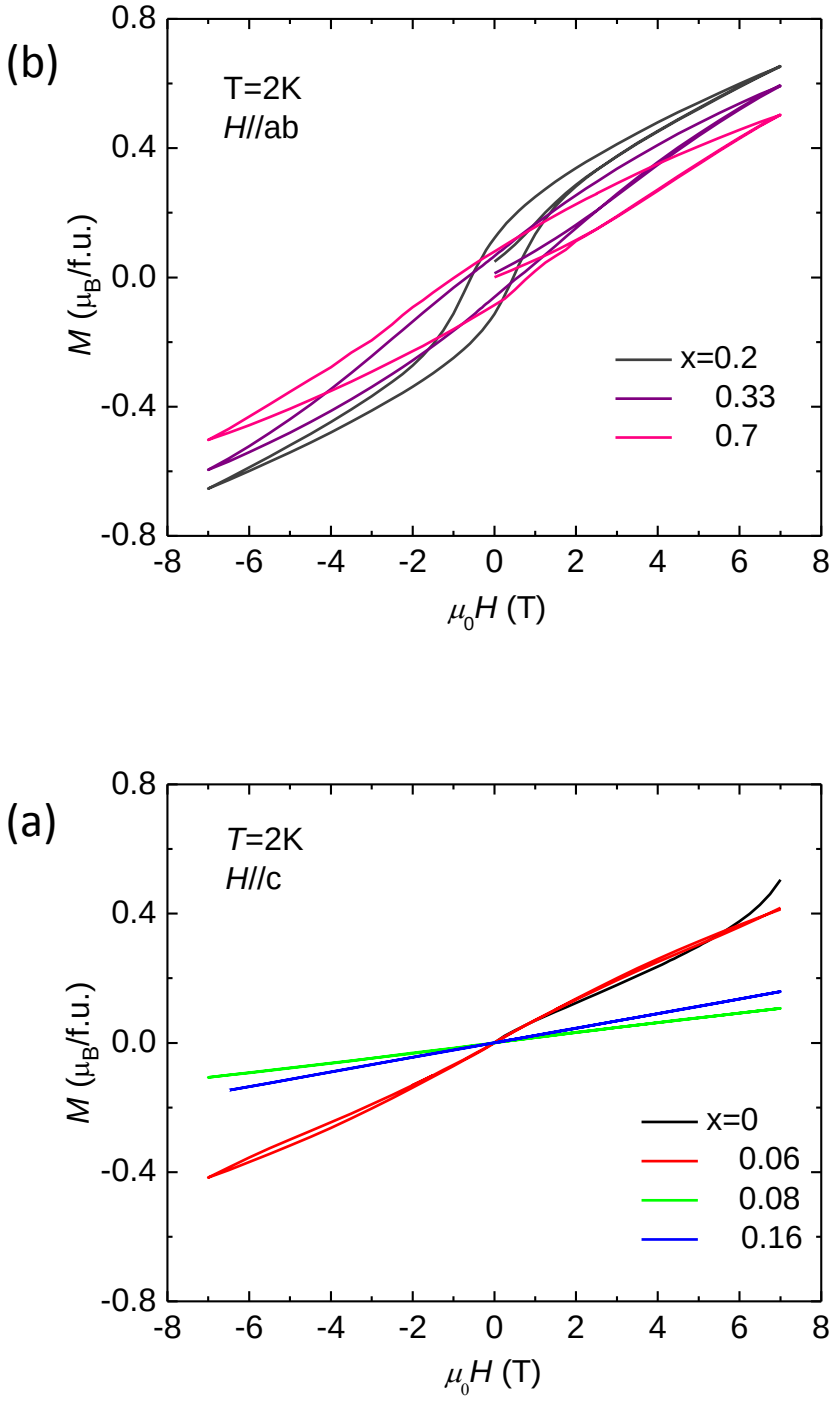

Figure 5.45 M versus H curves at 2 K for H//c in $0 \leq x \leq 0.16$ (a) and $0.2 \leq x \leq 0.7$ (b).

fig. cont'd

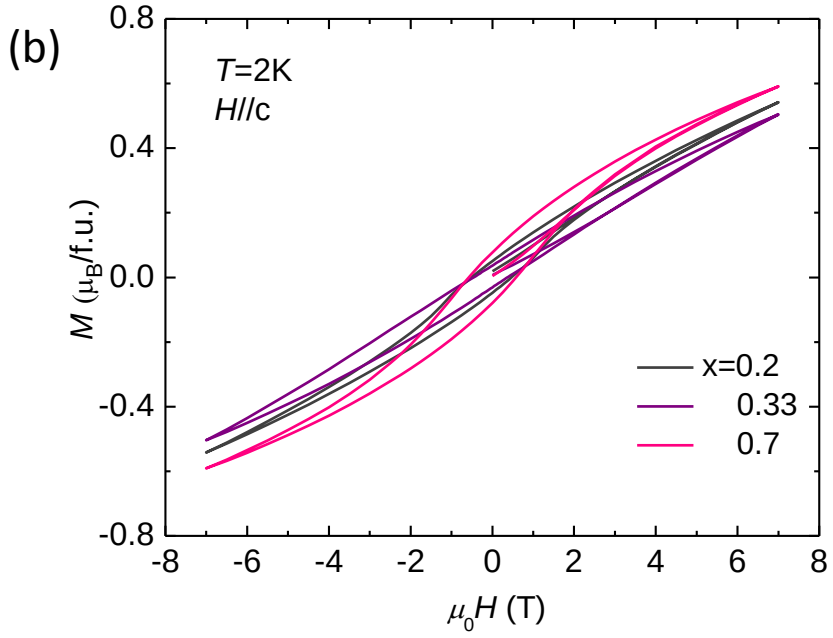

Now we plot resistivity, magnetic susceptibility and specific heat data of crystals with x = 0.08 and 0.16 together. As shown in Figure 5.46 (a) and (c), a specific heat anomaly exhibits exactly at T_M in crystal with x = 0.08, where T_{MIT} (inset of Figure 5.46 (c)) is close to T_M. Likewise, a specific heat anomaly exhibits at T_M in crystal with x = 0.16, where T_{MIT} is far away from T_M, as shown in Figure 5.46 (b) and (d) as well as the inset. Thus, we conclude that T_M in crystals with x = 0.08 and 0.16 corresponds to a true phase transition and T_{MIT} just corresponds to a metallic-to-insulating crossover instead of a true phase transition.

From the physical properties measurements we can construct a phase diagram covering the entire Mn content x range ($0 \leq x \leq 0.7$). Figure 5.47 shows the x-T phase diagram for $Sr_3(Ru_{1-x}Mn_x)_2O_7$, which is divided into five different regions. In the phase diagram, region I is a paramagnetic metallic (PM-M) phase. Region II is AFM-like correlation metallic (AFMC-M) phase. Region III is a paramagnetic insulating (PM-I) phase. Region IV is a long-range AFM insulating

(LR-AFM-I) phase. Region V is a short-range magnetic correlation insulating (SRMC-I) phase. $Sr_3Ru_2O_7$ remains metallic at all temperature range. No metallic-to-insulating crossover is observed in crystal with x = 0.7 up to 400 K. The T_M of $Sr_3Ru_2O_7$ is 16 K, which agrees with previous magnetic susceptibility measurement [38].

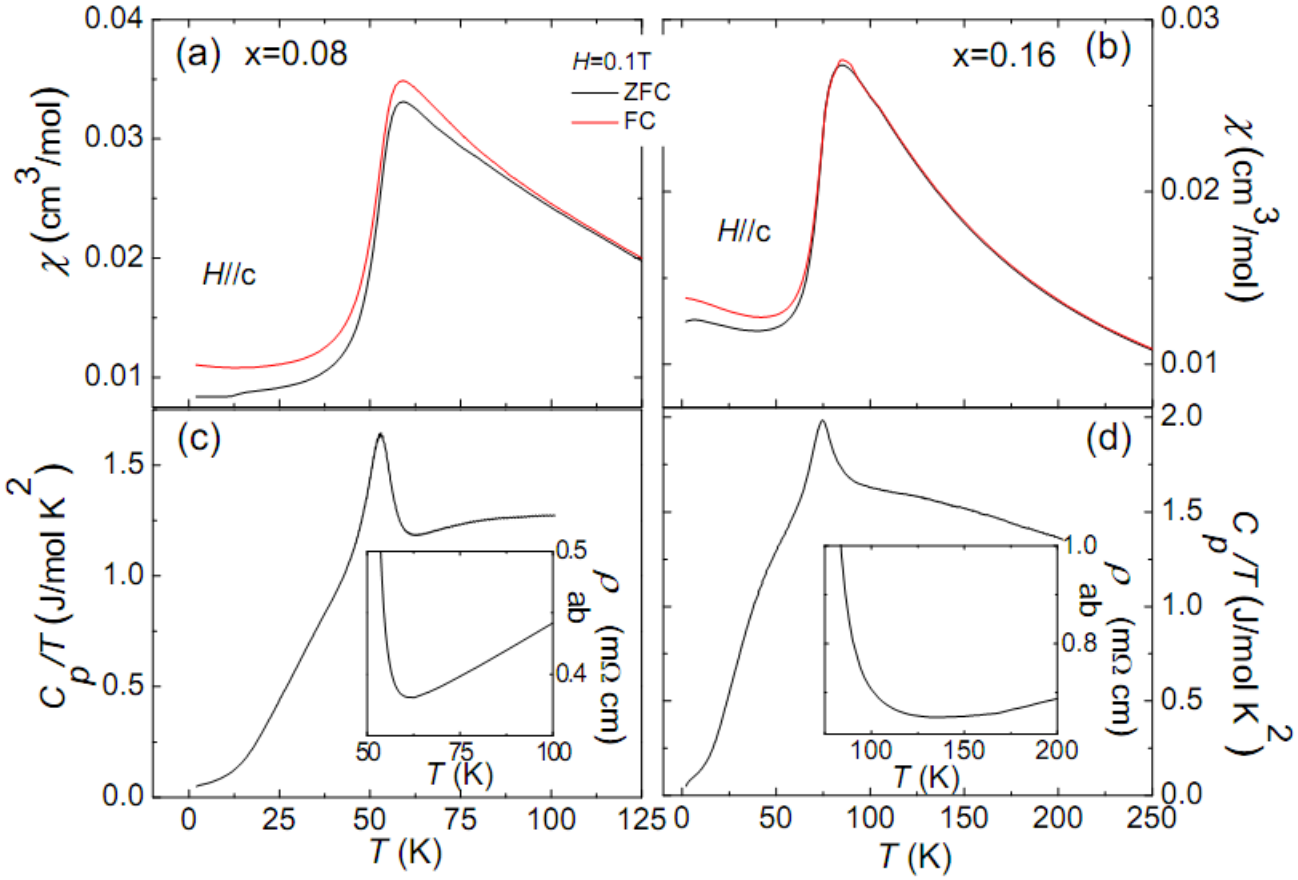

Figure 5.46 (a) and (b) are the temperature dependences of χ_c in crystals with x = 0.08 and 0.16, respectively. (c) and (d) are measured specific heat as a function of T in zero field for crystals with x = 0.08 and 0.16, respectively. Insets of (c) and (d) display the temperature dependences of ρ_{ab} around T_{MIT} in crystals x = 0.08 and 0.16, respectively.

5.7 Discussion

The structural, electrical and magnetic properties of $Sr_3(Ru_{1-x}Mn_x)_2O_7$ show intimate correlations. As shown in Figure 4.3, the lattice parameter a, c and ratio c/a as a function of x shows a turning point around x = 0.2. The rotation angle of RuO_6 decreases with increasing x, and equals to zero around x = 0.2 (Figure 4.4). The magnetic susceptibility and magnetization isotherm

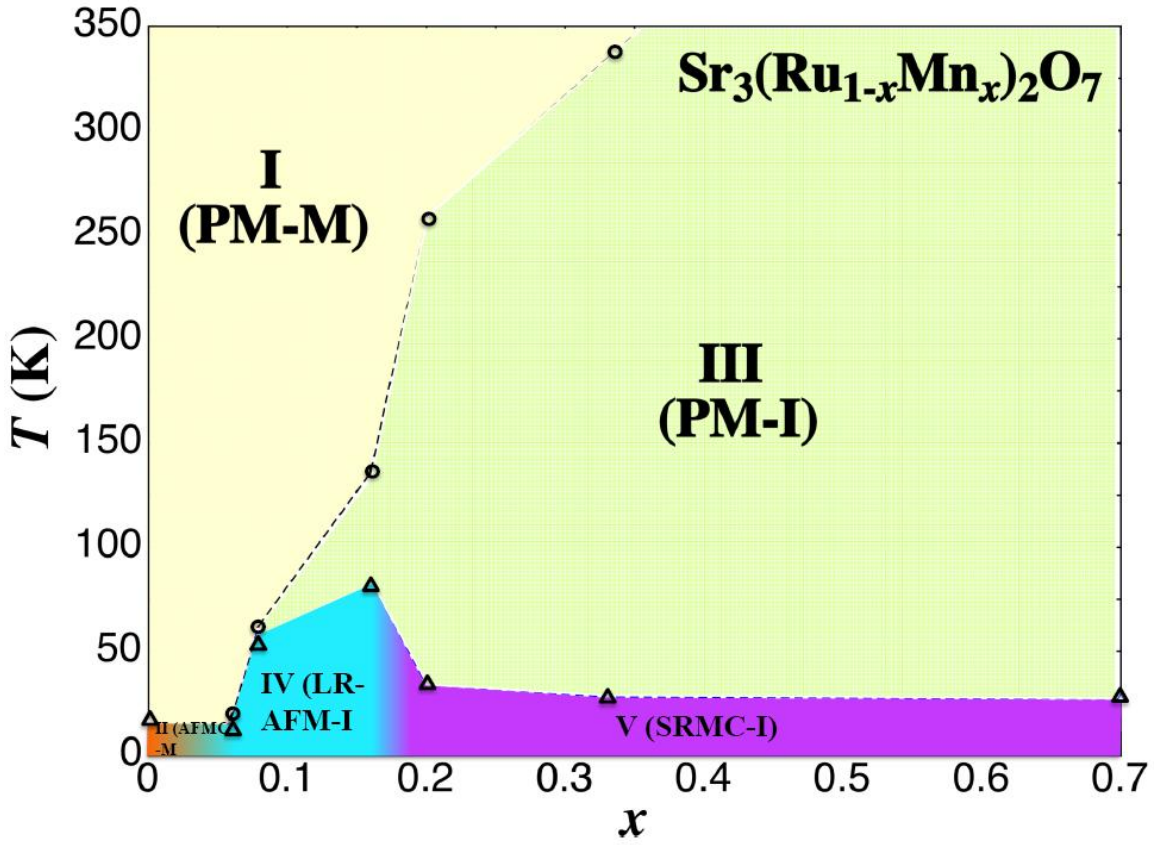

Figure 5.47 Phase diagram of $Sr_3(Ru_{1-x}Mn_x)_2O_7$ ($0 \leq x \leq 0.7$) with abbreviations. PM for paramagnetic, AFM for antiferromagnetic, MC for magnetic correlation, LR for long-range, SR for short-range, M for metallic phase, I for insulating phase. The open circle, and the open triangle represents the metallic-to-insulating crossover temperature T_{MIT}, and the peak temperature T_M of the susceptibility, respectively.

measurements also show clear different features below and above x = 0.2, as shown in Figure 5.43, 5.44 and 5.45. The x dependence of resistivity and magnetic susceptibility anisotropy of $Sr_3(Ru_{1-x}Mn_x)_2O_7$ at 300 K (Figure 5.42) shows a kink around x = 0.2, revealing a similar behavior with the ratio c/a varying as x (Figure 4.3 (d)). Furthermore, the specific heat anomalies are observed in crystals with x = 0.06, 0.08 and 0.16 around their T_M while no trace of anomaly is observed in crystals with x = 0.2, 0.33 and 0.7 around their T_M, as shown in Figure 5.48. It suggested that compounds with $x \geq 0.2$ show distinct features from compounds with $x < 0.2$. As shown in the phase diagram (Figure 5.47), T_{MIT} monotonically increases with increasing x while T_M shows a cusp at x = 0.16 and the difference between T_{MIT} and T_M becomes much larger above x = 0.2. The non-

monotonic behavior in T_M can be understood from the scenario that competing FM and AFM interactions always exist in the ground state of $Sr_3(Ru_{1-x}Mn_x)_2O_7$. Furthermore, the strong field dependences of T_{MIT} in crystals with x = 0.06 and 0.08 may suggest a scenario of electronic phase separation in such a correlated system, which needs further measurements in the future.

As shown in Figure 5.49, the Hall coefficient of crystals with x = 0.06 and 0.08 at lower temperature is approximately two or three orders of magnitude smaller than that of crystals with x = 0.16 and 0.2. Thus, the charge carrier concentration (derived from Hall coefficient R_H via $n = 1/(q \cdot R_H)$) for x = 0.16 and 0.2 is much smaller than that for x = 0.06 and 0.08, which is consistent with their high resistivity at lower temperature. In addition, R_H changes the sign for x = 0.16 around T_M (Inset of Figure 5.49 (b)). The charge carriers are dominated by holes below x = 0.16 and electrons in x = 0.2.

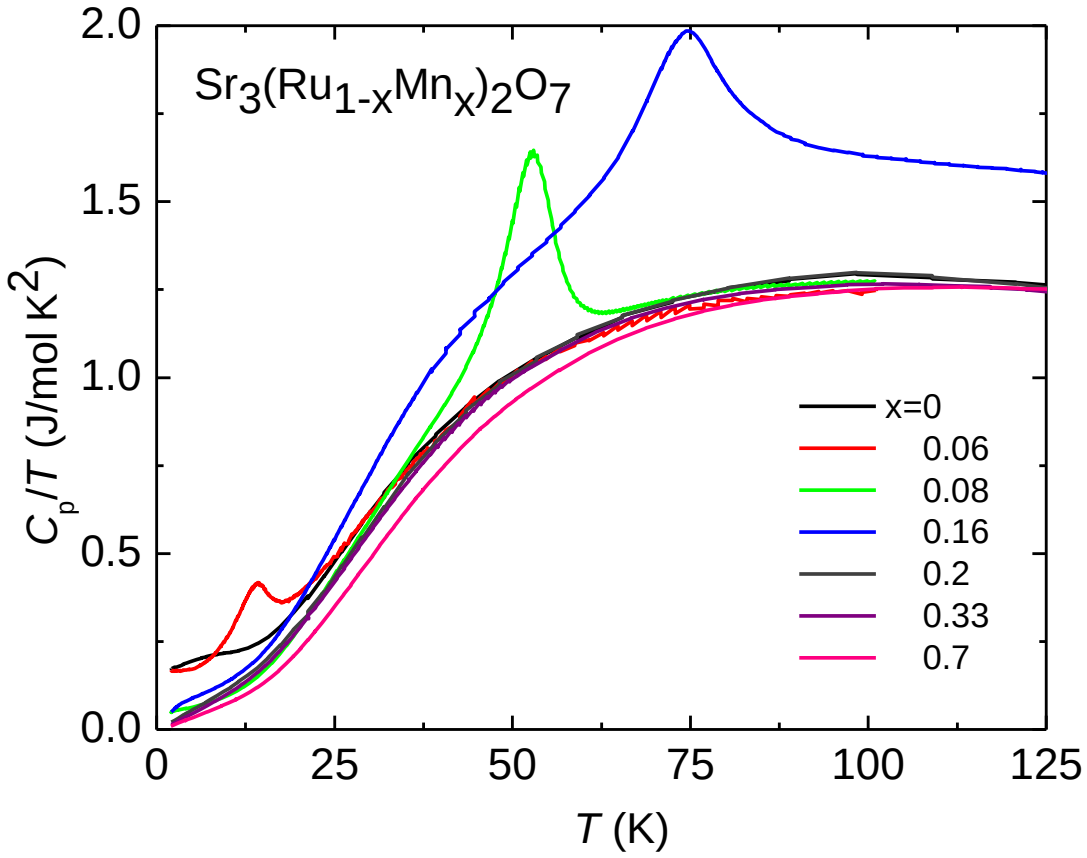

Figure 5.48 Plot of C_p/T vs T at different x.

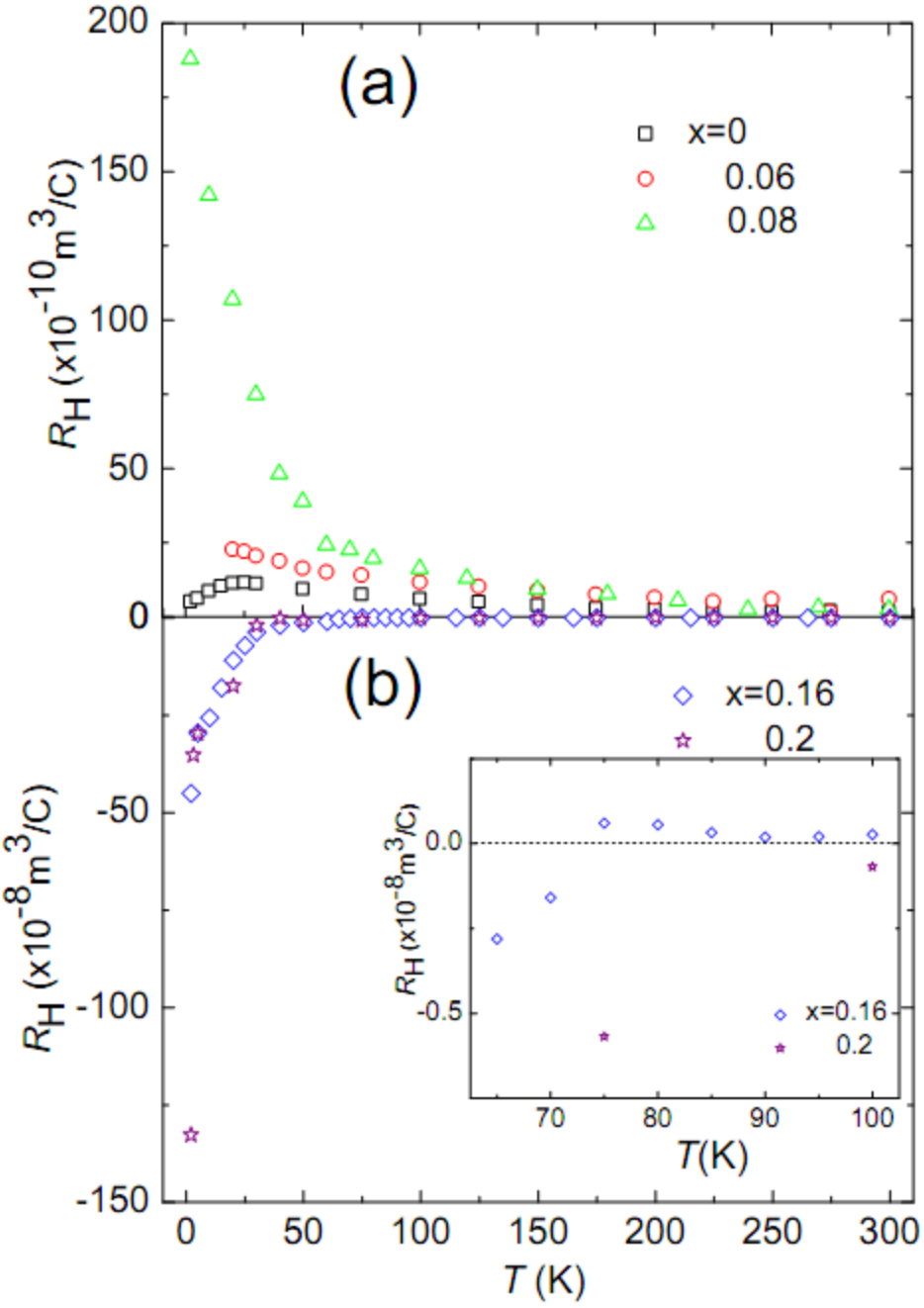

Figure 5.49 Hall coefficient of crystals with x = 0, 0.06, 0.08 (a) and x = 0.16, 0.2 (b). The inset is the enlarged plot of R_H versus T for x = 0.16, showing a sign change of R_H around T_M.

Chapter 6 Summary

The work of this dissertation sheds light on the understanding of complexity in Mn-doped $Sr_3Ru_2O_7$. High quality single crystals of $Sr_3(Ru_{1-x}Mn_x)_2O_7$ ($0 \leq x \leq 0.7$) are grown via the floating zone technique. A phase diagram of $Sr_3(Ru_{1-x}Mn_x)_2O_7$ is constructed, revealing rich phenomena in different regions. A metallic-to-insulating crossover at T_{MIT} and a susceptibility peak at T_M are determined from physical properties measurements. T_{MIT} monotonically increases with increasing x while T_M shows a cusp at $x = 0.16$ and the difference between T_{MIT} and T_M becomes much larger above $x = 0.2$. The bulk structure evolvement of $Sr_3(Ru_{1-x}Mn_x)_2O_7$ shows a turning point around $x = 0.2$ and there is no rotation of RuO_6 octahedra for $x \geq 0.2$. Correspondingly, their physical properties show distinct features below and above $x = 0.2$. Specific heat anomalies are observed in crystals with $x = 0.06$, 0.08 and 0.16 while no anomalies are observed for $x \geq 0.2$. Furthermore, the compounds for $x \geq 0.2$ show mixed FM and AFM interactions, different from those below $x = 0.2$.

The broken translational symmetry at the surface in layered TMOs may exhibit exotic behaviors. The surface structure of $Sr_3Ru_2O_7$ (001) shows different features from the bulk, revealing a tilt of RuO_6 and a rotation with a higher angle. The evolution of structural distortions at surface with x is a possible direction to lead us to understand complexities in strongly correlated system at low dimensionality.

References

[1] P. W. Anderson, *Science* **177**, 393 (1972)

[2] Y. Tokura and N. Nagaosa, *Science* **288**, 462 (2000)

[3] T. Z. Ward, Ph.D thesis, The University of Tennessee, 2008

[4] J. B. Goodenough, Localized to Itinerant Electronic Transition in Perovskite Oxides, Springer (2001)

[5] E. Dagotto, T. Hotta and A. Moreo, *Phys. Rep.* **344**, 1 (2001)

[6] Horst Köppel, David R. Yarkony, Heinz Barentzen**,** The Jahn-Teller-Effect: Fundamentals and Implications for Physics and Chemistry**,** Springer (2010)

[7] C. Zener, *Phys. Rev.* **81**, 440 (1951)

[8] C. Zener, *Phys. Rev.* **82**, 403 (1951)

[9] P. W. Anderson and H. Hasegawa, *Phys. Rev.* **100**, 675 (1955)

[10] M. B. Salamon and M. Jaime, *Rev. Mod. Phys.* **73**, 583 (2001)

[11] S. Jin *et al. Science* **264**, 413 (1994)

[12] Y. Tokura and Y. Tomioka *J. Magn. Magn. Mater.* **200**, 1 (1999)

[13] J. G. Bednorz *et al. Z. Phys. B: Condens. Matter.* **64**, 189 (1986)

[14] J. M. Tarascon *et al. Science* **235**, 1373 (1987)

[15] A. Moreo, S. Yunoki, and E. Dagotto, *Science* **283**, 2034 (1999)

[16] M. R. Ibarra, P. A. Algarabel, C. Marquina, J. Blasco, J. Garcia, *Phys. Rev. Lett.* **75**, 3541 (1995)

[17] H. Y. Hwang, S.-W. Cheong, P. G. Radaelli, M. Marezio, B. Batlogg, *Phys. Rev. Lett.* **75**, 914, (1995)

[18] P.Schiffer, A. P. Ramirez, W. Bao, S.-W. Cheong, *Phys. Rev. Lett.* **75**, 3336 (1995)

[19] A. Asamitsu, Y. Moritomo, Y. Tomioka, T. Arima, Y. Tokura, *Nature* **373**, 407 (1995)

[20] P. Dai, J. Zhang, H. A. Mook, S. -H. Liou, P. A. Dowben, E. W. Plummer, *Phys. Rev. B* **54**, R3694 (1996)

[21] S. J. L. Billinge, R. G. DoFrancesco, H. H. Kwei, J. J. Neumeier, J. D. Thompson, *Phys. Rev. Lett.* **77**, 715, (1996)

[22] P. G. Radaelli, D. E. Cox, M. Marezio, S.-W. Cheong, P. E. Schiffer, A. P. Ramirez, *Phys. Rev. Lett.* **75**, 4488 (1995)

[23] E. Dagotto, Nanoscale Phase Separation and Colossal Magnetoresistance, Springer-Verbag, Berlin, 2002

[24] M. Uehara, S. Mori, C. H. Chen, and S.-W. Cheong, *Nature* **399**, 560 (1999)

[25] P. L. Kuhns, *et al. Phys. Rev. Lett.* **91**, 127202 (2003)

[26] Tae-Hwan Kim, M. Angst, B. Hu, R. Jin, *X*.-G. Zhang, J. F. Wendelken, E. W. Plummer, and An-Ping Li, *Proceedings of National Academy of Sciences*, **107**, 5272-5275 (2010)

[27] S. N. Ruddlesden and P. Popper, *Acta. Cryst.* **10**, 538 (1957)

[28] S. N. Ruddlesden and P. Popper, *Acta. Cryst.* **11**, 54 (1958)

[29] A. P. Mackenzie *et al. Phys. Rev. Lett.* **80**, 161 (1998)

[30] Y. Maeno *et al. Phys. Today* **54**, 42 (2001)

[31] Y. Maeno, H. Hashimoto, K. Yoshida, S. Nishizaki, T. Fujita, J. G. Bednorz and F. Lichtenberg, *Nature* (London) **372**, 532 (1994)

[32] A. Damascelli *et al. Phys. Rev. Lett.* **85**, 5194 (2000)

[33] A. P. Mackenzie et al *Phys. Rev. Lett.* **76**, 3786 (1996)

[34] I. I. Mazin, D. J. Singh, *Phys. Rev. Lett.* **79**, 733 (1997)

[35] A. P. Mackenzie and Y. Maeno, *Rev. Mod. Phys.* **75**, 657 (2003)

[36] K. Ishida *et al. Nature* **396**, 658 (1998)

[37] G. M. Luke *et al. Nature* **394**, 558 (1998)

[38] S. Ikeda, Y. Maeno, S. Nakatsuji, M. Kosaka, Y. Uwatoko, *Phys. Rev. B* **62**, R6089 (2000)

[39] H. Müller-Buschbaum, J. Wilkens, *Z. Anorg. Allg. Chem.* **591**, 161 (1990)

[40] Q. Huang, J. W. Lynn, R. W. Erwin, J. Jarupatrakorn, R. J. Cava, *Phys. Rev. B* **58**, 8515 (1998)

[41] H. Shaked, J. D. Jorgensen, S. Short, O. Chmaissem, S. Ikeda, Y. Maeno, *Phys. Rev. B* **62**, 8725 (2000)

[42] R. Kiyanagi, K. Tsuda, N. Aso, H. Kimura, Y. Noda, Y. Yoshida, S. I. Ikeda, Y. Uwatoko, *J. Phys. Soc. Jpn.* **73**, 639 (2004)

[43] R. J. Cava *et al. J. Solid State Chem.* **116**, 141 (1995)

[44] M. B. Stone, M. D. Lumsden, R. Jin, B. C. Sales, D. Mandrus and S. E. Nagler, *Phys. Rev. B* **73**, 174426 (2006)

[45] L. Capogna *et al. Phys. Rev. B* **67**, 012504 (2003)

[46] R. S. Perry, L. M. Galvin, S. A. Grigera, L. Capogna, A. J. Schofield, A. P. Mackenzie, M. Chiao, S. R. Julian, S. I. Ikeda, S. Nakatsuji, Y. Maeno, C. Pfleiderer, *Phys. Rev. Lett.* **86**, 2661 (2001)

[47] G. Aeppli *et al. Science* **294**, 315 (2001)

[48] S. A. Grigera, R. S. Perry, A. J. Schofield, M. Chiao, S. R. Julian, G. G. Lonzarich, S. I. Ikeda, Y. Maeno, A. J. Millis, and A. P. Mackenize, *Science* **294**, 329 (2001)

[49] A. Tamai *et al. Phys. Rev. Lett.* **101**, 026407 (2008)

[50] A. G. Green *et al. Phys. Rev. Lett.* **95**, 086402 (2005)

[51] D. J. Singh and I. I. Mazin *Phys. Rev. B* **63**, 165101 (2001)

[52] M. K. Crawford, R. L. Harlow, W. Marshall, Z. Li, G. Gao, R. L. Lindstrom, Q. Huang, and J. W. Lynn, *Phys. Rev. B* **65**, 214412 (2002)

[53] G. Cao *et al. Phys. Rev. B* **68**, 174409 (2003)

[54] D. Fobes, M. H. Yu, M. Zhou, J. Hooper, C. J. O'Connor, M. Rosario, Z. Q. Mao, *Phys. Rev. B* **75**, 094429 (2007)

[55] D. Fobes *et al. Phys. Rev. B* **81**, 172402 (2010)

[56] Z. Q. Mao *et al. Phys. Rev. Lett.* **96**, 077205 (2006)

[57] A. Callaghan, C. W. Moller, and R. Ward, *Inorg. Chem.* **5**, 1572 (1966)

[58] P. B. Allen et al *Phys. Rev. B* **53**, 4393 (1996)

[59] R. G. Moore, Ph.D thesis, The University of Tennessee, 2006

[60] S. Nakatsuji, Y. Maeno, *Phys. Rev. Lett.* **84**, 2666 (2000)

[61] S. Nakatsuji, Y. Maeno, *Phys. Rev. Lett.* **90**, 137202 (2003)

[62] M. Braden, G. Andre, S. Nakatsuji and Y. Maeno, *Phys. Rev. B* **58**, 847 (1998)

[63] Z. Fang and K. Terakura, *Phys. Rev. B* **64**, 020509 (2001)

[64] K. Iwata *et al. J. Phys. Soc. Jpn* **77**, 104716 (2008)

[65] J. Peng *et al. Phys. Rev. B* **82**, 024417 (2010)

[66] G. Cao *et al. Phys. Rev. Lett.* **78**, 1751 (1997)

[67] E. Ohmichi *et al. Phys. Rev. B* **70**, 104414 (2004)

[68] Y. Yoshida *et al. Phys. Rev. B* **72**, 054412 (2005)

[69] J. Hooper *et al. Phys. Rev. B* **75**, 060403 (2007)

[70] P. Steffens *et al. Phys. Rev. B* **79**, 054422 (2009)

[71] R. Mathieu, A. Asamitsu, Y. Kaneko, J. P. He, X. Z. Yu, R. Kumai, Y. Onose, N. Takeshia, T. Arima, H. Takagi, and Y. Tokura, *Phys. Rev. B* **72**, 092404 (2005)

[72] M. A. Hossain, *et al Phys. Rev. Lett.* **101**, 016404 (2008)

[73] H. Z. Guo *et al. Phys. Rev. B* **81**, 155121 (2010)

[74] J. F. Mitchell *et al. J. Solid State Chem.* **141**, 599 (1998)

[75] I. Tanaka and H. Kojima, *Nature* **337**, 21 (1989)

[76] Z. Q. Mao *et al. Mater. Res. Bull.* **35**, 1813 (2000)

[77] http://people.seas.harvard.edu/~jones/es154/lectures/lecture_2/materials/materials.html

[78] N. Kikugawa *et al. J. Phys. Soc. Jpn.* **78**, 014701 (2009)

[79] G. M. Sheldrick, *Acta Crystallogr. Sect. A* **64**, 112 (2008).

[80] A. Altomare, M. C. Burla, M. Camalli, G. L. Cascarano, C. Giacovazzo, A. Guagliardi, A. G. G. Moliterni, G. Polidori, R. Spagna, *J. Appl. Crystallogr.* **32**, 115 (1999)

[81] L. J. Farrugia, *J. Appl. Crystallogr.* **32**, 837 (1999)

[82] A. L. Spek, *J. Appl. Crystallogr.* **36**, 7 (2003)

[83] M. A. Van Hove, W. H. Weinberg, and C.-M. Chan, Low-Energy Electron Diffraction Experiment, Theory, and Surface Structure Determination (Springer Verlag, Berlin, 1986)

[84] J. B. Pendry, *J. Phys. C* **13**, 937 (1980)

[85] V. B. Nascimento, R. G. Moore, J. Rundgren, Jiandi Zhang, Lei Cai, R. Jin, D. G. Mandus, E. W. Plummer, *Phys. Rev. B* **75**, 035408 (2007)

[86] J. Rundgren, *Phys. Rev. B* **68**, 125405 (2003)

[87] L. Landau, *Soviet Physics JETP* **3**, 920 (1957)

[88] L. Landau, *Soviet Physics JETP* **5**, 10 (1957)

[89] PPMS Manual, Quantum Design

[90] Jason Farrell, Ph.D thesis, University of St. Andrews, 2008

[91] J. W. Lynn (ed.) High Temperature Superconductivity. Springer-Verlag, New York 1990

[92] MPMS XL Manual, Quantum Design

[93] http://hyperphysics.phy-astr.gsu.edu/hbase/solids/squid.html

[94] J. L. Squires, Introduction to the Theory of Thermal Neutron Scattering, Dover Publications Inc., Mineola, New York (1978)

[95] http://neutrons.ornl.gov/instruments/HFIR/HB1A/

[96] G. Cao *et al. Phys. Rev. B* **68**, 174409 (2003)

[97] G. Cao *et al. Phys. Rev. B* **55**, 672 (1997)

[98] R. S. Perry and Y. Maeno, *J. Crystal Growth* **271**, 134 (2004)

[99] Jinho Lee *et al. Nature Physics* **5**, 800 (2009)

[100] K. Iwaya, S. Satow, T. Hanaguri, N. Shannon, Y. Yoshida, S. I. Ikeda, J. P. He, Y. Kaneko, Y. Tokura, T. Yamada, H. Takagi, *Phys. Rev. Lett.* **99**, 057208 (2007)

[101] R. G. Moore, V. B. Nascimento, Jiandi Zhang, J. Rundgren, R. Jin, D. Mandrus, and E. W. Plummer, *Phys. Rev. Lett.* **100**, 066102 (2008)

[102] R. G. Moore, Jiandi Zhang, V. B. Nascimento, R. Jin, Jiandong Guo, G. T. Wang, Z. Fang, D. Mandrus and E. W. Plummer, *Science* **318**, 615 (2007)

[103] R. Matzdorf, Ismail, T. Kimura, Y. Tokura, and E. W. Plummer, *Phys. Rev. B* **65**, 085404 (2002)

[104] R. S. Perry *et al. Physica B* **284-288**, 1469 (2000)

[105] Y. Liu *et al. Phys. Rev. B* **63**, 174435 (2001)

Appendix A: Bulk Crystal Structures of $Sr_3(Ru_{1-x}Mn_x)_2O_7$ (x = 0.06, 0.16, 0.2, 0.33 and 0.7)

Table A1 Crystallographic Parameters of Crystal with x = 0.06

Crystal data		
Temperature (K)	298(2)	90(2)
Formula	$Sr_3(Ru_{0.94}Mn_{0.06})_2O_7$	$Sr_3(Ru_{0.94}Mn_{0.06})_2O_7$
Crystal system	Tetragonal	Tetragonal
Space group	*I*4/*mmm* (No. 139)	*I*4/*mmm* (No. 139)
a (Å)	3.8951(5)	3.8778(5)
c (Å)	20.660(4)	20.733(4)
V (Å^3)	313.45(8)	311.77(8)
Mosaicity ( )	0.453(3)	0.460(3)
Z	2	2
2θ range ( )	8.0-59.98	7.8-60.2
μ (mm^{-1})	30.01	30.17
Data collection		
Measured reflections	482	480
Independent reflections	177	177
Reflections with $I>2\sigma(I)$	175	177
[a]R_{int}	0.017	0.021
H	-5→5	-5→5
k	-3→3	-3→3
l	-28→28	-28→28
Refinement		
Reflections	177	177
Parameters	22	22
[b]$R_1[F^2>2\sigma(F^2)]$	0.027	0.025
[c]$wR_2(F^2)$	0.057	0.058
[d]S	1.27	1.27
$\Delta\rho_{max}$ (eÅ^{-3})	1.12	1.24
$\Delta\rho_{min}$ (eÅ^{-3})	-2.90	-2.14

[a]$R_{int} = [\Sigma | F_o^2 - F_c^2 \text{ (mean)} | / (n\text{-}p)]^{1/2}$

[b]$R_1 = \Sigma | | F_o | - | F_c | | / \Sigma | F_o |$

[c]$wR_2 = [\Sigma [w(F_o^2 - F_c^2)^2] / \Sigma [w(F_o^2)^2]]^{1/2}$,
$w = 1 / [\sigma^2(F_o^2) + (0.0389P)^2 + 0.0000P]$ for 298 K,
$w = 1 / [\sigma^2(F_o^2) + (0.0365P)^2 + 0.4462P]$ for 90 K

[d]$S = [\Sigma [w(F_o^2 - F_c^2)^2] / \Sigma (n - p)]^{1/2}$

Table A2 Atomic Positions and Equivalent Isotropic Displacement Parameters of Crystal with x = 0.06

Atom	Wyckoff position	x	y	z	Occ.[a]	U_{eq} (Å^2)[b]
T = 298 K						
Sr1	2*b*	1/2	1/2	0	1	0.0094(3)
Sr2	4*e*	1/2	1/2	0.18593(4)	1	0.0089(3)
Mn1	4*e*	0	0	0.09739(3)	0.059 (6)	0.0046(3)
Ru1	4*e*	0	0	0.09739(3)	0.941(6)	0.0046(3)
O1	2*a*	0	0	0	1	0.013(1)
O2	4*e*	0	0	0.1955(3)	1	0.0110(9)
O3	8*g*	1/2	0.056(2)	0.0966(2)	0.50	0.014(2)
T = 90 K						
Sr1	2*b*	1/2	1/2	0	1	0.0047(3)
Sr2	4*e*	1/2	1/2	0.18635(4)	1	0.0046(3)
Mn1	4*e*	0	0	0.09740(3)	0.066(8)	0.0023(3)
Ru1	4*e*	0	0	0.09740(3)	0.934(8)	0.0023(3)
O1	2*a*	0	0	0	1	0.007(1)
O2	4*e*	0	0	0.1954(3)	1	0.0074(9)
O3	16*n*	1/2	0.066(1)	0.0966(1)	0.5	0.008(1)

[a] Occupancy of atoms

[b] U_{eq} is defined as one-third of the trace of the orthogonalized U^{ij} tensor.

Table A3 Anisotropic Atomic Displacement Parameters (Å^2) of Crystal with x = 0.06

Atom	U^{11}	U^{22}	U^{33}	U^{12}	U^{13}	U^{23}
T = 298 K						
Sr1	0.0095(3)	0.0095(3)	0.0092(5)	0.000	0.000	0.000
Sr2	0.0095(3)	0.0095(3)	0.0078(5)	0.000	0.000	0.000
Mn1	0.0045(3)	0.0045(3)	0.0047(4)	0.000	0.000	0.000
Ru1	0.0045(3)	0.0045(3)	0.0047(4)	0.000	0.000	0.000
O1	0.020(2)	0.020(2)	0.000(3)	0.000	0.000	0.000
O2	0.015(1)	0.015(1)	0.002(2)	0.000	0.000	0.000
O3	0.007(2)	0.018(5)	0.017(2)	0.000	0.000	0.000
T = 90 K						
Sr1	0.0046(3)	0.0046(3)	0.0049(5)	0.000	0.000	0.000
Sr2	0.0046(3)	0.0046(3)	0.0048(5)	0.000	0.000	0.000
Mn1	0.0021(3)	0.0021(3)	0.0026(4)	0.000	0.000	0.000
Ru1	0.0021(3)	0.0021(3)	0.0026(4)	0.000	0.000	0.000
O1	0.010(2)	0.010(2)	0.001(3)	0.000	0.000	0.000
O2	0.011(1)	0.011(1)	0.001(2)	0.000	0.000	0.000
O3	0.007(2)	0.009(4)	0.009(2)	-0.001(1)	0.000	0.000

Table A4 Selected Bond Distances (Å) and Angles (°) of Crystal with $x = 0.06$

	298K	90K
Distances		
Sr1-O1	2.7543(4)	2.7420(4)
Sr1-O3 (×4)	2.640(5)	2.615(4)
Sr2-O2	2.7613(5)	2.7484(5)
Sr2-O3 (×4)	2.530(5)	2.509(4)
Ru1-O1	2.0120(7)	2.0193(7)
Ru1-O2	2.026(5)	2.031(6)
Ru1-O3 (×4)	1.9598(9)	1.9559(7)
Angles		
O1-Ru1-O3 (×4)	89.49(9)	89.51(9)
O2-Ru1-O3 (×4)	90.51(9)	90.49(9)
Rotation		
[a]RuO_6 octahedra	6.4(2)	7.5(2)

[a] This value represents the rotational angle (Φ) for the RuO_6 octahedra. For a view of the rotational angles along the *ab*-plane, please see Figure 4.2(b).

Table A5 Crystallographic parameters of crystal with x = 0.16

Crystal data		
Temperature (K)	298(2)	90(2)
Formula	$Sr_3(Ru_{0.84}Mn_{0.16})_2O_7$	$Sr_3(Ru_{0.84}Mn_{0.16})_2O_7$
Crystal system	Tetragonal	Tetragonal
Space group	*I*4/*mmm* (No. 139)	*I*4/*mmm* (No. 139)
a (Å)	3.9107(10)	3.8987(15)
c (Å)	20.4561(55)	20.476(7)
V (Å^3)	312.85(15)	311.2(2)
Mosaicity ( )	0.534(6)	0.738(7)
Z	2	2
2θ range ( )	7.96-59.92	7.96-60.00
μ (mm^{-1})	29.985	30.141
Data collection		
Measured reflections	466	461
Independent reflections	176	176
Reflections with $I>2\sigma(I)$	161	155
[a]R_{int}	0.0622	0.0539
H	-5→5	-5→5
k	-3→3	-3→3
l	-28→27	-25→28
Refinement		
Reflections	176	176
Parameters	20	22
[b]$R_1[F^2>2\sigma(F^2)]$	0.0479	0.0406
[c]$wR_2(F^2)$	0.1088	0.1141
[d]S	1.178	1.131
$\Delta\rho_{max}$ (eÅ^{-3})	2.957	2.168
$\Delta\rho_{min}$ (eÅ^{-3})	-4.627	-3.690

[a]$R_{int} = [\Sigma | F_o^2 - F_c^2 \text{ (mean)} | / (n\text{-}p)]^{1/2}$

[b]$R_1 = \Sigma | | F_o | - | F_c | | / \Sigma | F_o |$

[c]$wR_2 = [\Sigma [w(F_o^2 - F_c^2)^2] / \Sigma [w(F_o^2)^2]]^{1/2}$,
$w = 1 / [\sigma^2(F_o^2) + (0.0692P)^2 + 0.0000P]$ for 298 K,
$w = 1 / [\sigma^2(F_o^2) + (0.0790P)^2 + 0.0000P]$ for 90 K

[d]$S = [\Sigma [w(F_o^2 - F_c^2)^2] / \Sigma (n - p)]^{1/2}$

Table A6 Atomic Positions and Equivalent Isotropic Displacement Parameters of crystal with x = 0.16

Atom	Wyckoff position	x	y	z	Occ.[a]	U_{eq} (Å^2)[b]
T = 298 K						
Sr1	2*b*	1/2	1/2	0	1	0.0086(6)
Sr2	4*e*	1/2	1/2	0.18507(8)	1	0.0080(5)
Mn1	4*e*	0	0	0.09741(6)	0.165(13)	0.0040(6)
Ru1	4*e*	0	0	0.09741(6)	0.835(13)	0.0040(6)
O1	2*a*	0	0	0	1	0.012(3)
O2	4*e*	0	0	0.1960(5)	1	0.011(2)
O3	8*g*	1/2	0	0.0969(3)	1	0.0191(17)
T = 90 K						
Sr1	2*b*	1/2	1/2	0	1	0.0059(6)
Sr2	4*e*	1/2	1/2	0.18508(8)	1	0.0054(6)
Mn1	4*e*	0	0	0.09726(6)	0.157(16)	0.0036(6)
Ru1	4*e*	0	0	0.09726(6)	0.843(16)	0.0036(6)
O1	2*a*	0	0	0	1	0.010(3)
O2	4*e*	0	0	0.1951(6)	1	0.011(2)
O3	16*n*	1/2	0.051(6)	0.0965(4)	0.5	0.006(5)

[a] Occupancy of atoms

[b] U_{eq} is defined as one-third of the trace of the orthogonalized U^{ij} tensor.

Table A7 Anisotropic Atomic Displacement Parameters (Å^2) of crystal with x = 0.16

Atom	U^{11}	U^{22}	U^{33}	U^{12}	U^{13}	U^{23}
T = 298 K						
Sr1	0.0091(6)	0.0091(6)	0.0075(11)	0.000	0.000	0.000
Sr2	0.0093(5)	0.0093(5)	0.0054(9)	0.000	0.000	0.000
Mn1	0.0042(6)	0.0042(6)	0.0036(8)	0.000	0.000	0.000
Ru1	0.0042(6)	0.0042(6)	0.0036(8)	0.000	0.000	0.000
O1	0.016(4)	0.016(4)	0.006(7)	0.000	0.000	0.000
O2	0.013(3)	0.013(3)	0.007(4)	0.000	0.000	0.000
O3	0.012(3)	0.032(4)	0.013(4)	0.000	0.000	0.000
T = 90 K						
Sr1	0.0064(7)	0.0064(7)	0.0050(11)	0.000	0.000	0.000
Sr2	0.0064(6)	0.0064(6)	0.0033(9)	0.000	0.000	0.000
Mn1	0.0042(7)	0.0042(7)	0.0025(8)	0.000	0.000	0.000
Ru1	0.0042(5)	0.0042(7)	0.0025(8)	0.000	0.000	0.000
O1	0.015(4)	0.015(4)	0.000(7)	0.000	0.000	0.000
O2	0.012(3)	0.012(3)	0.007(5)	0.000	0.000	0.000
O3	0.008(4)	0.007(15)	0.004(4)	-0.005(4)	0.000	0.000

Table A8 Selected Bond Distances (Å) and Angles ( ) of Crystal with $x = 0.16$

	298K	90K
Distances		
Sr1-O1	2.76504(14)	2.7570(2)
Sr1-O3 (×4)	2.784(5)	2.641(17)
Sr2-O2	2.433(11)	2.7646(9)
Sr2-O3 (×4)	2.661(5)	2.811(19)
Ru1-O1	1.9926(12)	1.9915(13)
Ru1-O2	2.016(11)	2.004(12)
Ru1-O3 (×4)	1.95538(11)	1.960(2)
Angles		
O1-Ru1-O3 (×4)	89.7(2)	89.6(3)
O2-Ru1-O3 (×4)	90.3(2)	90.4(3)
Rotation		
[a]RuO_6 octahedra	n/a	5.8(7)

[a] This value represents the rotational angle (Φ) for the RuO_6 octahedra. For a view of the rotational angles along the *ab*-plane, please see Figure 4.2(b).

Table A9 Crystallographic Parameters of Crystal with $x = 0.2$

Crystal data		
Temperature (K)	298(2)	90(2)
Formula	$Sr_3(Ru_{0.80}Mn_{0.20})_2O_7$	$Sr_3(Ru_{0.80}Mn_{0.20})_2O_7$
Crystal system	Tetragonal	Tetragonal
Space group	*I*4/*mmm* (No. 139)	*I*4/*mmm* (No. 139)
a (Å)	3.9159(10)	3.9049(10)
c (Å)	20.366(7)	20.365(8)
V (Å^3)	312.30(15)	310.52(15)
Mosaicity ( )	0.503(5)	0.536(5)
Z	2	2
2θ range ( )	8.00-59.98	8.00-59.70
μ (mm^{-1})	30.007	30.179
Data collection		
Measured reflections	461	439
Independent reflections	176	175
Reflections with $I>2\sigma(I)$	160	155
[a]R_{int}	0.0325	0.0332
H	-5→5	-5→5
k	-3→3	-3→3
l	-28→24	-24→28
Refinement		
Reflections	176	175
Parameters	20	20
[b]$R_1[F^2>2\sigma(F^2)]$	0.0359	0.0329
[c]$wR_2(F^2)$	0.0934	0.0713
[d]S	1.221	1.098
$\Delta\rho_{max}$ (eÅ^{-3})	3.503	2.591
$\Delta\rho_{min}$ (eÅ^{-3})	-2.606	-2.559

[a]$R_{int} = [\Sigma | F_o^2 - F_c^2 \text{ (mean)} | / (n\text{-}p)]^{1/2}$

[b]$R_1 = \Sigma | | F_o | - | F_c | | / \Sigma | F_o |$

[c]$wR_2 = [\Sigma [w(F_o^2 - F_c^2)^2] / \Sigma [w(F_o^2)^2]]^{1/2}$,
$w = 1 / [\sigma^2(F_o^2) + (0.0582P)^2 + 0.6662P]$ for 298 K,
$w = 1 / [\sigma^2(F_o^2) + (0.0477P)^2 + 0.0000P]$ for 90 K

[d]$S = [\Sigma [w(F_o^2 - F_c^2)^2] / \Sigma (n - p)]^{1/2}$

Table A10 Atomic Positions and Equivalent Isotropic Displacement Parameters of Crystal with x = 0.2

Atom	Wyckoff position	x	y	z	Occ.[a]	U_{eq} (Å^2)[b]
T = 298 K						
Sr1	2*b*	1/2	1/2	0	1	0.0090(5)
Sr2	4*e*	1/2	1/2	0.18486(7)	1	0.0084(5)
Mn1	4*e*	0	0	0.09747(5)	0.202(13)	0.0039(5)
Ru1	4*e*	0	0	0.09747(3)	0.798(13)	0.0039(5)
O1	2*a*	0	0	0	1	0.014(3)
O2	4*e*	0	0	0.1955(4)	1	0.0107(17)
O3	8*g*	1/2	0	0.0965(3)	1	0.0156(14)
T = 90 K						
Sr1	2*b*	1/2	1/2	0	1	0.0045(4)
Sr2	4*e*	1/2	1/2	0.18493(6)	1	0.0042(4)
Mn1	4*e*	0	0	0.09746(4)	0.203(10)	0.0019(4)
Ru1	4*e*	0	0	0.09746(4)	0.797(10)	0.0019(4)
O1	2*a*	0	0	0	1	0.006(2)
O2	4*e*	0	0	0.1950(4)	1	0.0091(16)
O3	8*g*	1/2	0	0.0960(2)	1	0.0130(12)

[a] Occupancy of atoms
[b] U_{eq} is defined as one-third of the trace of the orthogonalized U^{ij} tensor.

Table A11 Anisotropic Atomic Displacement Parameters (Å^2) of Crystal with x = 0.2

Atom	U^{11}	U^{22}	U^{33}	U^{12}	U^{13}	U^{23}
T = 298 K						
Sr1	0.0083(6)	0.0083(6)	0.0106(9)	0.000	0.000	0.000
Sr2	0.0077(5)	0.0077(5)	0.0099(8)	0.000	0.000	0.000
Mn1	0.0030(5)	0.0030(5)	0.0055(7)	0.000	0.000	0.000
Ru1	0.0030(5)	0.0030(5)	0.0055(7)	0.000	0.000	0.000
O1	0.021(4)	0.021(4)	0.000(5)	0.000	0.000	0.000
O2	0.016(3)	0.016(3)	0.000(3)	0.000	0.000	0.000
O3	0.004(3)	0.024(3)	0.018(4)	0.000	0.000	0.000
T = 90 K						
Sr1	0.0034(4)	0.0034(4)	0.0067(8)	0.000	0.000	0.000
Sr2	0.0028(4)	0.0028(4)	0.0068(6)	0.000	0.000	0.000
Mn1	0.0040(4)	0.0040(4)	0.0049(6)	0.000	0.000	0.000
Ru1	0.0040(4)	0.0040(4)	0.0049(6)	0.000	0.000	0.000
O1	0.010(3)	0.010(3)	0.000(5)	0.000	0.000	0.000
O2	0.009(2)	0.009(2)	0.008(4)	0.000	0.000	0.000
O3	0.002(2)	0.026(3)	0.011(3)	0.000	0.000	0.000

Table A12 Selected Bond Distances (Å) and Angles (°) of Crystal with x = 0.2

	298K	90K
Distances		
Sr1-O1	2.7690(7)	2.7612(7)
Sr1-O3 (×4)	2.774(5)	2.762(3)
Sr2-O2	2.436(9)	2.444(8)
Sr2-O3 (×4)	2.659(4)	2.664(3)
Ru1-O1	1.9850(13)	1.9847(11)
Ru1-O2	1.997(9)	1.987(8)
Ru1-O3 (×4)	1.9580(5)	1.9527(5)
Angles		
O1-Ru1-O3 (×4)	89.4(2)	89.10(15)
O2-Ru1-O3 (×4)	90.6(2)	90.90(15)
Rotation		
[a]RuO_6 octahedra	n/a	n/a

[a] This value represents the rotational angle (Φ) for the RuO_6 octahedra. For a view of the rotational angles along the *ab*-plane, please see Figure 4.2(b).

Table A13 Crystallographic Parameters of Crystal with $x = 0.33$

Crystal data		
Temperature (K)	298(2)	90(2)
Formula	$Sr_3(Ru_{0.67}Mn_{0.33})_2O_7$	$Sr_3(Ru_{0.67}Mn_{0.33})_2O_7$
Crystal system	Tetragonal	Tetragonal
Space group	*I*4/*mmm* (No. 139)	*I*4/*mmm* (No. 139)
a (Å)	3.9137(15)	3.9041(10)
c (Å)	20.271(7)	20.252(6)
V (Å^3)	310.5(2)	308.68(15)
Mosaicity ( )	0.410(5)	0.573(5)
Z	2	2
2θ range ( )	8.04-59.72	8.04-59.86
μ (mm^{-1})	30.074	30.257
Data collection		
Measured reflections	476	438
Independent reflections	175	175
Reflections with $I>2\sigma(I)$	159	164
[a]R_{int}	0.0473	0.0371
H	-5→5	-5→5
k	-3→3	-3→3
l	-27→28	-22→28
Refinement		
Reflections	175	175
Parameters	20	20
[b]$R_1[F^2>2\sigma(F^2)]$	0.0347	0.0310
[c]$wR_2(F^2)$	0.1052	0.0877
[d]S	1.156	1.215
$\Delta\rho_{max}$ (eÅ^{-3})	2.121	1.996
$\Delta\rho_{min}$ (eÅ^{-3})	-1.438	-1.395

[a]$R_{int} = [\Sigma | F_o^2 - F_c^2 \text{ (mean)} | / (n\text{-}p)]^{1/2}$

[b]$R_1 = \Sigma | | F_o | - | F_c | | / \Sigma | F_o |$

[c]$wR_2 = [\Sigma [w(F_o^2 - F_c^2)^2] / \Sigma [w(F_o^2)^2]]^{1/2}$,
$w = 1 / [\sigma^2(F_o^2) + (0.0687P)^2 + 0.0000P]$ for 298 K,
$w = 1 / [\sigma^2(F_o^2) + (0.0568P)^2 + 0.3702P]$ for 90 K

[d]$S = [\Sigma [w(F_o^2 - F_c^2)^2] / \Sigma (n - p)]^{1/2}$

Table A14 Atomic Positions and Equivalent Isotropic Displacement Parameters of Crystal with x = 0.33

Atom	Wyckoff position	x	y	z	Occ.[a]	U_{eq} (Å^2)[b]
T = 298 K						
Sr1	2*b*	1/2	1/2	0	1	0.0110(6)
Sr2	4*e*	1/2	1/2	0.18428(8)	1	0.0098(5)
Mn1	4*e*	0	0	0.09730(7)	0.332(11)	0.0054(5)
Ru1	4*e*	0	0	0.09730(7)	0.668(11)	0.0054(5)
O1	2*a*	0	0	0	1	0.013(3)
O2	4*e*	0	0	0.1953(5)	1	0.0118(19)
O3	8*g*	1/2	0	0.0967(3)	1	0.0131(15)
T = 90 K						
Sr1	2*b*	1/2	1/2	0	1	0.0060(5)
Sr2	4*e*	1/2	1/2	0.18423(6)	1	0.0049(4)
Mn1	4*e*	0	0	0.09739(6)	0.331(9)	0.0028(5)
Ru1	4*e*	0	0	0.09739(6)	0.669(9)	0.0028(5)
O1	2*a*	0	0	0	1	0.008(2)
O2	4*e*	0	0	0.1958(4)	1	0.0074(15)
O3	8*g*	1/2	0	0.0965(3)	1	0.0085(12)

[a] Occupancy of atoms

[b] U_{eq} is defined as one-third of the trace of the orthogonalized U^{ij} tensor.

Table A15 Anisotropic Atomic Displacement Parameters (Å^2) of Crystal with x = 0.33

Atom	U^{11}	U^{22}	U^{33}	U^{12}	U^{13}	U^{23}
T = 298 K						
Sr1	0.0118(6)	0.0118(6)	0.0093(11)	0.000	0.000	0.000
Sr2	0.0113(5)	0.0113(5)	0.0068(9)	0.000	0.000	0.000
Mn1	0.0055(6)	0.0055(6)	0.0052(8)	0.000	0.000	0.000
Ru1	0.0055(6)	0.0055(6)	0.0052(8)	0.000	0.000	0.000
O1	0.014(4)	0.014(4)	0.012(8)	0.000	0.000	0.000
O2	0.014(3)	0.014(3)	0.008(5)	0.000	0.000	0.000
O3	0.015(3)	0.010(3)	0.014(4)	0.000	0.000	0.000
T = 90 K						
Sr1	0.0068(5)	0.0068(5)	0.0043(8)	0.000	0.000	0.000
Sr2	0.0058(4)	0.0058(4)	0.0031(7)	0.000	0.000	0.000
Mn1	0.0032(5)	0.0032(5)	0.0020(6)	0.000	0.000	0.000
Ru1	0.0032(5)	0.0032(5)	0.0020(6)	0.000	0.000	0.000
O1	0.008(3)	0.008(3)	0.007(6)	0.000	0.000	0.000
O2	0.009(2)	0.009(2)	0.005(4)	0.000	0.000	0.000
O3	0.008(3)	0.008(3)	0.009(3)	0.000	0.000	0.000

Table A16 Selected Bond Distances (Å) and Angles (°) of Crystal with x = 0.33

	298K	90K
Distances		
Sr1-O1	2.7676(2)	2.7606(7)
Sr1-O3 (×4)	2.769(5)	2.762(4)
Sr2-O2	2.441(11)	2.429(9)
Sr2-O3 (×4)	2.643(5)	2.640(4)
Ru1-O1	1.9723(14)	1.9723(13)
Ru1-O2	1.987(11)	1.994(8)
Ru1-O3 (×4)	1.95704(16)	1.9521(5)
Angles		
O1-Ru1-O3 (×4)	89.6(2)	89.46(17)
O2-Ru1-O3 (×4)	90.4(2)	90.54(17)
Rotation		
[a]RuO_6 octahedra	n/a	n/a

[a] This value represents the rotational angle (Φ) for the RuO_6 octahedra. For a view of the rotational angles along the *ab*-plane, please see Figure 4.2(b).

Table A17 Crystallographic Parameters of Crystal with $x = 0.7$

Crystal data		
Temperature (K)	298(2)	90(2)
Formula	$Sr_3(Ru_{0.70}Mn_{0.30})_2O_7$	$Sr_3(Ru_{0.70}Mn_{0.30})_2O_7$
Crystal system	Tetragonal	Tetragonal
Space group	*I*4/*mmm* (No. 139)	*I*4/*mmm* (No. 139)
a (Å)	3.8950(15)	3.8891(10)
c (Å)	20.0960(60)	20.064(6)
V (Å^3)	304.88(20)	303.46(15)
Mosaicity ( )	0.794(6)	0.950(5)
Z	2	2
2θ range ( )	8.12-59.90	8.12-60.00
μ (mm^{-1})	30.311	30.488
Data collection		
Measured reflections	1402	472
Independent reflections	173	174
Reflections with $I>2\sigma(I)$	166	166
[a]R_{int}	0.1222	0.0544
H	-5→5	-5→5
k	-5→4	-3→3
l	-28→28	-28→28
Refinement		
Reflections	173	174
Parameters	20	20
[b]$R_1[F^2>2\sigma(F^2)]$	0.0538	0.0483
[c]$wR_2(F^2)$	0.1414	0.1429
[d]S	1.136	1.167
$\Delta\rho_{max}$ (eÅ^{-3})	4.165	2.321
$\Delta\rho_{min}$ (eÅ^{-3})	-2.256	-2.005

[a]$R_{int} = [\Sigma | F_o^2 - F_c^2 \text{ (mean)} | / (n\text{-}p)]^{1/2}$

[b]$R_1 = \Sigma | | F_o | - | F_c | | / \Sigma | F_o |$

[c]$wR_2 = [\Sigma [w(F_o^2 - F_c^2)^2] / \Sigma [w(F_o^2)^2]]^{1/2}$,
$w = 1 / [\sigma^2(F_o^2) + (0.1112P)^2 + 0.0000P]$ for 298 K,
$w = 1 / [\sigma^2(F_o^2) + (0.1093P)^2 + 0.0000P]$ for 90 K

[d]$S = [\Sigma [w(F_o^2 - F_c^2)^2] / \Sigma (n - p)]^{1/2}$

Table A18 Atomic Positions and Equivalent Isotropic Displacement Parameters of Crystal with x = 0.7

Atom	Wyckoff position	x	y	z	Occ.[a]	U_{eq} (Å^2)[b]
T = 298 K						
Sr1	2*b*	1/2	1/2	0	1	0.0112(7)
Sr2	4*e*	1/2	1/2	0.18345(6)	1	0.0100(6)
Mn1	4*e*	0	0	0.09717(9)	0.726(16)	0.0035(9)
Ru1	4*e*	0	0	0.09717(9)	0.274(16)	0.0035(9)
O1	2*a*	0	0	0	1	0.011(3)
O2	4*e*	0	0	0.1935(6)	1	0.0112(17)
O3	8*g*	1/2	0	0.0961(3)	1	0.0079(13)
T = 90 K						
Sr1	2*b*	1/2	1/2	0	1	0.0067(7)
Sr2	4*e*	1/2	1/2	0.18340(7)	1	0.0062(6)
Mn1	4*e*	0	0	0.09705(9)	0.678(17)	0.0030(9)
Ru1	4*e*	0	0	0.09705(9)	0.322(17)	0.0030(9)
O1	2*a*	0	0	0	1	0.007(3)
O2	4*e*	0	0	0.1942(7)	1	0.0073(17)
O3	8*g*	1/2	0	0.0959(3)	1	0.0057(14)

[a] Occupancy of atoms

[b] U_{eq} is defined as one-third of the trace of the orthogonalized U^{ij} tensor.

Table A19 Anisotropic Atomic Displacement Parameters (Å^2) of Crystal with x = 0.7

Atom	U^{11}	U^{22}	U^{33}	U^{12}	U^{13}	U^{23}
T = 298 K						
Sr1	0.0134(8)	0.0134(8)	0.0067(11)	0.000	0.000	0.000
Sr2	0.0121(5)	0.0121(7)	0.0057(9)	0.000	0.000	0.000
Mn1	0.0044(10)	0.0044(10)	0.0018(11)	0.000	0.000	0.000
Ru1	0.0044(10)	0.0044(10)	0.0018(11)	0.000	0.000	0.000
O1	0.014(4)	0.014(4)	0.005(5)	0.000	0.000	0.000
O2	0.015(3)	0.015(3)	0.004(3)	0.000	0.000	0.000
O3	0.005(3)	0.010(3)	0.009(2)	0.000	0.000	0.000
T = 90 K						
Sr1	0.0085(7)	0.0085(7)	0.0031(12)	0.000	0.000	0.000
Sr2	0.0077(7)	0.0077(7)	0.0032(10)	0.000	0.000	0.000
Mn1	0.0039(10)	0.0039(10)	0.0012(12)	0.000	0.000	0.000
Ru1	0.0039(10)	0.0039(10)	0.0012(12)	0.000	0.000	0.000
O1	0.008(4)	0.008(4)	0.006(6)	0.000	0.000	0.000
O2	0.008(3)	0.008(3)	0.006(4)	0.000	0.000	0.000
O3	0.004(3)	0.006(3)	0.007(3)	0.000	0.000	0.000

Table A20 Selected Bond Distances (Å) and Angles (°) of Crystal with $x = 0.7$

	298K	90K
Distances		
Sr1-O1	2.7542(2)	2.74994(14)
Sr1-O3 (×4)	2.742(4)	2.736(4)
Sr2-O2	2.7615(9)	2.7584(11)
Sr2-O3 (×4)	2.622(4)	2.620(4)
Ru1-O1	1.9527(18)	1.9472(19)
Ru1-O2	1.935(12)	1.948(13)
Ru1-O3 (×4)	1.94762(17)	1.964463(13)
Angles		
O1-Ru1-O3 (×4)	89.35(16)	89.33(19)
O2-Ru1-O3 (×4)	90.65(16)	90.67(19)
Rotation		
[a]RuO_6 octahedra	n/a	n/a

[a] This value represents the rotational angle (Φ) for the RuO_6 octahedra. For a view of the rotational angles along the *ab*-plane, please see Figure 4.2(b).

Appendix B: Letter of Permission

7/1/2011

To whom it may concern

I am preparing my dissertation entitled

"EVOLUTION OF STRUCTURAL AND PHYSICAL PROPERTIES OF TRANSITION METAL OXIDE $SR_3(RU_{1-x}MN_x)_2O_7$ ($0 \leq X \leq 0.7$) WITH MN CONCENTRATION"

to be submitted to the Graduate faculty of the Louisiana State University and Agricultural and Mechanical College in a partial fulfillment of the requirement for the degree of Doctor of Philosophy in the Department of Physics and Astronomy.

I would appreciate permission to reproduce the following item(s) in both print and electronic editions of the dissertation. Unless you indicate otherwise, I will use the complete reference given above as the credit line. In case you do not control these rights, I would appreciate it if you could let me know to whom I should apply for permissions.

Figures: Figure 4.2, 4.5, 4.6
Tables: Table 4.1, 4.2, 4.3, 4.4, 4.9

Title: Surface and bulk structural properties of single-crystalline Sr3Ru2O7

Authors: Biao Hu[1], Gregory T. McCandless[1], Melissa Menard[2], V. B. Nascimento[1], Julia Y. Chan[2], E. W. Plummer[1], and R. Jin[1,*]

Affiliations:
[1] Department of Physics and Astronomy, Louisiana State University, Baton Rouge, Louisiana, 70803, USA
[2] Department of Chemistry, Louisiana State University, Baton Rouge, Louisiana, 70803, USA

*Author to whom any correspondence should be addressed

Email: rjin@lsu.edu

Journal: Physical Review B
Issue: Volume 81, Issue 18
Year: 2010
Citation: Biao Hu, *et al*.
Phys. Rev. B 81, 184104 (2010) DOI:10.1103/PhysRevB.81.184104

For your convenience a copy of this letter may serve as a release form: the duplicate copy may be retained for your files.

Thank you for your prompt attention to this request. Permission is being requested of the authors and publisher separately.

Sincerely yours,

Biao Hu

Department of Physics and Astronomy
Louisiana State University
Baton Rouge, LA 70803, USA

I/We grant permission for the use of the work as set out above.
Signed:

Eileen LaManca
Publications Marketing Coordinator

Date: July 8, 2011

On behalf of Publisher: AMERICAN PHYSICAL SOCIETY

Statement of Copyright

Vita

Biao Hu was born on December 21, 1979, in Taojiang, Hunan Province, China. He graduated from Lanzhou University, Lanzhou, China, with a Bachelor of Science degree in physics in July, 2002. He received a Master of Science degree in physics from Fudan University, Shanghai, China, in July, 2005. He came to the U.S. and started his graduate study in The Department of Physics & Astronomy in The University of Tennessee, Knoxville, Tennessee, in August 2005. In September 2009, he transferred to The Department of Physics & Astronomy in Louisiana State University, Baton Rouge, Louisiana, to continue his doctoral program. He expects to receive his Doctor of Philosophy degree in physics in August, 2011.